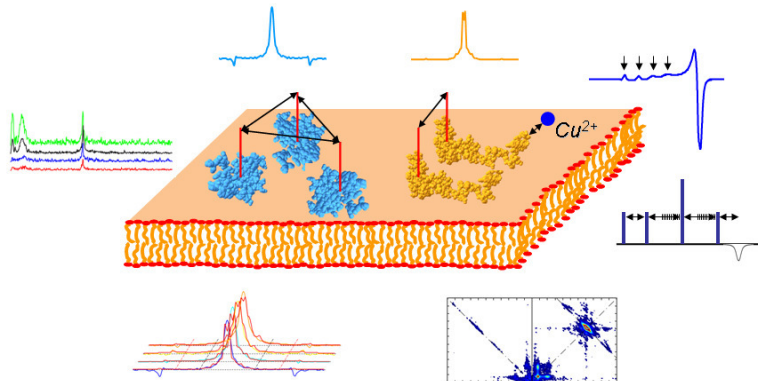




Studies of Myelin Basic Protein (MBP) Using Electron Paramagnetic Resonance (EPR) Spectroscopy



Timo Bund

Diplomarbeit
Johannes Gutenberg-Universität, Mainz

Studies of Myelin Basic Protein (MBP) Using Electron Paramagnetic Resonance (EPR) Spectroscopy

Fachbereich Biologie

Diplomarbeit

zur Erlangung des akademischen Grades „Diplom-Biologe“ am Fachbereich Biologie der
Johannes Gutenberg-Universität, Mainz

eingereicht von: Timo Bund
geb. am 19.10.1983
in Frankenthal (Pfalz).
Albert-Schweitzer-Strasse 17a
55128 Mainz

1. Gutachter: Prof. Dr. Harald Paulsen
2. Gutachter: Prof. Dr. Hans W. Spiess

Mainz, den 4.9.2009

Max-Planck-Institut für Polymerforschung
Ackermannweg 10
D-55128 Mainz



Die Natur ist so gemacht,
Dass sie verstanden werden kann.
Oder vielleicht sollte ich richtiger umgekehrt sagen,
Unser Denken ist so gemacht,
Dass es die Natur verstehen kann.

Werner Heisenberg

Contents

Introduction	1
1. Theory	5
1.1 Myelin basic protein (MBP) - structure and function	5
1.1.1 Spin-labeled MBP	11
1.1.2 The uptake of Cu ²⁺ by MBP	16
1.2 Introduction to EPR spectroscopy	17
1.2.1 CW EPR spectroscopy	21
1.2.2 Pulse EPR spectroscopy	27
1.2.2.1 The electron spin echo (ESE) experiment	31
1.2.2.2 The 2-pulse ESEEM experiment	33
1.2.2.3 The instantaneous diffusion experiment	33
1.2.2.4 The 3-pulse ESEEM experiment	34
1.2.2.5 The HYSCORE experiment	36
1.2.2.6 The DEER experiment	36
2. Materials and Methods	38
2.1 Technical equipment and chemicals	38
2.1.1 Technical equipment	38
2.1.2 Chemicals	38
2.2 Sample preparation	39
2.2.1 Non-spin-labeled MBP with Cu ²⁺ in solution	39
2.2.2 Spin-labeled MBP in solution	39
2.2.3 Spin-labeled MBP in artificial membrane vesicles	40
2.3 EPR Spectroscopy	41
2.3.1 Experimental procedure	41
2.3.1.1 CW EPR experiments	41
2.3.1.2 Pulse EPR experiments	41
2.3.2 Data analysis	45
2.3.2.1 CW EPR measurements	45
2.3.2.2 ESE measurements	45
2.3.2.3 2-pulse ESEEM measurements	45
2.3.2.4 Instantaneous Diffusion measurements	46
2.3.2.5 3-pulse ESEEM measurements	47
2.3.2.6 HYSCORE measurements	47
2.3.2.7 DEER measurements	47

Contents

3.	Results	49
3.1	The Uptake of Cu ²⁺ by non-spin-labeled MBP in solution	49
3.1.1	CW EPR measurements	49
3.1.2	ESE-detected EPR measurements	54
3.1.3	2-pulse ESEEM measurements	55
3.1.4	HYSORE measurements	56
3.1.5	DEER measurements	60
3.1.5.1	Orientation dependence of Cu ²⁺ DEER measurements	60
3.1.5.2	DEER measurements with different MBP/Cu ²⁺ ratios	62
3.2	EPR experiments based on spin-labeled MBP in solution	67
3.2.1	CW EPR measurements	67
3.2.2	ESE-detected EPR measurements	68
3.2.3	2-pulse ESEEM measurements	69
3.2.4	Instantaneous Diffusion measurements	69
3.2.5	DEER measurements	70
3.3	EPR experiments based on spin-labeled MBP in artificial membrane vesicles	71
3.3.1	CW EPR measurements	71
3.3.2	ESE-detected measurements	74
3.3.3	2-pulse ESEEM measurements	78
3.3.4	Instantaneous Diffusion measurements	79
3.3.5	3-pulse ESEEM measurements	81
3.3.6	HYSORE measurements	82
3.3.7	DEER measurements	83
4.	Discussion	89
4.1	MBP in solution: Evidence of aggregation of individual MBP molecules	89
4.1.1	The interaction of Cu ²⁺ and MBP	89
4.1.2	Spin-labeled MBP in solution: MBP aggregation even without Cu ²⁺	95
4.2	Structure determination of spin-labeled MBP in artificial membrane vesicles	95
4.3	Properties of the chemical vicinity of the spin labels within MBP	103
5.	Conclusions and Outlook	106
.	Appendix	111
.	List of Abbreviations and Symbols	112
.	References	113
.	Acknowledgements	119
.	Eidesstattliche Erklärung	121

Introduction

In the evolution of life, proteins perhaps represent both, one of the most remarkable but also mysterious class of substances at the same time. In the known ensemble of components, which are indispensable for the development of life, proteins rank at the lower nanometer scale and reflect only small dimensions when compared to, e.g., the macroscopic dimensions of higher organisms. Nevertheless, or rather due to their prominent position on the low nanometer range, proteins, functional proteins and enzymes are responsible for some of the most characteristic phenomena, which determine life of all organisms. These effects can be triggered by even slight modifications in protein structure or the interaction of proteins with other proteins, cofactors or other substances.

It is therefore not astonishing that in the history of biological research up to now great efforts have been made in order to further characterize this kind of biological molecules. With the advancement of physical characterization methods in recent decades, the intrinsically complex class of membrane proteins has moved into the focus of protein research. Several of the most famous experiments in biophysical and biochemical research of the last decades highlighted the importance of membrane proteins within basic molecular processes of all kind. Some prominent representatives are ATP synthase or complexes I-IV of the electron transport chain, which are essential for cellular production of energy.¹⁻² Membrane proteins are also engaged in signal transduction pathways or serve as channel proteins, and, in general, account for about 30% of the total cellular reading frames.³

The class of membrane proteins comprises molecules of most different properties. In the classic approach, they are classified by their specific structure. Therefore, structural proteins are well distinguishable from soluble proteins by just analyzing their structure. For most of the classical proteins the general structure is apparently also inseparably correlated to the protein function (structure-function paradigm).⁴ In the last few decades this view has changed dramatically with the knowledge that also a type of rather 'unstructured' proteins - the so-called *intrinsically unstructured proteins* or *IUPs* - exists, which nonetheless partially seem to have a *function*.⁴⁻¹¹ The importance of this new class of proteins became increasingly apparent and great efforts have been undertaken to further characterize their properties. One now generally acknowledged insight is that for a complete characterization of such a protein, its structure, function, and its molecular dynamics have to be known. The validity of the structure-function paradigm seems to be restricted significantly.⁴ Notably, the intrinsic lack of structure of IUPs makes this class of proteins also intrinsically hard to characterize.¹² Crystals are rarely available and X-ray crystallography, as one of the main tools of structural characterization in biophysics cannot be applied.¹³

Introduction

One of the most prominent representatives of intrinsically unstructured proteins is myelin basic protein (MBP), which represents the 2nd most abundant protein within the myelin sheath.¹⁴⁻¹⁶ The myelin sheath (~70% lipids by dry weight) represents a macroscopic insulation around axons of the central and peripheral nervous system with diameters up to 50 μm and lengths of up to 750 μm and accounts for the correct transmission of nervous signals. Obviously, any structural changes of this complex arrangement of lipids and proteins could lead to severe restrictions in the functionality of the nervous systems.¹⁵ Failure of “correct” insulation takes place in reality and manifests itself in a row of indications, which are characteristic for one of the most severe autoimmune diseases: multiple sclerosis (MS).¹⁷ Here, an immune response, which is based on the attraction of an immuno-dominant epitope of MBP, results in de-stabilization or degradation of the entire myelin sheath.¹⁸ This phenomenon seems to be correlated to the typical charge level of MBP.¹⁹ In healthy people a characteristic MBP charge isoform C1 with a net positive charge of +19 dominates the lipid fraction of MBP, while in MS patients the lipid fraction is dominated by charge isomer C8 with a net positive charge of +13.

MBP most obviously acts like a “molecular glue” and contributes significantly to the overall stability of the microscopic structure of the myelin sheath.¹⁹ The molecular basis of the interactions between MBP and the lipid bilayers on the one hand and potentially between MBP molecules on the other hand is only partially known. In this context, aggregation of MBP and specific, additional interactions with divalent metal ions like Zn^{2+} (and Cu^{2+}) are discussed (Fig. I).²⁰⁻²³

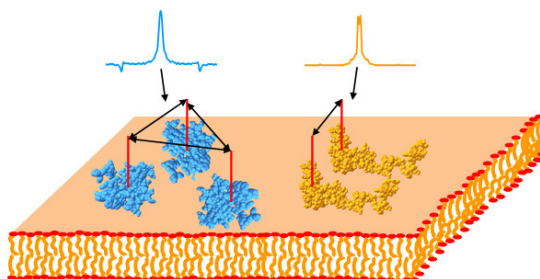


Fig. I. Schematic picture of interacting MBP molecules within the peripheral part of the myelin membrane and distances, which can be measured between selected positions within the MBP monomers by simulation of dipolar spectra obtained by double electron electron resonance (DEER) EPR measurements.

There clearly is a lack of robust information on MBP structure in solution as well as in the myelin sheath and so far all attempts to obtain X-ray diffraction data from 3D crystals which would give atomic resolution have failed.²⁴ Important information was obtained by cryo-electron microscopy (transmission electron microscopy, TEM).²⁵ The artificial 2D crystals used in this study allowed for the discovery of lamellae-like structures and additionally enabled to perform single particle reconstruction based on TEM, but it was not clear whether these studies observe isolated MBP or MBP aggregates.²⁶ Also optical waveguide light mode spectroscopy was performed indicating

Introduction

MBP clustering on artificial myelin membranes.²⁷ Additional information was gained by NMR experiments, which first underlined the 'unstructured' property of MBP (> 1/3 of the protein remains unordered), but, second, was also able to allocate regions of high mobility or possible α -helicity to the protein sequence.²⁸⁻³¹ Further crucial information was obtained by standard continuous wave (CW) electron paramagnetic resonance (EPR) measurements based on site-directed spin labeling (SDSL) of MBP in artificial membrane vesicles. With power saturation measurements, the immunodominant epitope was found to be positioned within a central α -helical region.¹⁹ The orientation and penetration depth of the helix into the membrane depend on the charge of the protein. The helical region of MBP C1 (healthy) stays within a more buried position compared to the one of MBP C8 (decreased charge, MS), which can be correlated to the auto-immuno response.

Thus EPR spectroscopy already revealed its potential to elucidate MBP structure and to selectively characterize different protein regions of MBP.¹⁹ Methods of EPR spectroscopy do not need long- or intermediate-ranged order and can characterize molecular structures up to a range of 8 nanometers and in the pico- to microsecond time scale of rotational reorientation. With sophisticated methods of pulse EPR an even more detailed study of MBP may thus be possible.

In this thesis, pulse EPR methods like electron spin echo (ESE) experiments, 2- and 3-pulse electron spin echo envelope modulation (ESEEM) experiments, and hyperfine sublevel correlation (HYSCORE) experiments were performed on MBP C1 in artificial membrane vesicles. Selective nanometer distance measurements using double electron electron resonance (DEER) were performed. This broad arsenal of pulse EPR methods should allow even deeper insights into the interaction of MBP and interaction of MBP with the membrane component. Distance information obtained from DEER data could enable determination of the interaction model and even deliver information about the overall dimensions in case of possible MBP aggregation.

This thesis is divided into five chapters. The first two chapters provide the basic knowledge to understand the scientific approach used in this thesis. In Chapter 1, the reader is introduced into the biological system under investigation and the basic EPR theory, as far as it is necessary to understand the performed EPR measurements. In Chapter 2, the reader is provided with additional, detailed information about the sample preparation, the individual measurements procedures, and data analysis. Chapter 3 presents experimental results obtained by the different CW and pulse EPR measurements. Here, first results from the experiments concerned with the uptake and interaction of MBP and Cu^{2+} ions are presented, followed by the results obtained for nitroxide spin-labeled MBP in solution and, finally, in artificial membrane vesicles. Chapter 4 delivers a discussion of the results based on the theoretical background, which is formulated in Chapter 1, highlighting correlations between results obtained from the different experiments. In

Introduction

Chapter 5, a short summary is given, which represents the synthesis of *ab initio* ideas, results, experiences, and the detailed discussion of Chapter 4. The drawn conclusions serve as a basis for a short outlook on the potential study of the charge-reduced MBP isomers found in MS patients and the impact that the knowledge of MBP structure and aggregation in the myelin sheath may have on the understanding of the progression and/or the origins of this neurodegenerative disease.

1. Theory

1.1 Myelin basic protein (MBP) - structure and function

Myelin basic protein (MBP) is a prominent member of a protein family known as intrinsically unstructured proteins (IUPs). Such proteins represent a significant fraction of the cellular proteome and share a high level of structural flexibility dependent on their environment or the association with specific ligands. In some special molecular interactions, parts of such proteins possess a characteristic structure and are therefore also known as pliable or conformationally adaptive.^{4, 6-10} The general protein seems to be designed in order to allow highest levels of interaction, enabling a fast response to changes in the environmental conditions.^{4, 32} For this reason and also because of the rather specific ligand interactions, IUP often serve as important elements within signal transduction pathways.^{4, 7} The stretched disordered segments, which are characteristic for IUPs, most often occur in eukaryotic proteins.³³ With respect to the central paradigm of molecular biology which closely correlates protein structure with protein function, the relation between the apparent lack of structure for IUPs and the coexisting high level of rather specific ligand interaction challenges the conventional way of scientific interpretation.

One of the most interesting IUPs is represented by MBP, which is predominantly found in membranes of the myelin sheath of the central nervous system (CNS, Fig. 1.1).^{14-15, 34}

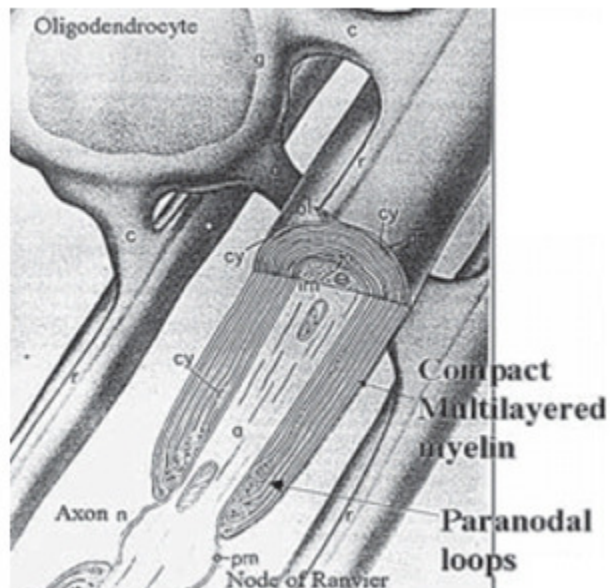


Fig. 1.1. Myelin membranes originating from an oligodendrocyte, which wrap around nervous axons (up to a hundred times) thereby establishing the characteristic structure of the myelin sheath. MBP represents up to about 70% of this characteristic structure by dry weight. Figure adapted from Boggs (2006)³⁴

Theory

In the myelin sheath specific membranes extend from oligodendrocytes and concentrically wrap around the nerve fibers (up to a hundred times) resulting in the myelin sheath. The resulting structure resembles an electrical insulation and finally grants for the characteristic and rapid transmission of nerve impulses within the CNS (Fig. 1.2).²⁴

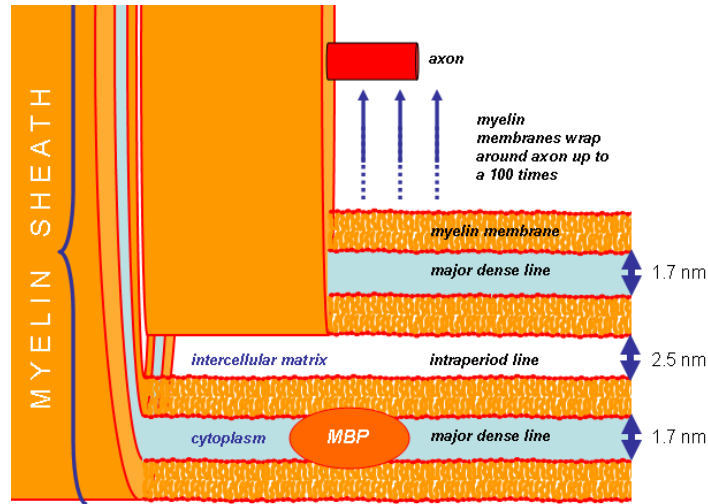


Fig. 1.2. Structural components of the myelin sheath and tentative picture of membrane-bound MBP.

In the peripheral nervous system the general structures are similar to those of the CNS, and mainly differ in the molecular composition of the membranes.³⁵ Most of the myelin is represented by lipids (up to 70% by dry weight), which is very remarkable with respect to other cellular membranes, which feature a significantly lower lipid content. The two major components are thereby represented by MBP and proteolipid protein (PLP) which feature approximately equimolar proportions.¹⁵

It is easy to appreciate that defective assembly of the myelin sheath can result in severe neurological disorders.¹⁵⁻¹⁷ In this context, multiple sclerosis (MS) represents a well-known human disease of multifactorial origin that is closely correlated to active degradation of the myelin sheath by autoimmune attack.¹⁷ MS was described in the late 19th and in the 20th century, when results revealed that injection of specific brain material, also MBP, finally leads to a demyelination process like it was observed for MS.³⁶ This condition was termed experimental autoimmune encephalomyelitis (EAE). Further studies on MBP (which usually refers to the most abundant 18.5 kDa isoform of MBP) revealed the importance of MBP as a candidate autoantigen in MS as well as its stabilizing effects within the myelin sheath.¹⁸ More recently results also established an 'executive' character of MBP, like e.g. in signal transduction pathways during development or remyelination attempts during MS.¹⁸

Theory

In closer examination, the standard MBP (18.5 kDa isoform) represents a gene product based on differential splicing of one single mRNA transcript (Fig. 1.3).³⁷⁻³⁹

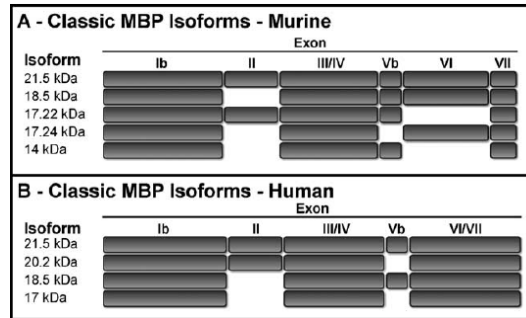


Fig. 1.3. Gene structure of the murine and human Golli-MBP-gene. Alternative splicing of the exons thereby gives rise to the characteristic isoforms of MBP (adapted from G. Harauz *et al.*, 2004).³⁸⁻³⁹

The correlated classic MBP gene consists of seven exons giving rise to five isoforms by differential splicing (21.5, 18.5, 17.24, 17.22, and 14.0 kDa) in mice. The human gene structure only reveals slight differences, with four isoforms in total: 21.5, 20.2, 18.5, and 17.2 kDa. The most abundant isoform is represented by 18.5 kDa in human and bovine mammalian CNS. The classic MBP gene is part of a larger gene complex called Golli (Genes of OLigodendrocyte Lineage) which features 11 exons in mice including the seven classic ones. Various gene products of the Golli family are produced during myelin formation or in remyelination attempts. By existing criteria each of the different isoforms is considered an IUP.⁴⁰⁻⁴² Like other IUPs, MBP also features a high net charge together with a low mean hydrophobicity, which maximizes the effect of intramolecular static repulsion and minimizes the contribution of a hydrophobic collapse. Within a charge-hydrophobicity plot the affiliation of proteins to the class of IUPs or classically folded proteins can be determined empirically. All MBP isoforms fall within the unstructured region in this plot (Fig. 1.4).

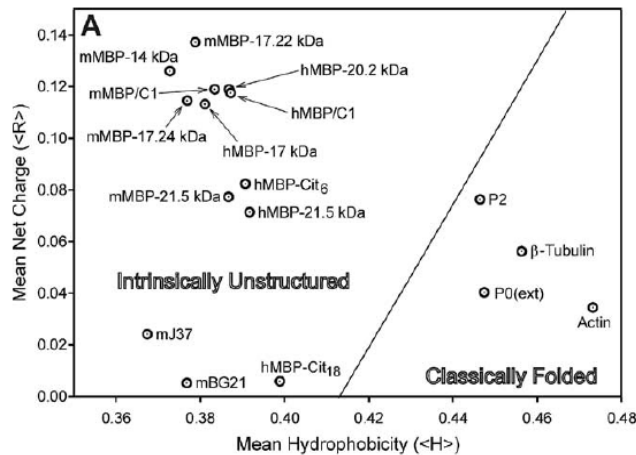


Fig. 1.4. Charge-hydrophobicity plot of MBP isoforms (adopted from Harauz *et al.*, 2004).⁴⁰⁻⁴¹ The dividing line represents an empirically determined division between the classes of intrinsically unstructured and classically folded proteins (determined by X-ray crystallography, adapted from G. Harauz *et al.*, 2004).^{9, 11, 42}

IUPs are also characterized by the characteristic amino acid composition with an increased proportion of P, E, K, S, and Q and reduction of W, Y, F, C, I, L, and N. MBP shares many characteristics of IUPs (Fig. 1.5), like proline enrichment or the absence of hydrophobic amino acids, but there are also characteristic discrepancies between IUP and MBP-features are observed, e.g. the increased level of arginin for interaction with the negatively charged phospholipids of the membrane and decreased levels of glutamic acid.⁴³

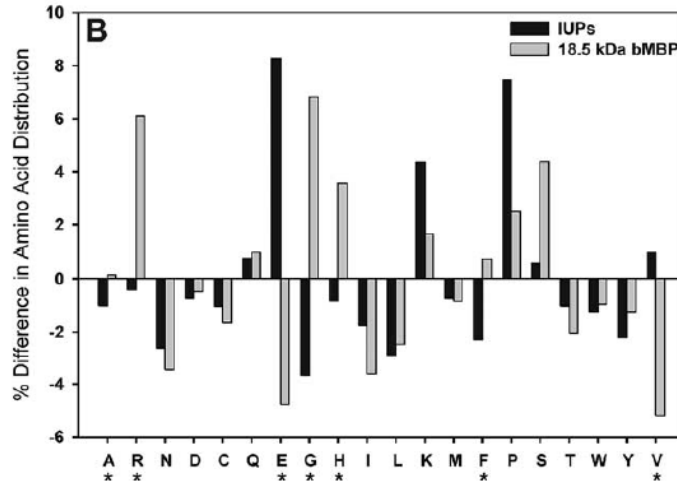


Fig. 1.5. Amino acid content of typical IUPs and the 18.5 kDa isoform of MBP based on sequence accessible on the protein data bank (see text for details, adapted from G. Harauz *et al.*, 2004).⁴²

The high number of histidines accounts for the potential coordination of divalent cations *in vitro* and *in vivo*, as suggested by many results.²¹⁻²³ Decreases numbers of the more hydrophobic amino acids are probably related to the lack of a hydrophobic core, although the phenylalanyl residues interact hydrophobically with the membrane.⁴³

With reference to the well studied stabilization effects of MBP on the myelin sheath with the 18.5 kDa isoform, further results highlighted the extremely basic properties of this isoform. A number of additional charge isomers were discovered, which result from an almost infinite number of possible post transcriptional modifications (PTMs) like N-terminal acylation, ADP-ribosylation, deiminations, phosphorylation, deamidation, methylation, and oxidation of specific amino acids.⁴⁴ The charge isomers are named C1-C8. The most cationic and original isoform features a net positive charge of +21. Analysis of MBP purified from healthy human myelin tissue resulted in a net positive charge of about +19 (MBP C1), while proteins prepared from myelin tissue of MS patients revealed a net positive charge of about +13 or even almost zero, for a patient, who suffered from the most acute and fulminating form of MS known as Marburg's syndrome. Here, 18 of 19 arginines were deiminated (citrullinated) on average.⁴⁵ This results in a perturbation of the protein structure and limits interaction of the protein with itself and with the membrane lipids, which finally results in significant limitations of the ability of MBP to maintain a compact myelin sheath.

A classical structure-function analysis of MBP has been pursued with great efforts. In general, one of the most important approaches is represented by structure determination based on X-ray diffraction from 3D crystals. With reference to MBP, until now, it was not possible to identify MBP structure with this method, since no adequate 3D-protein crystals could be achieved - a situation which is observed for a large number of ('uncrystallizable') membrane proteins.¹³

Alternatively, experiments based on transmission electron microscopy were performed. Here, soluble or membrane-associated proteins were induced to form 2D crystals by interaction with a mixed lipid monolayer formed on an air water interface. Several approaches identified multilamellar arrangements with a distance of about 4.8 nm between repeated, lamellar structures and particles of about 3 - 4 nm diameter (Fig. 1.6).²⁵⁻²⁶

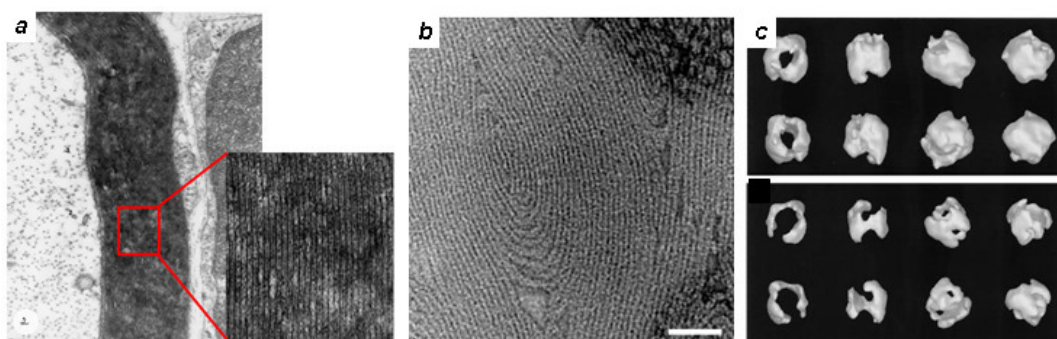


Fig. 1.6. MBP structures observed with transmission electron microscopy (TEM). **a:** TEM picture of myelin membranes. The detailed view reveals the characteristic assembly of the myelin membranes within the myelin sheath (source: Biology Image Library). **b:** Hexahistidine-tagged MBP on an artificial model membrane forming 2D crystals with characteristic lamellae-like structures and isolated particles in the periphery (Bates, 2000).²⁵ **c:** Computational 3D reconstruction of MBP molecules absorbed to an artificial lipid monolayer indicating an overall "C" shape of outer radius 5.5 nm, inner radius 3 nm, overall circumference 15 nm, and height 4.7 nm (Beniac *et al.*, 1996).²⁶

In this context, also computational 3D particle reconstruction was performed based on TEM. Experiments with MBP as negatively stained single particles absorbed to a lipid monolayer delivered results indicating an overall "C" shape with an outer radius of 5.5 nm, an inner radius of 3 nm, an overall circumference of 15 nm, and a height of 4.7 nm for MBP molecules, but it is not exactly clear whether the observed particles resemble single MBP molecules or MBP aggregates.²⁶

Another approach for structure determination of proteins is represented by methods based on magnetic resonance spectroscopy like NMR or EPR. Solid state NMR studies of MBP and bound actin filaments strongly indicated that at least one third of the protein remained exposed to the solvent and mainly disordered. Solution NMR experiments based on backbone dynamics implicated that different regions exist within the MBP molecules with a propensity towards α -

Theory

helicity, which is stabilized by membrane-mimetic condition, for residues 33 - 46, 83 - 92, and 142 - 154²⁹⁻³¹. An increased level of mobility was found for residues 15 - 23, 46 - 67, 120 - 148, and 154 - 163. Additionally, the region of 142 - 154 was reported as the primary calmodulin-binding site.

The amino acid sequence of human MBPC1, as well as suggestions for secondary structure elements are summarized in Fig. 1.7.

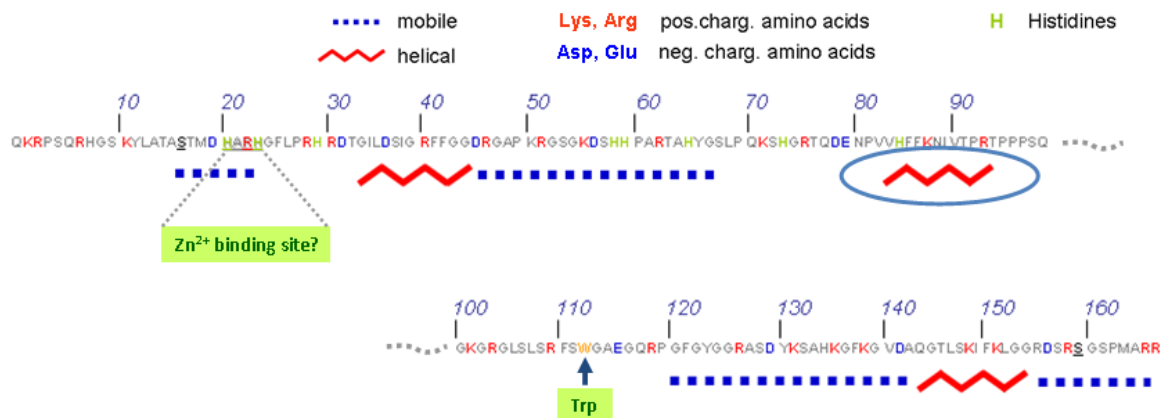


Fig. 1.7. Amino acid sequence of human MBP C1 with a potential Zn^{2+} binding site, and suggestions for secondary structure elements by NMR and CD studies.²⁹⁻³¹ The helical region at residues 82 - 93 (indicated by the blue circle) was observed by CW EPR experiments.¹⁹

1.1.1 Spin-labeled MBP and EPR

The CW EPR measurements, which were performed so far on this biological model system, were based on site-directed spin labeling (SDSL) of MBP in a myelin-like membrane environment. Since the samples, which were used for the EPR measurements presented in this work, were also prepared by SDSL, a short introduction to this basic technique is given at this point.

The reason, why a procedure like SDSL has to be performed at all in order to enable EPR measurement for this protein, is given by the fact that MBP itself represents a molecule with no intrinsic unpaired (or free) electron. Only very few biological molecules possess free electrons in their physiological structure and are therefore EPR-active *in vivo* (examples are complexes of proteins with paramagnetic transition metals like e.g. Cu, Ni, Mn, Fe, Rh, or Ir, Fig. 1.8, a). For molecules like MBP, this means that a free electron has to be introduced artificially into the protein. A standard approach for doing so is represented by SDSL. Here, a small molecule, the spin label, is chemically attached to the protein of interest. The methanethiosulfonate spin label (MTSSL, Fig. 1.8, b), representing one of the most common spin-labels, contains a free electron within a nitroxide group (indicated by the red circle), which is sterically stabilized by surrounding methyl groups.

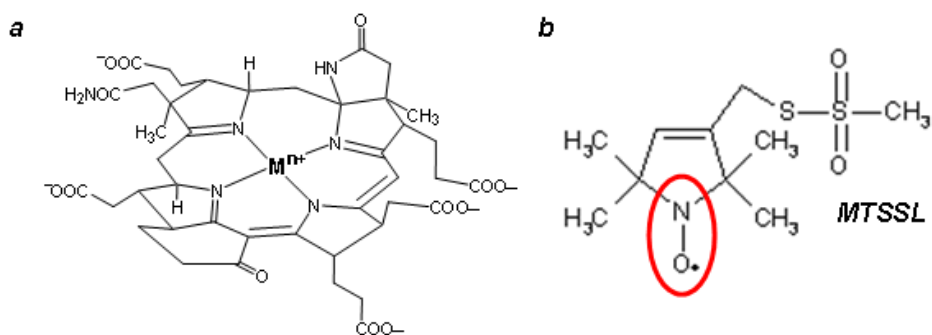


Fig. 1.8. **a:** Characteristic complex for coordination of metal ions within biological molecules. For coordination of EPR-active metal ions the protein becomes accessible for EPR measurements without additional chemical modifications (here, the metal ion is coordinated to a tetrapyrrole-ring). **b:** Chemical structure of MTSSL ((1-Oxyl-2,2,5,5-tetramethylpyrroline-3-methyl) methanethiosulfonate spin label) representing one of the most common spin-labels.

Spin label molecules like MTSSL feature a small overall size, which limits sterical effects on the protein structure and results in a minimum of structural perturbation. This feature represents one of the most important advantages of EPR when compared to the more common methods like e.g. fluorescence microscopy. Most often, the spin labels are attached to the protein of interest via interaction of the sulfhydryl group of the spin label molecule and one or more sulfhydryl groups within the protein. For specific labeling (as it is the case for the majority of EPR measurements) selected amino acids are mutated to cysteines (one or more mutations per molecule; e.g. the

mutation of serin to cysteine at position 17 of the protein sequence, which can be shortly written as S17C) in order to artificially introduce sulfhydryl groups within the protein of interest. Then sulfhydryl groups of the spin label and of the recombinant protein interact forming stable disulfide bridges and a secure attachment of the spin label at well defined (*i.e.* site-directed) positions within the protein (Fig. 1.9).

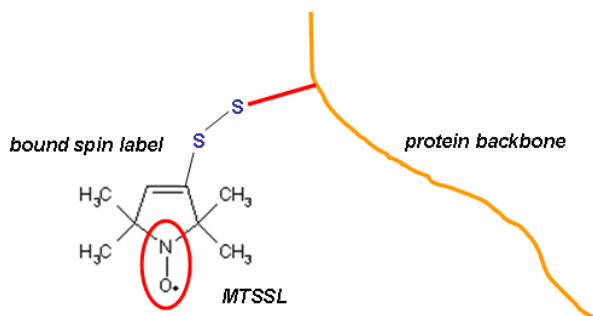


Fig. 1.9. Structure of MTSSL selectively bound to a protein. The artificially introduced cysteinyl group within the protein interacts with the cysteinyl group of the spin label forming a stable disulfide bridge.

For proteins containing cysteines in their native protein sequence, these cysteines have to be removed prior to the SDSL. This is not the case for MBP, which lacks any cysteines in its native structure. MTSSL, which was used as spin-label, can be attached to the protein of interest in hydrophobic as well as hydrophilic environments. The putative disadvantage of the additional, time-consuming step of artificially introducing the spin label can finally be regarded as a great advantage, since protein structure and dynamics can thereby be studied with very high selectivity. In this context, for more recent EPR measurements, a set of MBP samples including MBP in artificial model membranes was prepared using SDSL at defined labeling positions (which were selected in order to cover a large scope of the MBP sequence). Final CW EPR results indicated only very little overall immobilization in solution, as indicated by sharp hyperfine lines in the spectra. Together with the artificial membrane vesicle a clear tendency towards broader spectral features was observed indicating MBP interaction with the membranes. Power saturation measurements revealed values for the penetration depth of each spin label into the lipid membrane (Fig. 1.10).

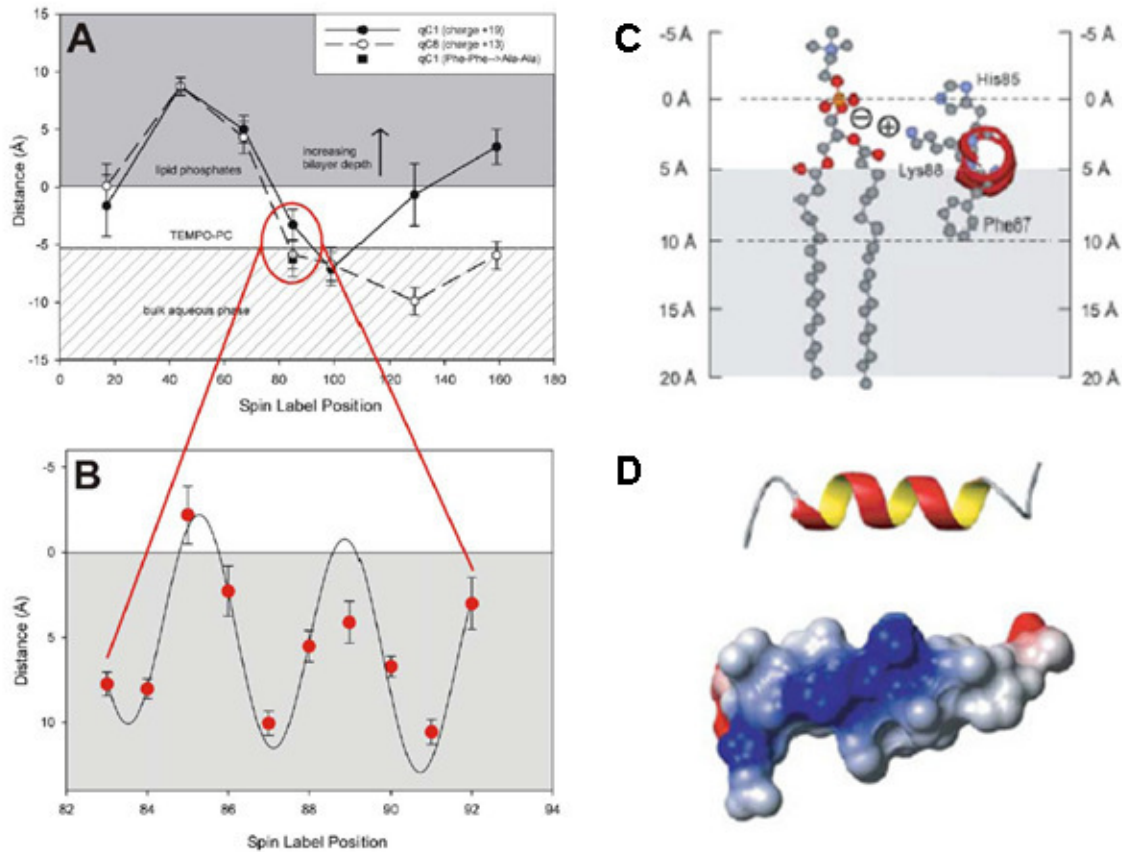


Fig. 1.10. A: Penetration depth of the different spin labeling positions within MBP C1 and C8 as detected by EPR power saturation measurements. **B:** The proteins Val83 to Thr92 feature a characteristic oscillation within the penetration depth which could be assigned to a helical structure. **C:** Scheme of the penetration of the helical region within the lipid layer depicting the most exposed amino acid residues within the tilted (9° with respect to the plane of the bilayer) α -helical immunodominant epitope. **D:** Ribbon and space-filled model for the region of proteins Pro82 to Pro93 (partial charge distribution indicated by: red = negative, white = neutral, blue = positive). Figure adapted from Harauz and Libich (2009).

A detailed analysis allowed for the remarkable identification of a helical structure for the region of residues 83 - 92. Experiments with MBP charge isomers C1 and C8 indicated that the characteristic helical region, which also represents the autoimmune epitope, changes its overall position and orientation with respect to the lipid surface. A clear tendency of decreased penetration depth and higher solvent accessibility was reported for the helical region of the less charged MBP isomer C8, which also implicates higher solvent accessibility for the autoimmune epitope and increased levels of biological interaction (Fig. 1.11).

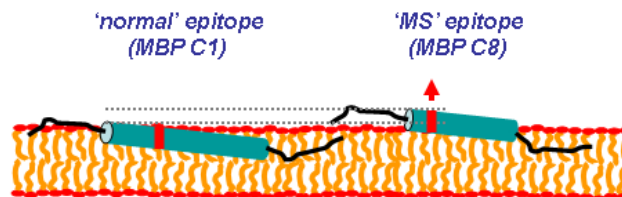


Fig. 1.11. Schematic presentation of the orientation of the α -helical part of MBP charge isomers C1 and C8, representing the 'normal' epitope (red bars) and the 'MS' epitope, respectively. The immunodominant epitope features a higher solvent accessibility for charge isomers C8. The resulting penetration depths thus indicate a more surface exposed orientation of the shortened α -helical region for MBP C8.

In this work all, sample preparations were based on the 18.5 kDa isoform and charge isomer C1 (the least modified MBP, from now on referred to as 'MBP'). Molecules were purified and spin labeled at well-selected positions. For measurements focusing on structure determination of MBP molecules in the presence of myelin-like membranes, additional artificial membrane vesicles were added with a characteristic lipid composition, which is similar to the one of myelin membranes *in vivo*. The characteristic selection of the spin labeling positions allows for a high selectivity in measurements probing structure and dynamics of the protein (CW, ESE, DEER measurements, Fig. 1.12).

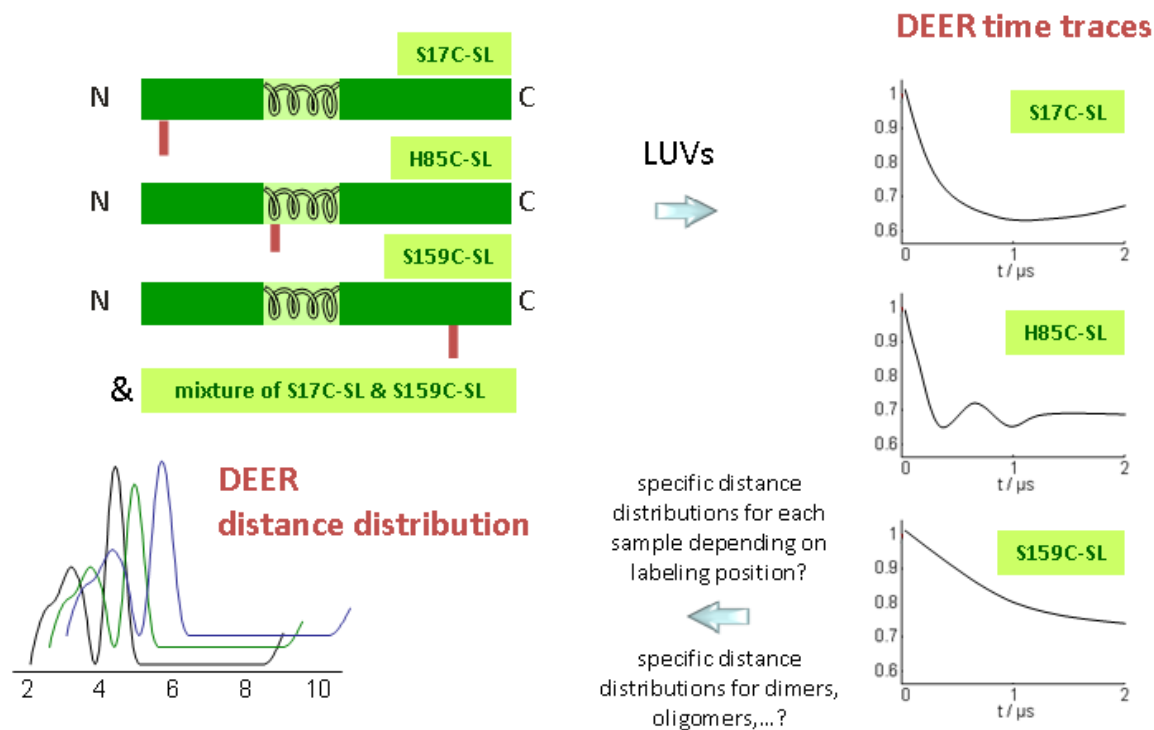


Fig. 1.12. EPR approach for structure determination of MBP in the presence of artificial membrane vesicles. Different labeling positions within the protein allow for detection of distance distributions, which are characteristic for each labeling position (and the mixture of S17C and S159C). After the original time traces are Fourier-transformed to dipolar spectra the specific distance distribution becomes accessible and enables to specify different types of MBP interaction. Note that the time-domain data on the right and the distance distributions on the left are not measured but simply chosen to highlight possible differences expected for different labeling positions.

Distance information revealed by DEER measurements would lead to characteristic distance distributions for several of the MBP interactions proposed so far and should allow for the identification of the MBP interaction type (Fig. 1.13).

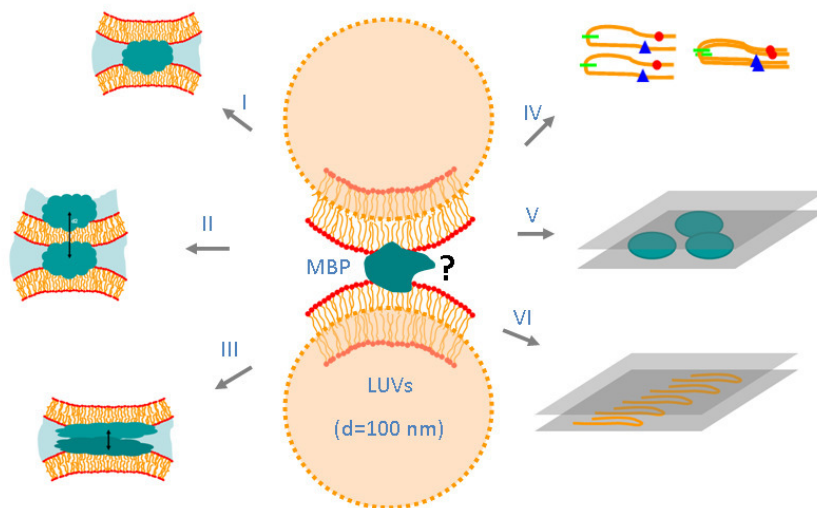


Fig. 1.13. Possible interaction of MBP molecules in the presence of artificial membrane vesicles. The different scenarios I-VI will be discussed in Chapter 5 (Discussion) in detail.

Further simplifications for the interpretation of obtained EPR results were correlated with several additional and characteristic modifications of the sample conditions. In this context, the modification of the membrane diameter by different lipid compositions should be mentioned. Also the effect of different lipid-to-protein ratios was tested. Additional measurements were based on MBP in solution without artificial membranes. This set of basic measurement conditions allows for a variety of new information about the local environment of the spin labels, the characteristic MBP conformation in membranes and in solution, and possible structural changes for the comparison of different MBP charge isomers.

1.1.2 The uptake of Cu^{2+} by MBP

An additional, very characteristic feature of MBP is its ability to bind divalent cations (MBP 18.5 kDa) in the order $\text{Hg}^{2+} > \text{Cu}^{2+} > \text{Zn}^{2+} > \text{Mg}^{2+} > \text{Cd}^{2+} > \text{Co}^{2+}$, which leads to a number of biologically relevant effects. The most important effects were observed for the interaction of MBP with Zn^{2+} or Cu^{2+} ions. The interaction of MBP with Zn^{2+} leads to a stabilization of the myelin membrane. Cu^{2+} also seems to play a very important role within the interplay of MBP and divalent metal ions. In this regard, it is known from calorimetric measurements that the uptake of Cu^{2+} by MBP takes place on an even higher level than the uptake of Zn^{2+} . Additionally, several other effects based on MBP and Zn^{2+} together with phosphate were documented. Here, e.g. the formation of cryptic aggregates as studied by light scattering was reported. Fluorescence studies indicated a significant quenching of the fluorescence intensity of the single tryptophan residue within the MBP sequence by the interaction with Cu^{2+} and a blue shift for interaction with Zn^{2+} . Furthermore, there are direct hints for a zinc binding site (residues 23 - 26: His-Ala-Arg-His) within the MBP sequence. As for the uptake of Cu^{2+} ions two binding sites with positive cooperativity ($K = 0.083 \mu\text{M}^{-1}$ and $n = 1.74$) were proposed, which allow an uptake of statistically 2.18 Cu^{2+} ions per MBP molecules.

Since Cu^{2+} represents an EPR-active ion with ($S = 1/2$, $^{63/65}\text{Cu}: I = 3/2$), direct investigations of the interaction between MBP and Cu^{2+} are possible. In this context valuable information about the number of binding sites, properties of the coordinated Cu^{2+} species, overall MBP structure in solution (studied by DEER distance measurements) and structural changes of MBP upon Cu^{2+} -uptake can be obtained. In this work, these were the corner stones for the performed experiments based on native MBP (charge isoform C1) and Cu^{2+} for different buffer conditions (*vide infra*).

1.2 Introduction to EPR theory

Electron paramagnetic resonance (EPR) spectroscopy represents a powerful tool for investigation of molecular structure and dynamics as well as of the local distribution of paramagnetic centers.⁴⁶ At the same time, EPR is a energy-saving alternative compared with neutron scattering or Mößbauer spectroscopy which allow comparable investigations. This spectroscopic method is based on the interaction of an electron spin of a paramagnetic center and an external magnetic field B_0 . Transitions between the different spin states are induced by resonant, electromagnetic radiation with frequencies in the nano/micro-second scale. The frequency is dependent on the electronic structure of the surrounding of the paramagnetic center, the dynamics of the sample molecule in the external magnetic field and the position of neighboring nuclei/electrons. Determination of the parameters describing these effects leads to the typical characterization of EPR samples.

The paramagnetic centers themselves can be introduced into the EPR sample as spin labels, which, in most cases, are molecules of only a small molecular weight including one or more paramagnetic centers that are chemically stable due to sterical hindrance. The paramagnetic centers most often used are nitroxides. Most common spin labels belong to the chemical groups of piperidines, which are based on a six membered heterocycle, and the pyrrolidines including a five membered heterocycle. Additionally, spin labels can also include double bonds in the heterocycle or specific side groups, like e.g. iodoacetamido-groups, which allow direct and specific chemical bonding to proteins by formation of disulfide bridges.

Unpaired electrons, like they exist in EPR spin labels, possess an intrinsic spin and therefore also a magnetic momentum, which interacts with an external magnetic field. The electron spin resembles an eigen angular momentum of the electron, its operator is called \mathbf{S} , with the eigen values $m_S = \pm 1/2$ and is quantized along the magnetic field direction, usually defined as the z-axis. The spin angular momentum \mathbf{S} and its magnetic momentum μ_e are linked by the following equation:

$$\mu_e = -g_e \mu_B \mathbf{S} = \gamma_e \mathbf{S}.$$

μ_B represents the Bohr magneton, g_e is the g-factor for the free electron ($g_e = 2.00232$), and γ_e is called the magnetogyric ratio of the electron. For an electron within an external magnetic field B the z-axis of the system can be defined as the direction of vector B and the strength of the magnetic field as B_0 . Due to non-degenerate magnetic spin states, the energy of the electron within the magnetic field becomes sensitive to the magnetic quantum number m_S which can be $\pm 1/2$ depending on the orientation of the spin with respect to B :

$$E = g\beta_e B_0 m_S.$$

In the resonance condition the two spin states differ by an energy matched by electromagnetic radiation at the Larmor-frequency ω_s :

$$\Delta E = \hbar \omega_s = g \beta_e B_0.$$

In EPR spectroscopy, an ensemble of magnetic moments of electron spins is detected, which is represented by the macroscopic magnetization, the net magnetic moment per volume:

$$M_o = \frac{1}{V} \sum_{i=1}^N \mu_i.$$

The resonance position is altered with reference to the interaction of the electron spin with magnetic nuclei in its vicinity. Different energetic contributions are best described by the spin Hamiltonian. The static, time-independent spin Hamiltonian of an effective electron spin S coupled to m nuclei with a spin I is given by

$$H_o = H_{EZ} + H_{ZFS} + H_{HF} + H_{NZ} + H_{NQ} + H_{e-e}.^{46}$$

In terms of energy, here only contributions involving the spin are included, since other energetical contributions can well be separated from the magnetic interactions. The Hamilton operator presented here consists of the electron Zeeman interaction (H_{EZ}), the zero-field splitting (H_{ZFS}), the hyperfine interaction (H_{HF}), the nuclear quadrupole interaction (H_{NQ}) and weak electron-electron interaction (H_{e-e}), which will be explained in the following.

Electron Zeeman interaction

This interaction represents the dominating term in the Hamiltonian for common magnetic fields. It describes the splitting of the two degenerate spin states of the electron ($\pm 1/2$) based on interaction with the external magnetic field:

$$H_{EZ} = \beta_e B^T g S.$$

S represents the spin vector operator, the g -factor now has the form of a 3 x 3 matrix, which can be formulated as a symmetric tensor of three principal values (g_{xx} , g_{yy} , g_{zz}) and three Euler angles describing their orientation in the molecular coordinate system. In solution, the g tensor is averaged and can be characterized by the isotropic g -factor, determining the center of the CW EPR spectrum

$$g_{iso} = \frac{1}{3} (g_{xx} + g_{yy} + g_{zz}).$$

Zero field splitting

The zero field splitting describes dipole-dipole interactions between individual spins that form a group-spin of $>1/2$ and adds the fine structure term to the Hamiltonian

$$H_{ZFS} = S^T D S .$$

For spin systems with cubic symmetry and $S \leq 2$ the fine structure term vanishes completely.

Hyperfine interaction

This term specifies the interaction of the electron spin with surrounding nuclear spins and is one of the most important sources of information in EPR spectroscopy. The contribution of hyperfine interaction is given by

$$H_{HF} = \sum_{i=1}^N S^T A_i I_i = H_F + H_{DD} .$$

I represents the nuclear spin operator and \mathbf{A} the hyperfine interaction tensor. The hyperfine interaction Hamiltonian comprises two parts: the isotropic Fermi contact and the electron-nuclear dipole-dipole coupling (H_F and H_{DD}). In solution and fast tumbling of the electron spin, H_{HF} is entirely represented by the Fermi contact contribution

$$H_F = \sum_{i=1}^N a_{iso,i} S_i^T I_i$$

and the isotropic hyperfine coupling constant $a_{iso,i}$ is given for the respective nucleus i :

$$a_{iso} = \frac{2\mu_0}{3\hbar} g_e \beta_e g_N \beta_N |\psi(0)|^2 ,$$

with the vacuum permeability μ_0 , the nuclear g-factor g_N and the nuclear magneton β_N , and the electron spin density at the nucleus $|\psi(0)|^2$. In general, the isotropic hyperfine coupling is based on direct contact between the unpaired electron and the nucleus mostly by the non-vanishing electron spin density at the s-orbitals of the atom.

The dipole-dipole interaction with the characteristic dipolar coupling tensor \mathbf{T} acts through space and averages to zero for isotropic rotation in solution:

$$H_{DD} = \sum_{i=1}^N S_i^T T_i I_i .$$

Nuclear Zeeman interaction

Also the nuclear spins interact with the external magnetic field based on nuclear Zeeman interaction

$$H_{NZ} = -g_N \beta_N \mathbf{B}^T \mathbf{I} ,$$

with I representing the nuclear spin quantum number and isotropic g_N , which is a good approximation for common EPR experiments (and also in this work).

Nuclear quadrupole interaction

For nuclei with $I \geq 1$ the charge distribution is non-spherical and features a quadrupole moment. The resulting contribution can be written as

$$H_{NQ} = \mathbf{I}^T \mathbf{P} \mathbf{I} ,$$

with the quadrupole tensor \mathbf{D} . A measure of the magnitude of the quadrupolar coupling is usually given by the asymmetry parameter of the \mathbf{P} -tensor elements $\eta = (P_{xx} - P_{yy}) / P_{zz}$ and the quantity $e^2 qQ / \hbar$ with the product of the electric field gradient eq and the quadrupole moment Q . In cubic symmetry the quadrupole moment becomes zero and thus also the quadrupole interaction vanishes.

Electron-electron interaction

For strongly interacting between electron spins, interaction is best described as a zero field interaction of a group spin. If the interaction between two unpaired electrons is weak (common case), they are better described by their individual spins \mathbf{S}_1 and \mathbf{S}_2 , an exchange coupling tensor \mathbf{J} , and a dipole-dipole coupling tensor \mathbf{D} . The corresponding Hamiltonian for a two spin system is described as

$$\begin{aligned} H(\mathbf{S}_1, \mathbf{S}_2) &= H(\mathbf{S}_1) + H(\mathbf{S}_2) + H_{e-e} \\ &= H(\mathbf{S}_1) + H(\mathbf{S}_2) + H_{exch} + H_{DD,e} . \end{aligned}$$

$H(\mathbf{S}_1)$ and $H(\mathbf{S}_2)$ are the Hamiltonians for each individual spin, H_{EXCH} represents the exchange coupling Hamiltonian and H_{DD} the dipole-dipole coupling Hamiltonian.

Exchange coupling between electrons takes place for a significant overlap of the singly occupied molecular orbitals of two spins. As a consequence the electrons are exchanged between these orbitals. For non-delocalized electrons this process occurs at distances smaller than 1.5 nm. The exchange interaction is described by

$$H_{\text{exch}} = \mathbf{S}_1^T \mathbf{J} \mathbf{S}_2,$$

with \mathbf{J} as the exchange coupling tensor.

The dipole-dipole coupling between electrons is observed when the spin of one electron is sensing the magnetic moment of the other electron through space. It is described by

$$H_{\text{DD}} = \mathbf{S}_1^T \mathbf{D} \mathbf{S}_2.$$

In the high field approximation and with neglect of \mathbf{g} -tensor anisotropies the dipole-dipole coupling tensor in the principal axis system (coordinate system, in which the off-diagonal elements of the tensor are zero) is given by

$$\mathbf{D} = \frac{\mu_0}{4\pi\hbar} \frac{g_1 g_2 \beta_e^2}{r_{12}^3} \begin{pmatrix} -1 & & \\ & -1 & \\ & & 2 \end{pmatrix} = \begin{pmatrix} -\omega_{\text{DD}} & & \\ & -\omega_{\text{DD}} & \\ & & 2\omega_{\text{DD}} \end{pmatrix}.$$

1.2.1 CW EPR spectroscopy

The majority of the EPR measurements presented here were performed with nitroxide radicals. Sterical hindrance induced by methyl groups surrounding the paramagnetic center, the nitroxide group, results in a high level of molecular stability. Together with a good accessibility this specific molecular stability leads to a wide range of applications for nitroxide spin labels. The impaired electron is predominantly situated in the oxygen and nitrogen orbitals. The generalized molecular frame for nitroxide molecules is visualized in Fig. 1.14. The x axis is orientated along the NO-bond, the z axis is orientated along the $2p_z$ orbital, and the y axis is depicted perpendicular to the letter two.

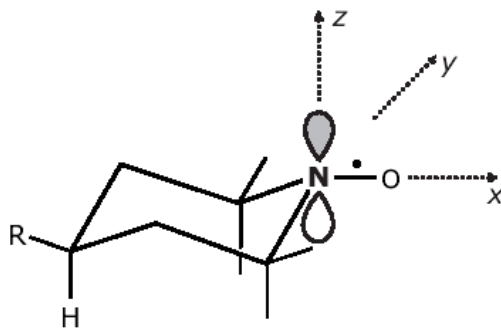


Fig. 1.14. Basic structure and tensor main axes of common nitroxide spin labels.

Small substituents R result in more or less spherical spin label structures and lead to isotropic molecular rotational motions in media of low viscosity. For fast rotations it is sufficient to focus only on the Electron Zeeman and the hyperfine interactions, as mentioned above.

In CW EPR experiments the allowed transitions of the spin system are observed by stepwise adjustments of the external magnetic field but with a constant microwave frequency. Interpretation of CW spectra is described for nitroxide spectra and Cu^{2+} spectra and will be followed by a characterization with reference to the Hamiltonian.

For common measurements of nitroxides at low concentration the electron Zeeman and the hyperfine interaction with ^{14}N reflect the most important contributions to the Hamiltonian:

$$H_0 = \beta_e \mathbf{B}_0^T \mathbf{g} \mathbf{S} / \hbar + \mathbf{S}^T \mathbf{A} \mathbf{I}.$$

For liquid-state spectra the \mathbf{g} -tensor averages to the isotropic g -value (like described before). Additionally, also the dipolar coupling term of the hyperfine interaction vanishes:

$$H = \beta_e S_Z g_{iso} B_0 / \hbar + A_{iso} S_Z I_Z.$$

Solving the time independent Schrödinger equation with this Hamiltonian results in the energy eigen values in frequency units that are given by

$$\omega(m_s, m_I) = \frac{\beta_e g_{iso} B_0 m_s}{\hbar} + A_{iso} m_s m_I$$

where m_I represents the nuclear spin quantum number (-1, 0, +1 for ^{14}N).

Hence, every electron Zeeman energy level is split in three sublevels caused by hyperfine interaction (Fig. 1.15).

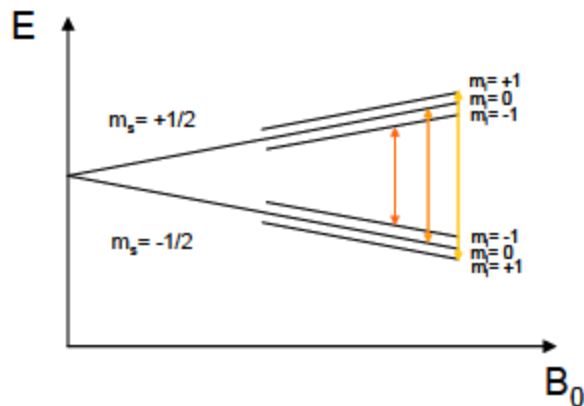


Fig. 1.15. Splitting of the energy levels of a free electron spin in a magnetic field. The arrows indicate the allowed transitions excited by the mw.

These energy levels can be detected by microwave irradiation with frequencies matching the differences between the energy levels ($\Delta m_s=1$, $\Delta m_l=0$). Irradiation of a resonant frequency ω induces transitions between the states $|m_s, m_l\rangle$ and $|m'_s, m'_l\rangle$.

The frequency correlated to the transitions in the spectra is given by

$$\omega = \frac{\Delta E}{\hbar} = \frac{\langle m'_s, m'_l | \mathbf{H} | m'_s, m'_l \rangle - \langle m_s, m_l | \mathbf{H} | m_s, m_l \rangle}{\hbar}.$$

or according to the selection rules ($\Delta m_s = \pm 1$ and $\Delta m_l = 0$):

$$\omega = \beta_e g_{iso} B_0 / \hbar + A_{iso} m_l.$$

Since the frequency of the different transitions is correlated to the applied magnetic field, for technical reasons, in CW EPR measurements the magnetic field is changed, while the frequency is kept constant. The radiation, which is sufficient to induce such transitions in magnetic fields of about 0.3 T is in the microwave region (~ 9 GHz, X-band).

A typical first derivative nitroxide spectrum comprises three lines which are separated by a_{iso} . (Fig. 1.16).

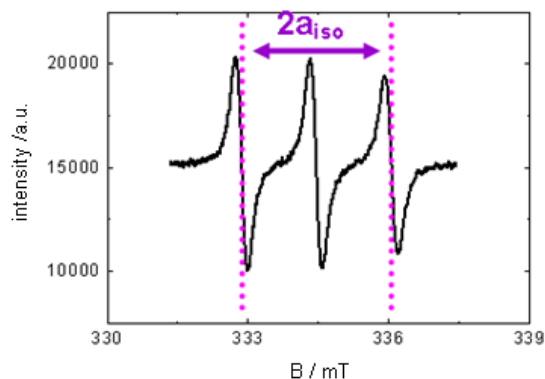


Fig. 1.16. Fast regime CW EPR spectrum at 22 °C (Proxyl IAA in toluene). $2a_{iso}$ is given by the distance between the point of the low field line and the point of the high field line as indicated by the violet dotted lines.

In the slow regime the characteristic hyperfine coupling constant $2A_{zz}$ is determined by the distance between the two outer peaks of the so-called powder spectrum (Fig. 1.17).

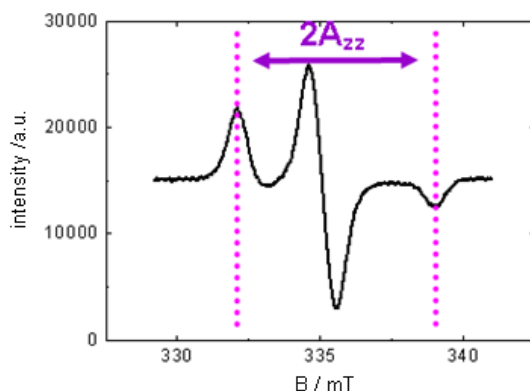


Fig. 1.17. Slow regime CW EPR spectrum at -170 °C (Proxyl IAA in toluene). $2A_{zz}$ is indicated by the distance between the outer peaks as indicated by violet dotted lines.

In the slow regime spectrum no averaging of the g -tensor takes place. Additionally, the dipolar coupling tensor contributes to the spectrum.

As mentioned before, one of the most important features of EPR measurements is the investigation of molecular dynamics. The descriptions of these dynamics are based on a characteristic parameter called rotational correlation time (τ). First, EPR measurements were only able to detect correlation times in nanosecond scale. Nowadays, this time interval increased to values ranging from picoseconds to milliseconds. The EPR spectrum is highly sensitive to molecular dynamics of the spin label. Taking into regard complex interactions like H-bonding, polarity, or viscosity effects, it is therefore absolutely necessary to determine the associated rotational correlation times to get further information about the nature of interaction.⁴⁷

Theory

As for the isotropic motion of spin label molecules the rotational correlation time can be described by Brownian rotational diffusion together with specifications based on the Stokes-Einstein-Diffusion. In magnetic resonance it is common to examine the rotation of tensors of the second grade resulting in the following equation:

$$\tau = \frac{1}{6D_{rot}} = \frac{1}{6R}.$$

R is the rotational diffusion coefficient and is introduced according to the notation of Jack H. Freed.⁴⁸

Motions of spherical spin labels, like TEMPO, in isotropic media resemble isotropic rotational diffusion and can be described by the Stokes-Einstein-Equation and the rotational correlation time τ_r :

$$\tau_R = \frac{4\pi r^3 \eta}{3k_B T}.$$

As described above, the correlation time depends on the radius of solvation r , the viscosity η , and the absolute temperature T ; k_B is the Boltzmann constant.

By rotational motion of spin label molecules the interactions of electron spin and nuclear spin and their local orientation according to the magnetic field are modified temporarily inducing fluctuations in local magnetic fields and resulting in a broadening of the spectral EPR lines. This broadening depends on the hyperfine interaction constant as well as on the g-factor. When parameters are known it is possible to derive the rotational correlation time in the fast regime region directly from the line widths and intensities (Fig. 1.18). For ¹⁴N-nitroxides the rotational correlation time is correlated with the relative intensities of the three transitions I_{+1} , I_0 , I_{-1} and their line widths ΔH_{+1} , ΔH_0 , ΔH_{-1} .⁴⁹⁻⁵⁰

$$\tau_r = 6.7 \times 10^{-10} \Delta H_{+1} \left[\left(\frac{I_{+1}}{I_{-1}} \right)^{1/2} - 1 \right].$$

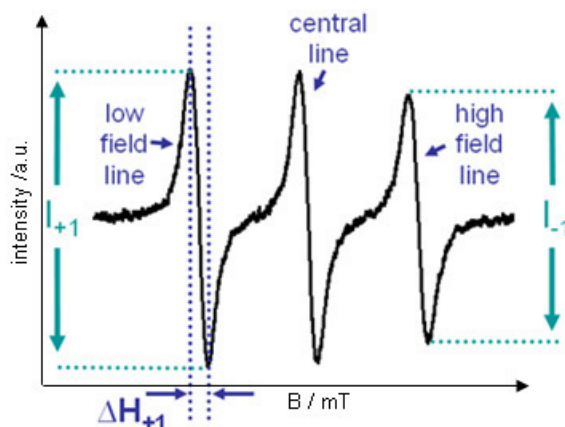


Fig. 1.18. Fast regime CW EPR spectrum at 22 °C (Proxyl IAA in toluene). ΔH_{+1} , represents the line width of the low field line, I_{+1} and I_{-1} , are the line intensities of the low field line and the high field line, respectively.

The spin Hamiltonian for a spin system consisting of a Cu^{2+} ion ($S = 1/2$, $I = 3/2$) together with weakly coupled nuclei can be written as

$$H = \frac{\beta_e}{h} B_o g S + S A^{\text{Cu}} I + H_N.$$

The copper quadrupole interaction is neglected in this description. Further, the \mathbf{g} - and \mathbf{A}^{Cu} -tensors are assumed to be coaxial and axially symmetric. Effects arising from the simultaneous presence of two copper isotopes are neglected, here. The third term H_N represents ^{13}C and proton interactions and is small compared to other contributions. The resulting CW EPR spectrum is described by the principal values g_{\parallel} , g_{\perp} , A_{\parallel} , A_{\perp} of the \mathbf{g} and \mathbf{A}^{Cu} tensors (Fig. 1.19).

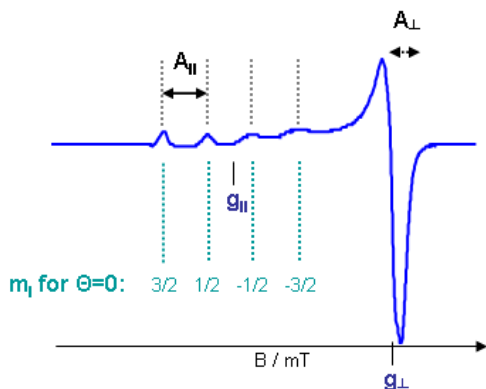


Fig. 1.19. Cu^{2+} powder CW EPR spectrum recorded at 77 K depicting the characteristic EPR parameters g_{\parallel} , g_{\perp} , A_{\parallel} , and A_{\perp} .

For a typical powder EPR spectrum of an axially elongated copper complex $g_{\parallel} > g_{\perp}$ and $A_{\parallel} > A_{\perp}$ is found. The spectrum reflects a superposition of four axial powder lines which can be assigned to the different m_l states (the angle θ is defined as the angle between the z -axis and the external magnetic field vector B_0). The parameters g_{\parallel} and A_{\parallel} can be obtained easily from the g_{\parallel} -region of the spectrum. The determination of g_{\perp} and A_{\perp} , though, is more challenging due to unresolved features in the g_{\perp} -region.

1.2.2 Pulse EPR spectroscopy

With pulse EPR spectroscopy, it is possible to separate contributions to the overall spin Hamiltonian and thus to selectively study one specific interaction like e.g. the electron nuclear interaction in an ESEEM experiment or the electron-electron dipolar interaction in a DEER experiment. Here, in general, the electromagnetic field is irradiated only in certain time intervals, called pulses. The pulses change the spin state, which can be described as a change of the angle of the magnetization vector with respect to the external B_0 -field in the classical view. This flip of the total magnetization depends on the B_0 -field amplitude of the applied pulse as well as the length of the pulses. A 90° ($\pi/2$) pulse creates spin coherence, while a 180° (π) pulse inverts magnetization in the quantum mechanical picture. The time between the pulses is called evolution time and allows the system to evolve under the influence of the Hamiltonian.

To describe the time evolution of the spin, the time-dependent Schrödinger equation is used:

$$\frac{d}{dt}|\psi\rangle = -iH(t)|\psi\rangle$$

$$\frac{d}{dt}\langle\psi| = i\langle\psi|H(t).$$

Theory

In EPR experiments not only one spin is observed but an ensemble of electron spins that may feature different states. Therefore the ensemble of quantum mechanical particles is described by a density matrix.

The general basics for the description of a density matrix can be derived from the wave function $|\psi\rangle$. Here, the spin of the electron in the magnetic field can be observed in one of the two eigenstates denoted as α and β , which are characterized by the quantum number m_s . The wave function for a spin is represented as a superposition of two states that are characterized by the wave functions $|\alpha\rangle$ and $|\beta\rangle$, with the respective complex coefficients c_α and c_β

$$|\psi\rangle = c_\alpha |\alpha\rangle + c_\beta |\beta\rangle.$$

The probability of a particular spin state for the electron is represented by the square of these coefficients. A "pure" state is represented by one state condition and the same coefficients c_α and c_β . The wave function for N spins is then described by $|\psi\rangle^N$.

Any ensemble of spins can be described by a superposition of n sub-ensembles in pure states. These pure states are determined by the wave functions $|\psi_l\rangle$ and the correlated probabilities p_l .

The ensemble average is defined as

$$\overline{|c_\alpha|^2} = \sum_l p_l |c_\alpha^{(l)}|^2.$$

Ensemble averages of other coefficients are computed analogously.

The correlated density matrix for a spin with $S=1/2$ can be derived from the ensemble averages and is given by

$$\sigma = \begin{pmatrix} \overline{|c_\alpha|^2} & \overline{c_\alpha c_\beta} \\ \overline{c_\alpha c_\beta} & \overline{|c_\beta|^2} \end{pmatrix}.$$

The difference between the diagonal elements is referred to as polarization and is proportional to the longitudinal magnetization. Off-diagonal elements are correlated to coherence, with a magnitude which is proportional to the transverse magnetization.

Another term for the expression of the density matrix of any spin system is given by:

$$\sigma = \sum_{kl} \overline{c_l c_k} |l\rangle\langle k|,$$

with the two states of the spin system $|l\rangle$ and $|k\rangle$. This term represents all data accessible by EPR measurements.

The time evolution of the density matrix is described by the Liouville-von Neumann equation:

$$\frac{d}{dt}\sigma(t) = -i(H(t)\sigma(t) - \sigma(t)H(t)).$$

Using this equation the spin ensemble can be described within the pulse experiment. For a time-independent Hamilton operator the density matrix at the time t is

$$\sigma(t) = \exp(-iHt)\sigma(0)\exp(iHt) = U(t)\sigma(0)U(t)^\dagger,$$

with the propagator element $\exp(-iHt) = U(t)$. For a time-dependent Hamiltonian, the integration of the Liouville-von Neumann equation is not as easy as in the former case. Alternative approaches therefore introduce a Dyson time-ordering operator or subdivide the evolution of the spin system into sufficiently small intervals with a constant Hamiltonian.

The expectation value of the observable O from the density matrix can be determined by

$$\langle o \rangle = \text{tr}\{\hat{O}\sigma\},$$

with the operator \hat{O} . This description enables to determine the outcome at any time. Since relaxation effects were neglected so far for a more general description of a quantum mechanical system, a relaxation superoperator Ξ has to be introduced:

$$\frac{d}{dt}\sigma(t) = -i(H(t)\sigma(t) - \sigma(t)H(t)) - \Xi(\sigma(t) - \sigma_{eq}),$$

with σ_{eq} representing the density operator at thermal equilibrium. In the description of pulse sequences, relaxation effects are usually neglected.

In the following sections all pulse experiments performed during this work are theoretically explained step by step. At this point, a standard model system is introduced with one electron spin $S=1/2$ and one nuclear spin $I=1/2$, which is in thermal equilibrium and depicted as a four level scheme (Fig. 1.20).⁴⁶

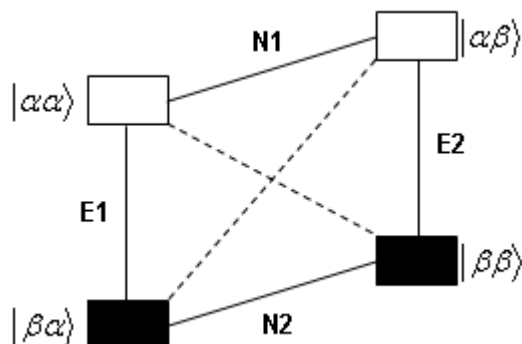


Fig. 1.20. Four-level scheme for a system consisting of an electron spin=1/2 and a nuclear spin $I=1/2$ at thermal equilibrium. The allowed electron Zeeman transitions are indicated by vertical lines (E1, E2), allowed nuclear transitions by horizontal lines (N1, N2). Also the forbidden transitions, which violate the selection rules mentioned above, are presented (indicated by dashed lines).

The overall state of the spins is determined by $m_s, m_l = 1/2 \equiv \alpha$ and $m_s, m_l = -1/2 \equiv \beta$, resulting in the four possible spin states $|\alpha\alpha\rangle, |\beta\alpha\rangle, |\alpha\beta\rangle$, and $|\beta\beta\rangle$, the first letter denoting the state of the electron spin the second one denoting the state of the nuclear spin. The allowed electron Zeeman transitions are labeled “E1” and “E2”, the nuclear Zeeman transitions “N1” and “N2”, respectively. Forbidden transitions are indicated by dashed connectors. The 16 Cartesian basis operators for this system are calculated as the Kronecker product of the basis sets

$$\{B_1, B_2, \dots, B_{16}\} = \{S_x, S_y, S_z, 1\} \otimes \{I_x, I_y, I_z, 1\}$$

and are characterized in Table 1.1.

Table 1.1. Cartesian operators based on the four-level scheme.

<i>product operator</i>	<i>interpretation</i>
$\frac{1}{2} 1$	unity operator
S_x, S_y, I_x, I_y	electron/nuclear coherences
S_z, I_z	electron/nuclear coherences
$2 S_z I_z$	longitudinal electron-nuclear two-spin order
$2 S_x I_z, 2 S_y I_z$	electron coherence in anti-phase
$2 S_z I_x, 2 S_z I_y$	nuclear coherence in anti-phase
$2 S_x I_x, S_y I_y$	electron coherences and electron-nuclear double/zero
$2 S_x I_y, S_y I_x$	quantum coherences

Theory

In the equilibrium state of a spin experiment with dominating electron Zeeman interaction (following the high-temperature approximation), the initial spin state is simply the spin component orientated antiparallel to the direction of the quantization axis, which is determined by the external field. The same applies for the macroscopic magnetization. With regard to the micro wavepulses of length t_p applied in pulse EPR measurements the resonance condition is correlated to a flip of the overall magnetization by the flip angle β

$$\beta = \omega_1 t_p .$$

Not only the flip angle but also the excitation bandwidth, which represents the fraction of excited spins, depends on the pulse duration and can be characterized in the frequency domain by

$$FWHM \approx \frac{1.207}{t_p} .$$

Shorter values for t_p thereby result in larger excitation bandwidths. Pulses can be regarded as *selective* in the case when only one transition of a spin (or a nucleus) is excited or as *non-selective*, when all allowed or partially allowed transitions are excited. An ideal non-selective pulse acting on a spin in the S_z state from the x-direction of the rotating frame is described within the following transformation

$$S_z \xrightarrow{\beta_x} \cos \beta S_z - \sin \beta S_y .$$

Detection of the magnetization after application of the different pulse sequences is performed in the x- y-plane of the rotating frame in the phase sensitive quadrature detection mode, giving rise to a real and an imaginary component of the measured signal.

With reference to pulse EPR measurements with Cu^{2+} representing the EPR-active atom several characteristic theoretical aspects should be highlighted, which are different from those with standard nitroxide spin labels. In this context, the most important difference is given by the much broader copper spectrum itself. The limited bandwidth of the MW pulses of standard pulse EPR measurements accounts for the limitation, that only a small part of the EPR spectrum is excited. At a given B_0 position spin packets from different m_l states with different θ values can thus contribute to the spectrum.

1.2.2.1 The electron spin echo (ESE) experiment

One of the simplest pulse EPR experiments is based on detection of the primary echo, which describes the re-appearance of magnetization of the initial magnetization after a pulse sequence of $(\pi/2)-\tau-(\pi)-\tau$ -echo. Neglecting relaxation of the spin system, this experiment can be described based on the Cartesian operators by

$$S_z = \sigma_{eq} \xrightarrow{(\pi/2)S_x} \sigma_1 = S_y \xrightarrow{\text{free-evolution}} \cos(\Omega_s \tau) S_y - \sin(\Omega_s \tau) S_x$$

$$\sigma_2 = \xrightarrow{(\pi)S_x} \sigma_3 \xrightarrow{\text{free-evolution}} \sigma_4 = -\cos(\Omega_s \tau) S_y - \sin(\Omega_s \tau) S_x,$$

with the precession frequency Ω_s of the individual spin packets about the z-axis in the rotating frame. The sequence starts with a $\pi/2$ pulse transforming the equilibrium magnetization form S_z along -y. After a free evolution time (τ) the different spin packets fan out into the xy plane. Then a π pulse is applied to the system (irradiated from the x axis) which converts the phases of the y components of the overall magnetization. After an additional time τ the spins refocus to give rise to an echo of the originally inverted spin packets, which is observable along the y axis after the time $2\tau + \tau_1 + \tau_2$ (τ_1, τ_2 represent pulse durations for the pulses p_1 and p_2).

In general, it should be mentioned that this method cannot refocus magnetization of spins that have relaxed during the measurements. Thus the final echo intensity is strongly dependent on the phase memory time and refocuses only the inhomogeneously broadened signals.⁵¹ Based on this sequence, ESE-detected EPR is a technique where the pulse sequence is repeated several times during a sweep of the magnetic field (Fig. 1.21).

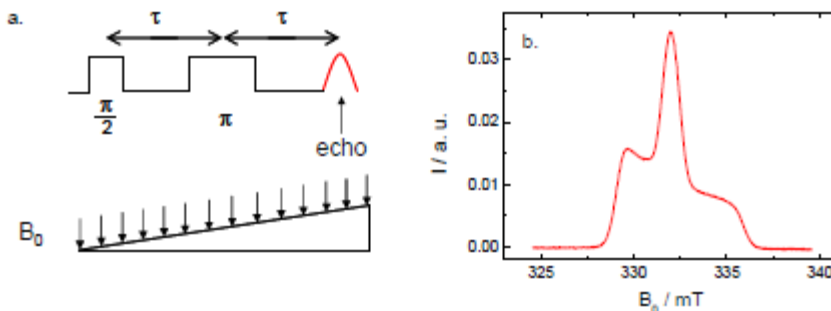


Fig. 1.21. **a:** ESE pulse sequence. **b:** typical ESE-detected EPR spectrum (adopted from A. Volkov).

1.2.2.2 The 2-pulse ESEEM experiment

2-pulse ESEEM is an experiment where the dependence of the overall intensity of the echo from the phase memory time T_m is used to measure T_m itself. During the measurement, the evolution time τ is incremented in steps of $\Delta\tau$ (Fig. 1.22).

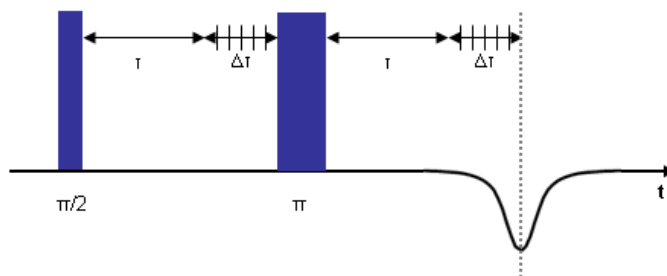


Fig. 1.22. 2-pulse ESEEM/ T_2 pulse sequence with the characteristic measurement parameters

$V(2\tau)/V(0)$ can be analyzed as a function of $\tau + \Delta\tau$ by an exponential decay with the characteristic time T_m :

$$\frac{V(2\tau)}{V(0)} = \exp\left[\frac{-2\tau}{T_m}\right].$$

If the spin system cannot be described by only one single phase memory time, the decay can be fitted by a stretched exponential decay function (like it was done in the present work). The exponential decay in the time data is superimposed by oscillations (modulations) with a certain frequency, and can be analyzed analytically by Fourier-transformation of the time-domain to the frequency domain. This modulation originates from weak hyperfine couplings of the detected electron spin to magnetic nuclei.

1.2.2.4 The Instantaneous Diffusion experiment

The “local” concentration of spins in a nitroxide EPR sample was determined by instantaneous diffusion measurements. Instantaneous diffusion is an effect observed at higher spin concentrations leading to increased relaxation during an echo experiment (2p-ESEEM). If this takes place there is a correlation between the concentration of spins (C), the phase recovery time (T_{ID}) and the mw pulse flip angle of a pulse EPR experiment (β). For nitroxides this correlation is given by

$$\frac{1}{T_{ID}} = \frac{C\pi\mu_0 g_1 g_2 \beta_e^2}{\hbar 9\sqrt{3}} \sin^2\left(\frac{\beta}{2}\right).$$

By plotting $1/T_{ID}$ against $\sin^2(\beta/2)$ the concentration C can be retrieved. The resulting concentration of “local” spins can be compared to the real physical concentration of spins labels in order to reveal effects like e.g. aggregation of bio-molecules.

In general, this measurement is based on the same pulse sequence as used for 2-pulse ESEEM. In order to gain information about the correlation of T_m and the mw pulse flip angle the simplest approach is to vary the microwave attenuation, which is directly related to the flip angle by

$$\beta(a) = \beta(r) \sqrt{10^{\frac{dB(r)}{10} - \frac{dB(a)}{10}}}$$

where $\beta(a)$ is the actual flip angle after changing the microwave attenuation, $\beta(r)$ the optimized reference flip angle (was set as near as possible to 180°), and $dB(a)$ and $dB(r)$ the correlated values of microwave attenuation.

1.2.2.5 The 3-pulse ESEEM experiment

3-pulse ESEEM represents a pulse EPR technique which is based on stimulated echos. It is based on the characteristic pulse sequence $(\pi/2)-\tau-(\pi/2)-T-(\pi/2)-echo$ (Fig. 1.23).

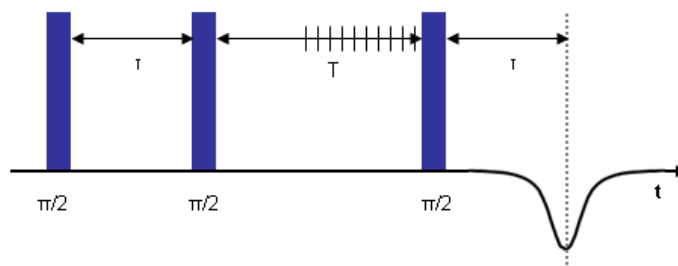


Fig. 1.23. 3-pulse ESEEM pulse sequence with the characteristic measurement parameters.

In the vector picture the two $\pi/2$ -pulses account for a polarization grating along the z direction, which is stored there for the time T . The polarization grating is spaced by $1/\tau$ and decays with the spin lattice relaxation time T_1 ($>T_m$ for most solids). During this comparatively large time span T , additional pulses can be irradiated. The last $\pi/2$ pulse transfers the polarization pattern to the xy plane allowing standard detection of the refocused echo. The spin density operator σ at a time t is described by

$$\begin{aligned} \sigma(\tau + T + t) = & -\frac{1}{2} [\cos(\Omega_s(t - \tau)) + \cos(\Omega_s(t + \tau))] S_y \\ & + \frac{1}{2} [\sin(\Omega_s(t - \tau)) + \cos(\Omega_s(t + \tau))] S_x . \end{aligned}$$

Theory

When there is hyperfine coupling between the detected electron spin and magnetic nuclei in the vicinity characteristic modulations are observed within the spectrum.

The typical 3-pulse ESEEM pulse sequence is given by an additional increment of T and is based on the common pulse sequence to produce a stimulated echo. This allows a detection of a time decay which can be described fitting a stretched exponential function to the data in time-domain:

$$\frac{V_{3-p}(\tau, T)}{V(0)} = \exp\left[\frac{-T}{T'}\right]^x.$$

After background correction the characteristic modulations become even more apparent and are accessible by Fourier transformation, which finally results in a determination of the hyperfine couplings in the frequency domain.

Proceedings during the experiments are again best described by the model system with $S=1/2$, $I=1/2$. In the first part of the experiment, up to the end of the first free evolution interval (after time τ) the system exactly behaves like it was described for the 2-pulse ESEEM experiment. Then the characteristic $\pi/2$ -pulse within the 3-pulse ESEEM sequence induces nuclear coherence. After that the nuclear coherence is redistributed from the allowed E1 transition to E2 or the forbidden transitions. As a consequence, also off-diagonal elements in the density matrix are populated. These elements can now evolve with the nuclear frequencies ω_{N1} and ω_{N2} and gain the phase $\phi_{N1} = \omega_{N1}T$. The last pulse accounts for a transfer of the nuclear coherence back to electron coherence and finally results in an electron echo.

1.2.2.6 The HYSCORE experiment

The HYSCORE experiment is a specific modification of the 3-pulse ESEEM experiment. Here, an additional non-selective π pulse is added to the sequence of 3-pulse ESEEM between the second and the last $\pi/2$ pulse, which inverts all spins (Fig. 1.24).

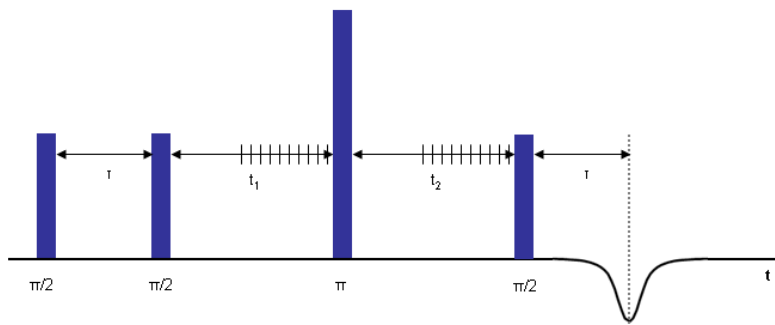


Fig. 1.24. HYSCORE pulse sequence with the characteristic measurement parameters.

Additionally, the time t_1 between the second $\pi/2$ pulse and the π pulse and t_2 between the π pulse and the last $\pi/2$ pulse are incremented independently from each other, which finally results in the 2D spectra obtained by HYSCORE measurements.

1.2.2.7 The DEER experiment

Since the EPR spin Hamiltonian also contains a contribution $H_{DD,e}$, which describes weak dipolar couplings between electron spins, it is also possible to obtain information about the distance distribution between electron spins in a system, as there is a r_{12}^{-3} -dependence of the dipolar coupling. The characteristic DEER pulse sequence is depicted in Fig. 1.25.

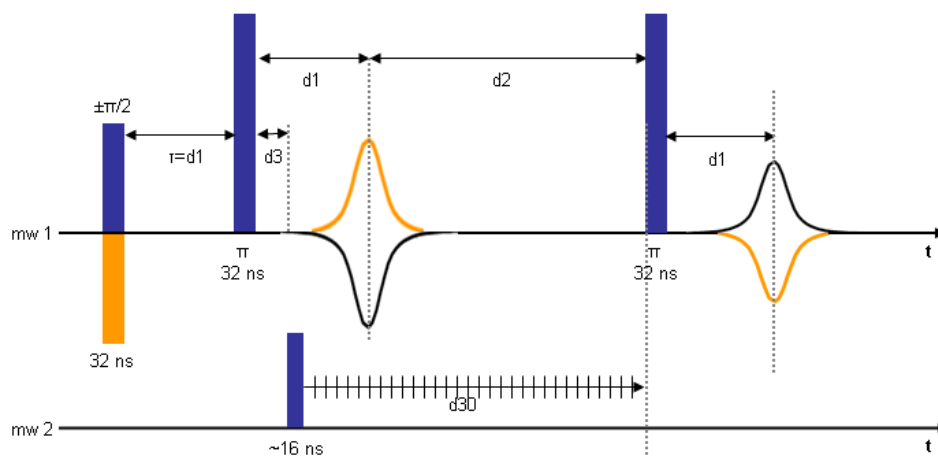


Fig. 1.25. DEER pulse sequence with the characteristic measurement parameters.

Theory

Here, an 'observer' experiment with a refocused echo is performed on spin packets '1' with frequency ω_1 (mw 1), while on spins '2' a π (pump) pulse is applied with resonance frequency ω_2 (mw 2). The irradiation time of the pump-pulse is varied between the position of the primary echo (which is not detected but dephases again) and the last π -pulse of the observer sequence. Spins '2' are thus inverted by the π -pulse. This results in a changed magnetic field at the position of the '1' spins. Therefore the precession of the '1' spins changes and magnetization features a phase difference of $\Delta\phi_{DD} = \omega_{DD}t$. Finally, the echo intensity of the refocused echo is recorded as a function of the pump pulse position t .

Extraction of distance data from this record is based on

$$\omega_{DD} = \frac{\mu_0 g_1 g_2 \beta_e^2}{4\pi\hbar} \frac{1}{r_{12}^3}.$$

The distance range, which is accessible by DEER measurements is limited at the lower scale to ~ 1.5 nm by the technical excitation bandwidth of the mw pulse generators at X-band frequencies. Pulses which are closer than 1.5 nm feature stronger dipolar couplings with frequencies > 35 MHz, which significantly exceeds the excitation bandwidth. The limitation at the upper scale is directly determined by the dipolar evolution time and allows for detection of a theoretical maximum distance of ~ 8 nm. Larger distances only contribute to the homogeneous background signal.

2. Materials and Methods

2.1 Technical equipment and Chemicals

2.1.1 Technical equipment

EPR CW-spectrometer (X-band):

MiniScope MS200 with a TE102 rectangular resonator, *mt* magnettech GmbH Analysemesstechnik, Berlin;

Temperature Controller HO2, *mt* magnettech GmbH Analysemesstechnik, Berlin;

Frequency Counter Model 3200, XL-Microwave Inc. Oakland (CA) USA.

EPR pulse-spectrometer (X-band):

Bruker Elexsys 580 EPR spectrometer with a Bruker Flexline split-ring resonator ER 4118X_MS3, Bruker biospin GmbH, Wikingstraße 13, Mühlburg, Karlsruhe, Germany;

Closed cycle cryostat (ARS AF204, customized for CW and pulse EPR, ARS, Macungie, PA, USA);

Temperature controller, Lake Shore Cryotronics, Inc., 575 McCorkle Blvd, Westerville, OH 43082-8888, USA;

Frequency counter & X-band magnet, Bruker biospin GmbH, Wikingstraße 13, Mühlburg, Karlsruhe, Germany;

Vacuum pump, Pfeiffer Vacuum GmbH, Berliner Straße 43, 35614 Asslar, Germany.

Further technical equipment:

Standard stock Max-Planck-Institut für Polymerforschung, Mainz.

2.1.2 Chemicals

Glycerol:

$C_3H_5(OH)_3$, molecular weight: 92.09 g/mol

Fluka, purity: 87%, H_2O : 12-14%

Sodium chloride:

NaCl, molecular weight: 58.44 g/mol
Riedel-de Haën, purity: 99.8%, H₂O: 0.005%

Copper(II)chloride:

CuCl₂, molecular weight: 134.45 g/mol
Aldrich, purity 99%

Phosphate buffer (pH 7.4):

50 mM, pH was adjusted with HCl

TRIS buffer (pH 7.4):

50 mM, pH was adjusted with HCl

2.2 Sample preparation

2.2.1 Non-spin-labeled MBP

MBP C1 (the least modified charge isoform) was kindly provided by Prof. Dr. George Harauz. MBP and myelin membranes were isolated from human spinal cord stored frozen at ~ -80 °C. MBP was then extracted from delipidated nervous tissue with dilute ice-cold HCl at pH 3. Pepstatin A (1 µg/ml) and 2 mM EDTA were added to the extracts to prevent proteolytic breakdown and to remove divalent metal ions from MBP. MBP was then further purified by anion exchange column chromatography on DEAE-TSK (650) at pH 10.4. The purified protein was then freeze-dried and stored frozen for further sample preparations. For EPR measurements the lyophilized MBP was dissolved in TRIS or phosphate buffer (50 mM, pH 7.4) at concentrations of about 1 mM and Cu²⁺ was added *ad lib.* (typical final Cu²⁺ concentrations: 1 mM). The sample solution - together with 25% (v/v) glycerole - was transferred into home made 3 mm quartz capillaries. The samples were then frozen in isopentane in order to form a stable glassy state of the sample volume and never again thawed before measurements.

2.2.2 Spin-labeled MBP in solution

The protein was purified following a well established biochemical protocol. This was again performed in the lab of Prof. Dr. George Harauz. Single cystein mutants of rmC1 were purified from BL21-CodonPlus (DE3)-RP *Escherichia coli*. Spin labeling of mutants was performed using a column matrix and a 10-fold molar excess of [1-oxyl-2,2,5,5-tetramethyl-D-pyrroline-3-methyl]methanethiosulfonat (Toronto Research Chemicals, Toronto) in 20 mM Hepes-NaOH (pH 7.4), 6 M urea, and 10 mM NaCl at 4 °C overnight. The column was repacked and washed to remove spin probe excess and labeled proteins were eluted and dialyzed against 20 mM Hepes-NaOH (pH 7.4) and 10 mM NaCl. The sample was then frozen, stored and ready for further preparation. For EPR measurements without artificial membranes the spin-labeled protein was gently thawed diluted with unlabeled MBP *ad lib.* and transferred into home made 3 mm quartz capillaries. The samples were then frozen in isopentane in order to form a stable glassy state of the whole sample volume and never again thawed before measurements. Typical concentrations for measurements were ~ 0.3 mM.

2.2.3 Spin-labeled MBP in artificial membrane vesicles

The purified, spin labeled MBP C1 was prepared like it is described above (chapter 3.2.2). LUVs with a lipid composition similar to that of the cytoplasmic monolayer of myelin (Cyt-LUVs; cholesterol, phosphatidylethanolamine, phosphatidylserine, PC, sphingomyelin, phosphatidylinositol in 44:27:13:11:3:2% molar percentages) were prepared by extrusion in the laboratory of Prof. Dr. George Harauz. Lipids were purchased from Avanti Polar Lipids and prepared in 20 mM Hepes-NaOH, 10 mM NaCl, pH 7.4, for EPR experiments and added to the spin labeled MBP. The sample volume was then gently transferred into home made 3 mm glass capillaries and never again thawed before measurements. Samples were prepared in LUVs (lipid content like described above) with a lipid-to-protein ratio (LPR) of 378:1 for MBPI and 567:1 for MBPII with a final protein and spin concentrations of about 0.2 mM. MBPIII was prepared in MLVs (15 mol-% DSPG, 85 mol-%DSPC) with an LPR of 567:1 and a final protein and spin concentration of about 0.13 mM.

2.3 EPR spectroscopy

2.3.1 Experimental procedure

2.3.1.1 CW EPR measurements

CW EPR spectra were performed on a MiniScope MS200 spectrometer at variable temperatures. For measurements at room temperature 1 mm quartz capillaries were used and fixed within the spectrometer without further technical equipment (no temperature controlling unit). For measurements at 103 K nitrogen cooling was used and regulated by a TC HO2 temperature controller. Here, home made 3 mm quartz capillaries were used for measurements. Measurements at 77 K were performed within a dewar filled with liquid nitrogen, which could be directly inserted into the resonator of the spectrometer. For the measurements it was checked that the typical microwave power of 10 W applied during the measurements did not result in saturation broadening of the obtained EPR spectra. The modulation amplitude was set to values of about 1/5 of the spectral line width of the central line of the EPR spectra. The sweep width was 12 mT for measurements with Cu^{2+} , 0.8 mT for measurements with spin-labeled MBP at room temperature and 1.5 mT for measurements of spin labeled MBP at 77 or 103 K. Spectra were detected with 4096 data points and a scan time of 60 s. The number of averaged scans was individually adjusted according to signal quality.

2.3.1.2 Pulse EPR measurements

X-band pulse EPR measurements were performed on a Bruker Elexsys 580 EPR spectrometer with a Bruker Flexline split-ring resonator ER 4118X_MS3. The resonator was overcoupled to $Q \sim 100$. Pulse EPR measurements were performed at 8 K for measurement with Cu^{2+} samples and at 20 or 50 K for measurements with MTSSL-labeled MBP with a closed cycle cryostat (ARS AF204, customized for CW and pulse EPR, ARS, Macungie, PA, USA). The 3 mm quartz capillaries containing the frozen sample volume were inserted into the resonator at 50 K.

- ESE-detected measurements were performed using a Hahn echo sequence $\pi/2 - \tau - \pi - \tau - \text{echo}$ and a 1.8 mT field sweep. The interpulse delay time τ was 200 ns and the pulse lengths were 16 ns for $\pi/2$ pulse and 32 ns for π pulse. The integration gate length was set to 100 ns.

- The transversal relaxation experiments (T_2) were performed based on a Hahn echo sequence $\pi/2 - \tau - \pi - \tau - \text{echo}$. The initial interpulse delay of 200 ns was incremented by 8 ns. The integrated

echo intensity was measured as a function of this increment with an integration gate length of 32 ns centered at the echo maximum and at a position of $B_{max}-0.25$ mT (Fig. 2.1). The pulse lengths were 16 ns for the $\pi/2$ pulse and 32 ns for the $\tilde{\pi}$ pulse.

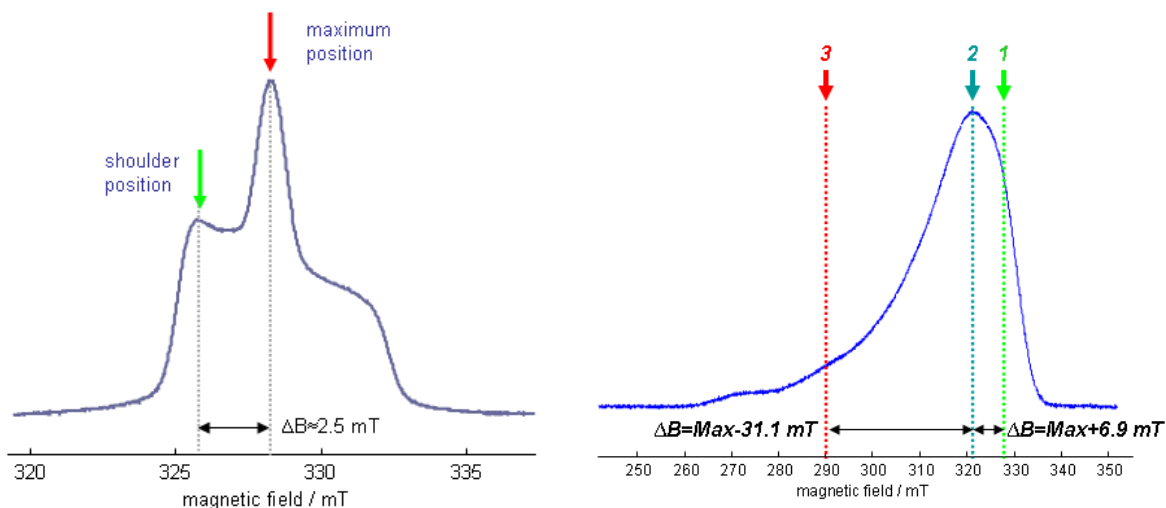


Fig. 2.1. Detection positions for the ESEEM based measurements (T_2) for measurements with MTSSL spin-labels (left) and Cu^{2+} (right). For measurements with MTSSL the red arrow indicates detection at the maximum position of the correlated ESE spectrum. The green arrow represents the position of the magnetic field for detection at the shoulder position of the correlated ESE spectrum, which represented a shift of about 2.5 mT towards a lower magnetic field from the maximum position. Within the Cu^{2+} measurements detection positions referred to as '1,' '2,' and '3' are depicted in the correlated ESE spectrum on the right, with $\Delta B_z = -31.1$ mT and $\Delta B_z = +6.9$ mT with regard to the detection position at the maximum ('2').

- Instantaneous Diffusion measurements (based on the T_2 measurement setup) were performed using a Hahn echo sequence $\pi/2 - \tau - \pi - \tau - echo$. The initial interpulse delay of 200 ns was again incremented by 8 ns. The integrated echo intensity was measured as a function of this increment with an integration gate length of 32 ns centered at the echo maximum and at a position of $B_{max} - 0.25$ mT (Fig. 2.1). The pulse lengths were 16 ns for the $\pi/2$ pulse and 32 ns for the $\tilde{\pi}$ pulse. Attenuation (dB_{min}) of the pulses was optimized by minimizing the echo intensity for the zero pulse amplitude by microwave attenuation. The microwave attenuation was then increased step-by-step (1 dB increments) in order to acquire T_2 data for a maximum number of microwave attenuations.

- 3-pulse ESEEM measurements were performed with a $\pi/2 - \tau - \pi/2 - T - \pi/2 - \tau - echo$ pulse sequence and a 4-step phase cycle. The pulse length of the $\pi/2$ pulses was 16 ns and the interpulse delay $d_1 = 136$ ns or 176 ns (selection based on proton blind spots) was kept constant. The second interpulse delay time T with initial value of 80 ns was incremented in steps of 8 ns. The integration gate length was 32 ns.

Materials & Methods

- HYSORE experiments were performed based on the pulse sequence of 3-pulse ESEEM, and an additional sharp π -pulse (stemming from a second microwave channel), which inverts all spins. The resulting pulse sequence is $\pi/2$ - τ - $\pi/2$ - t_1 - π - t_2 - $\pi/2$ - τ -echo with a [(+x +x +x)-(+x +x +x)-(+x +x -x)+(+x +x -x)+(-x +x +x)-(-x +x +x)-(-x +x -x)+(-x +x -x)] phase cycle. Variation of both t_1 and t_2 results in the characteristic 2D detection of the HYSORE experiment. t_1 and t_2 are incremented in steps of 16 ns with starting values of 300 ns. τ is adjusted according to proton blind spots in a range of about $100 \leq \tau \leq 300$ ns. 256x256 data points were detected for each scan. An additional 8-fold phase cycle (see below) is used for signal optimization (reduction of unwanted echos). The pulse length of the +x/-x-channel was set to 8 ns ($\pi/2$ -pulse) and 16 ns (π -pulse). The pulse length of the +<x>/-<x>-channel was fixed to 16 ns ($\pi/2$ -pulse) and 32 ns (π -pulse).

The magnetic field positions selected for the measurements with MBP and Cu^{2+} were at the maximum position of the correlated ESE spectrum (referred to as '2'), a position of Max -311 G (referred to as '3') and the position of the maximum +69 G (referred to as '1', Fig. 2.2). This was done in order to obtain information about a possible effect of spin orientation on the resulting T_2 times.

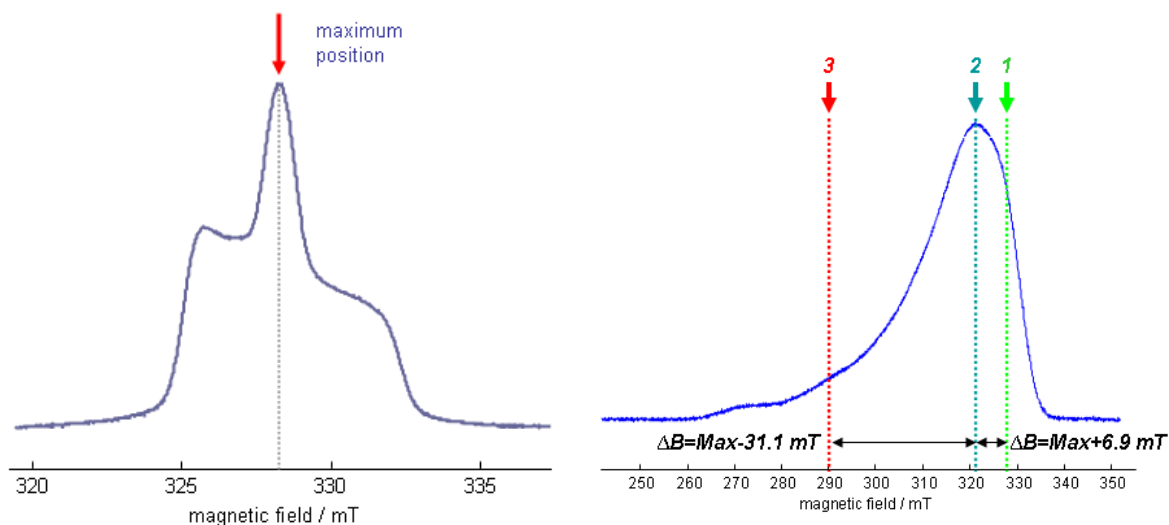


Fig. 2.2. Detection positions for HYSORE and 3-pulse ESEEM measurements with MTSSL spin-labels (left, detection at maximum position of the correlated ESE spectrum) and Cu^{2+} (right), with orientation selection of spins in z-orientation (red), y-orientation (petrol), and x-orientation (light green), referred to as '1', '2', and '3'.

- DEER experiments were performed with a $\pi/2(v_{observer})-\tau_1-\pi(v_{observer})-t'-\pi(v_{pump})-(\tau_1+\tau_2-t')-\pi(v_{observer})-t_2$ -echo pulse sequence with a [(+x)-(-x)] phase cycle applied to the $\pi/2$ pulse. The time t' was incremented in steps of 8 ns. The time $\tau_1 = 200$ ns was kept constant. τ_2 was varied between 1 μ s and 2.4 μ s depending on the T_2 relaxation properties of the sample and distance that needed to be measured. The dipolar evolution time is defined as $t = t' - \tau_1$. Data analysis was performed for $t > 0$ ns. The pump frequency (v_{pump}) was set to the center of the resonator dip that coincides with the maximum of the nitroxide EPR spectrum, whereas the observer frequency ($v_{observer}$) was set to $v_{pump} + 70$ MHz for measurements with MTSSL (for copper measurements $v_{observer}$ was swept within +630 MHz to -190 MHz) and coincided with the low field local maximum of the spectrum for MTSSL (shoulder position in Fig. 2.3). The observer pulse lengths were 32 ns for both $\pi/2$ and π pulses. The π pump pulse length was 12 ns. The width of the integrator gate was 32 ns.

The measurement time of DEER experiments was typically around 4 hours for standard measurements up to 96 hours for long time measurements.

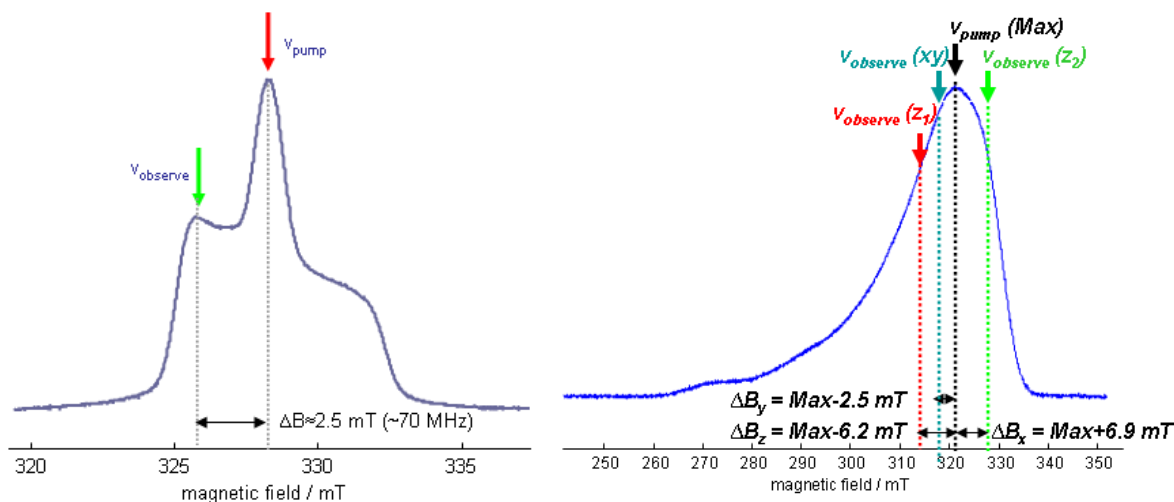


Fig. 2.3. Spin selection of the DEER experiment based on different frequencies of observer- and pump-pulses. DEER measurements with spin labeled MBP (left): The correlating positions within the ESE spectrum are indicated by a red arrow for v_{pump} and green arrow for $v_{observer}$. The difference of about 70 MHz resembles the difference ΔB between the spectral maximum and the low field local maximum of the spectrum. Cu^{2+} DEER measurements with unlabeled MBP (right): Positions for the detection of the DEER experiments are based on a fixed position of the pump pulse but variable positions of the observer pulse ('x', 'z1', 'z2').

2.3.2 Data analysis

EPR data were analyzed based on MATLAB R2007b with the EasySpin program package for EPR spectroscopy.⁵²

2.3.2.1 CW EPR experiments

The characteristic $2A_{zz}$ values were obtained from the CW data directly out of the original or pseudo-modulated spectra using MATLAB software. All presented CW EPR spectra were background corrected by subtracting the first order polynomial fitted on the first and last 10% of the spectral data points for measurements with MTSSL (based on home written MATLAB software). For the relatively broad copper spectra with sweeps of 1.2 mT data was background corrected by subtraction of a reference baseline spectrum for each measurement condition followed by the typical standard baseline correction presented already (*i.e.* subtracting the first order polynomial fitted on the first and last 10% of the spectral data points). For plots containing more than one CW spectrum the magnetic field axes were adjusted according to their resonance frequencies and B_0 -field.

2.3.2.2 ESE measurements

Spectral data obtained by ESE-detected measurements was analyzed based on a home written MATLAB program. First the phase of the quadrature-detected ESE data is optimized (minimizing the imaginary part of the spectra). Then a base line correction is performed subtracting the first order polynomial fitted on a user selected range of data points in the beginning and the end of the spectra. If necessary ESE detected spectra were pseudomodulated according to the modulation used for detection (standard: 0.25 mT for pseudo-modulation).

2.3.2.3 2-pulse ESEEM measurements

Since the relaxation curves could not always be fitted by mono- or biexponential decay functions, a home written MATLAB program has been used fitting a stretched exponential to the experimental data.⁵³ This was performed with three fixed starting points, which were set to the beginning of the original time traces and defined the starting position of the stretched exponential

fitting procedure. The resulting mean value for the relaxation time $\langle T_2 \rangle$ was transferred to the final T_2 time by application of the William-Watts-Relation⁵⁴

$$\langle T_2 \rangle = \frac{1}{x} \cdot T_2 \cdot \Gamma\left(\frac{1}{x}\right)$$

with the mean relaxation time $\langle T_2 \rangle$ determined by stretched exponential fitting, the stretch factor x and the gamma function $\Gamma(1/x)$.

2.3.2.4 Instantaneous Diffusion measurements

Here, in analogy to T_2 measurements, the resulting relaxation curves were fitted by a stretched exponential. $\langle T_2 \rangle$ -values for the different settings of the microwave attenuation were transferred to T_2 based on the William-Watts-Relation for each level of microwave attenuation. Since the microwave attenuation is directly correlated to the flip angle β by

$$\beta(a) = \beta(r) \sqrt{10^{\frac{dB(r)}{10} - \frac{dB(a)}{10}}}$$

with $\beta(a)$ as the actual flip angle after changing the microwave attenuation, $\beta(r)$ as the optimized reference flip angle (was set as near as possible to 180°), and $dB(a)$ and $dB(r)$ as the correlated values of microwave attenuation. After that $1/T_{ID}$ is plotted against $\sin^2(\beta/2)$. If there is a correlation between the concentration of spins (C), the phase recovery time (T_2) and the mw pulse flip angle of a pulse EPR experiment (β) in the form

$$\frac{1}{T_2} = \frac{C\pi\mu_0 g_1 g_2 \beta_e^2}{\hbar 9\sqrt{3}} \sin^2\left(\frac{\beta}{2}\right),$$

a linear correlation of $1/T_{ID}$ and $\sin^2(\beta/2)$ should be revealed. Linear fitting delivers values for the slope, which can be directly converted into a local concentration of spins.⁴⁶

2.2.2.5 3-pulse ESEEM measurements

ESEEM data were analyzed with a home written MATLAB program provided by Dr. Dariush Hinderberger. After optimization of the phase a stretched exponential was fitted to the decay data for a user selected region of the time spectrum. After dividing by the background the residual modulation was Fourier transformed into the frequency domain.

2.2.2.6 HYSCORE measurements

First, the real part of the time-domain, quadrature-detected signal was optimized. Then a 3rd-order polynomial fit was used in order to determine the experimental background. Background-corrected spectra were then zero-filled and apodized with a Hamming window function. After Fourier transformation the absolute values were computed and the 2-dimensional spectra were symmetrized about the diagonal. Simulation of HYSCORE spectra was performed with a MATLAB-based program that utilizes “ZOMA“, a software that was developed at the ETH Zurich.⁵⁵

2.2.2.7 DEER measurements

DEER measurements were analyzed using the “DeerAnalysis2008” program written by Gunnar Jeschke.⁵⁶⁻⁵⁸ The experimental data was loaded in the program followed by automatic or manual optimization of the signal phase (Fig. 2.4). Then the starting point and the end point (cut off time) of the data analysis were defined manually. After that the starting point for the 3D-background was defined. This value was fixed at position at the beginning of the last quarter of the analyzed part of the decay spectrum. Then the spectrum was divided by the background function and the residual modulation was Fourier transformed and symmetrized about the y-axis in order to obtain the characteristic dipolar spectrum. Simulation of the dipolar data finally enabled to extract the characteristic distance information. Therefore, input parameters like the assumed distances and their relative fraction in the dipolar spectra were optimized.

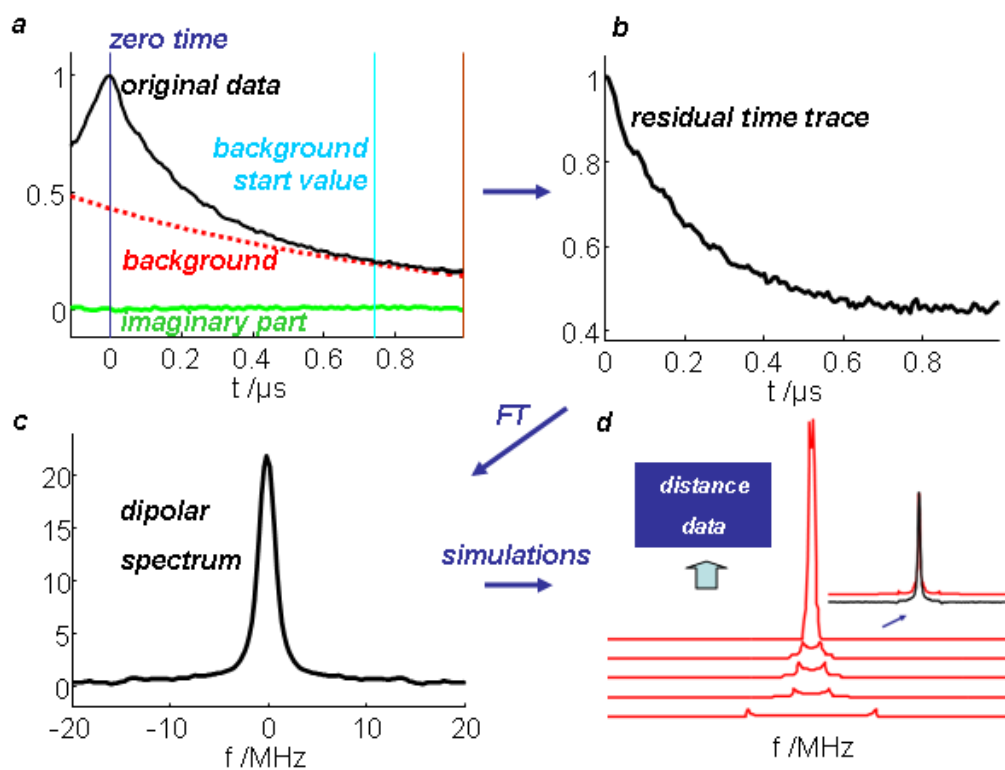


Fig. 2.4. DEER data analysis. **a**: Original data. **b**: Background corrected data **c**: Fourier transformed data in the frequency domain. **d**: Simulation of dipolar data based on the input of distances. The final distance information is obtained by optimization of the input parameters (distances, relative fraction of the different distances within the dipolar data).

3. Results

3.1 Uptake of Cu^{2+} by non-spin-labeled MBP in solution

The uptake of Cu^{2+} by non-spin-labeled MBP was studied based on different sample conditions. First, MBP/ Cu^{2+} samples were prepared in TRIS-buffer (pH 7.4) with a molar MBP/ Cu^{2+} ratio of 1:3. Additional samples were prepared in phosphate buffer (pH 7.4) with molar MBP/ Cu^{2+} ratios of 2:1, 1:1, 1:2, 1:3, 1:4, and 1:5. Finally, also reference Cu^{2+} samples with only buffer, without MBP, were prepared. Standard EPR measurements were performed for all the samples according to the measurement conditions mentioned above (for details see Chapter 3, Materials and Methods).

3.1.1 CW EPR measurements

CW EPR measurements based on Cu^{2+} together with non-spin-labeled MBP were performed at 77 K. The spectra of MBP and Cu^{2+} in TRIS buffer and phosphate buffer with a molar MBP/ Cu^{2+} ratio of 1:3 (Fig. 3.1) both reveal the characteristic hyperfine splitting pattern of copper CW EPR spectra.

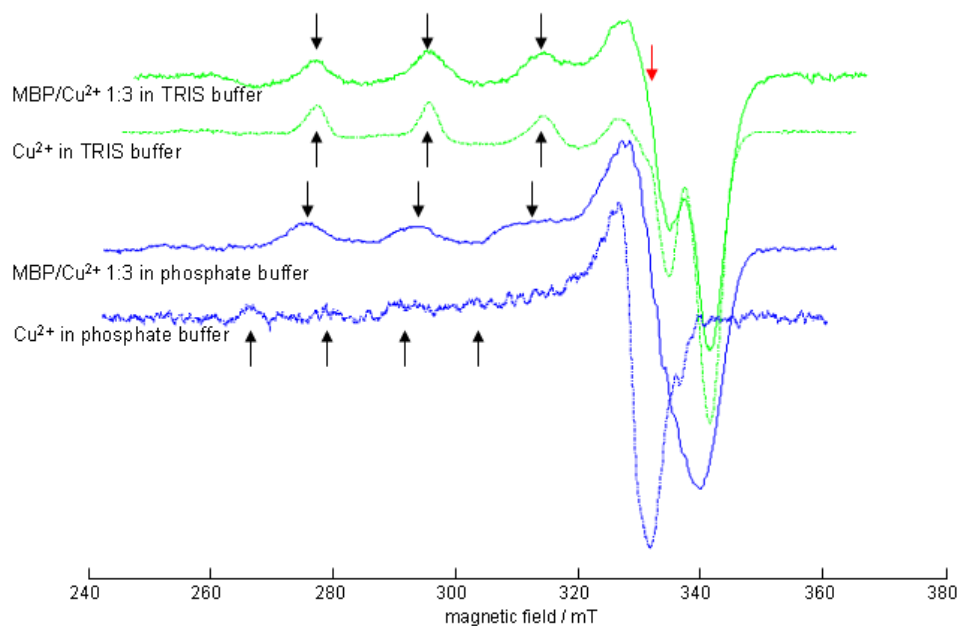


Fig. 3.1. CW EPR spectra of non-spin-labeled MBP and Cu^{2+} (ratio 1:3) in TRIS buffer (green) and phosphate buffer (blue) at 77 K (integral normalized). Measurements with Cu^{2+} in TRIS or phosphate buffer without MBP are shown in dashed lines.

Results

At first sight, only three of the four characteristic peaks of copper A_{\parallel} splitting are observable in the low field region of the spectra (indicated by black arrows). The fourth one, at a higher magnetic field, overlaps with the well pronounced g_{\perp} fraction within the EPR spectra and is only visible in the samples prepared in TRIS buffer (red arrow). In the spectrum of MBP and Cu^{2+} in TRIS buffer, an additional shoulder emerges in the g_{\perp} -region. In general, there is a high similarity between the spectrum of MBP/ Cu^{2+} (ratio 1:3) in TRIS and the TRIS reference spectrum with only slight shifts of the dominant peak positions and the same overall signal width. Comparing the spectrum of MBP and Cu^{2+} in phosphate buffer with the reference spectrum without MBP, clear shifts of the peak positions are observable as well as a significant change in the overall signal width. In case of the reference spectrum the peaks in the g_{\perp} region as well as the peaks in the g_{\parallel} region are shifted towards lower magnetic fields. Additional smaller splittings, which are characteristic for nitrogen hyperfine coupling, are detectable in the spectrum of MBP and Cu^{2+} in phosphate buffer. They split the g_{\perp} region of the spectrum at about 320 – 335 mT and were not detectable in the sample with TRIS buffer. For a better resolution of these specific splittings additional detailed scans were performed for the magnetic field region of 315 – 345 mT for both buffer conditions (Fig. 3.2). These splittings also seem to occur in the spectrum of MBP and Cu^{2+} in TRIS buffer, but with much lower intensity. In the spectra of the reference samples, no comparable additional splittings were observed (data not shown).

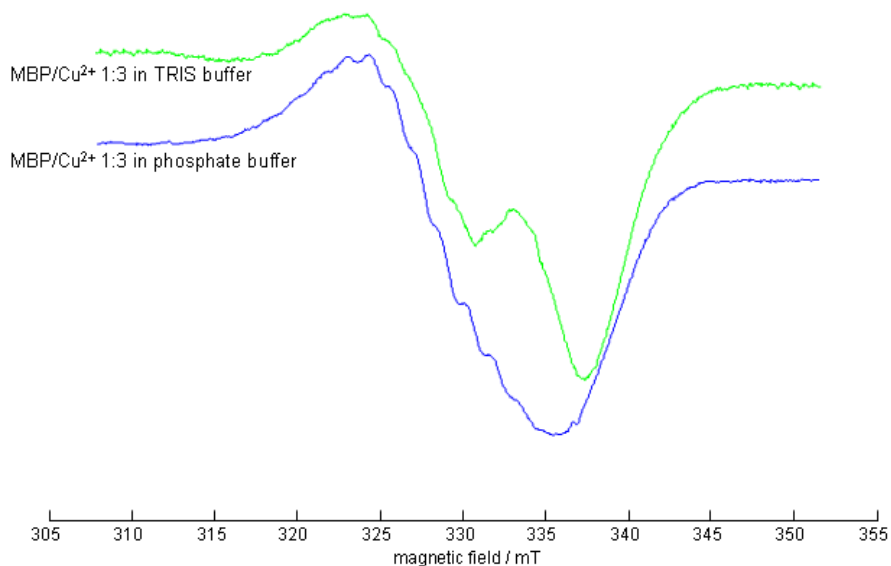


Fig. 3.2. g_{\perp} region of the CW EPR spectra of non-spin-labeled MBP and Cu^{2+} (1:3) in TRIS buffer (green) and phosphate buffer (blue) at 77 K.

Results

Regarding the molar ratios of MBP/Cu²⁺, several characteristic alterations of the spectral features are observable (Fig. 3.3).

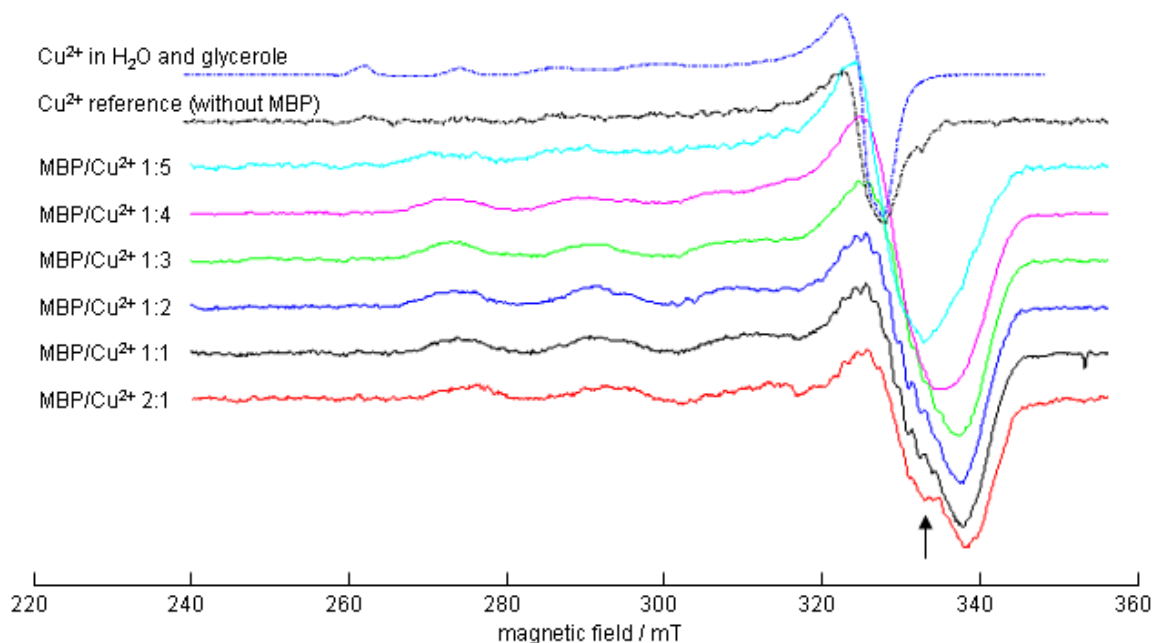


Fig. 3.3. CW EPR spectra of Cu²⁺ and non-spin-labeled MBP in phosphate buffer with different molar ratios of MBP and Cu²⁺ at 77 K (integral normalized). Reference measurements with Cu²⁺ in phosphate buffer without MBP and Cu²⁺ in water and glycerole are shown in dashed lines on top of the plot, scaled by a factor of 0.2.

A gradual change in the shape of the $g_{\parallel}/A_{\parallel}$ components of the copper spectrum is observed. In this context, for some samples additional peaks appear in the low-field region of the copper spectrum. These findings are accompanied by changes of the spectral shape of the g_{\perp}/A_{\perp} components of the spectrum. Here, characteristic shoulder-like structures emerge (indicated by the black arrow), which are best observable in the spectra of the 2:1- and 1:1-samples and disappear towards higher contents of Cu²⁺ within the sample. Additionally, the major peaks in the g_{\perp} region of the spectrum shift towards a lower magnetic field for samples with a higher content of Cu²⁺. Moreover, a change in the shape of the smaller couplings in the region of about 320 – 335 mT becomes observable. With an increasing copper content in the sample the couplings become better observable reaching their maximum intensity in the 1:1 and 1:2 sample. Higher contents of copper, again, lead to decreasing intensities of the couplings, until finally, in the 1:4 sample, the couplings are not detectable anymore. Simulations of these CW EPR spectra were performed and shown together with the respective spectra (Fig. 3.4).

Results

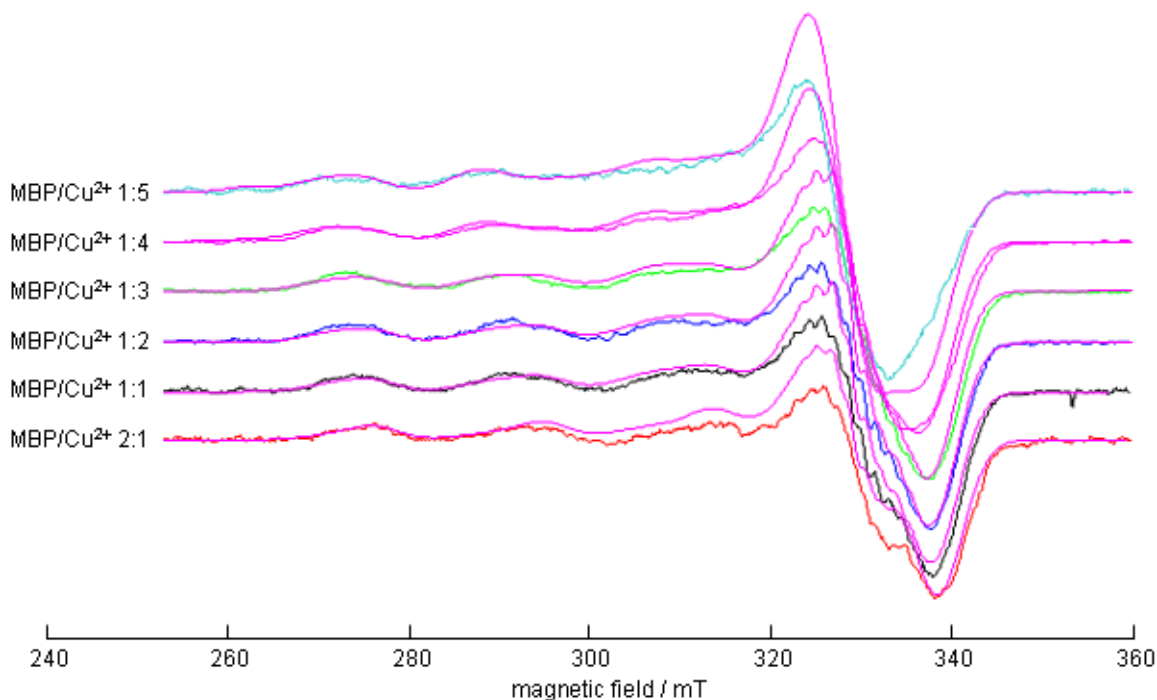


Fig. 3.4. CW EPR spectra of Cu^{2+} and non-spin-labeled MBP in phosphate buffer with different molar ratios of MBP and Cu^{2+} at 77 K (integral normalized) and simulated spectra.

Best agreement of experimental and simulated data was achieved with the assumption that the resulting, simulated spectrum is composed of at least three different copper species. The simulation model applied here assumes two or three copper species, which partly show ^{14}N -hyperfine coupling and seem to be coordinated to MBP (species I-III). In addition, one species of free copper (species IV) is introduced, which can be simulated very well for the reference samples of Cu^{2+} in phosphate buffer and Cu^{2+} in water and glycerole (data not shown). EPR parameters like g values and $^{63}\text{Cu}^{2+}$ and ^{14}N hyperfine couplings are summarized in Table 3.1.

Table 3.1. g - and hyperfine coupling values of species I to IV used for simulation.

	$g_{\perp}(\text{Cu})$	$g_{\parallel}(\text{Cu})$	$A_{\perp}(\text{Cu})$ /MHz	$A_{\parallel}(\text{Cu})$ /MHz	$a_{\text{iso}}(\text{N})$ /MHz	number of coupled N
<i>species I</i>	2.041	2.211	27	575	50	4
<i>species II</i>	2.043	2.253	27	550	50	4
<i>species III</i>	2.045	2.2635	27	560	50	4
<i>species IV</i>	2.053	2.39	13	410	50	4

Results

For all species axial symmetry of the g tensor was assumed. For the 2:1 sample the simulation model proposes a relatively high proportion of bound species I (~60%, Fig. 3.5) which features a relatively small g_{\parallel} value of about 2.211 and a Cu^{2+} hyperfine coupling of 575 MHz, and a lower percentage of species II (~40%) with a g_{\parallel} value of about 2.253 and a hyperfine coupling of 550 MHz. With higher copper contents (sample 1:1 and 1:2) the fraction of species II increases up to ~70% while the fraction of species I decreases (~30%). With respect to the simulations for the samples 1:3, 1:4, and 1:5 the fraction of free copper steadily increases up to 25% and leads to shifts of all spectral features towards lower magnetic field. An additional third species (bound species III) was introduced with a g_{\parallel} value of about 2.264 and hyperfine coupling of 560 MHz, which accounts for a fraction of about 50% in simulations of the 1:4 and 1:5 spectra (fraction of species I: 18%).

To simulate the characteristic couplings in the magnetic field region from 320 – 335 mT additional couplings to four nitrogen atoms have been introduced (with isotropic coupling constants of about 50 MHz) for bound species II.

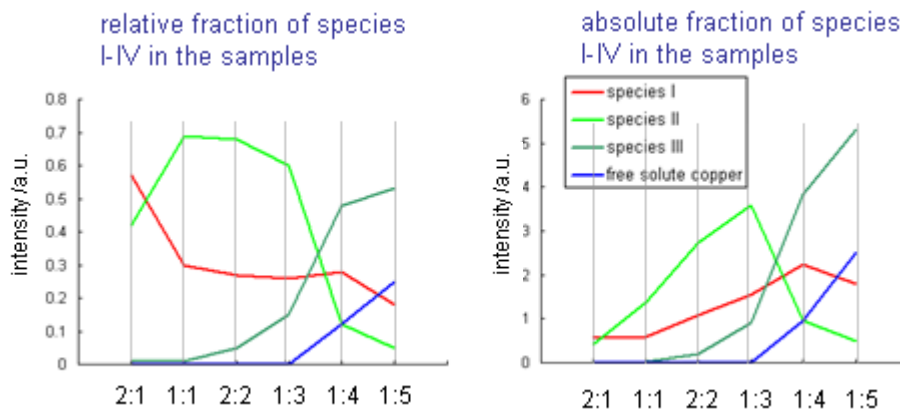


Fig. 3.5. Fraction of simulated species for each molar ratio of MBP and Cu^{2+} giving optimized simulations of the original data.

3.1.2 ESE-detected EPR measurements

ESE-detected EPR measurements (ESE EPR) were carried out at 8 K for samples of non-spin-labeled MBP together with Cu^{2+} in TRIS, or phosphate buffer. Similar to the CW EPR measurements, the ESE EPR spectra of MBP and Cu^{2+} (1:3) in TRIS buffer and the reference without MBP share most of the characteristic spectral features (Fig. 3.6).

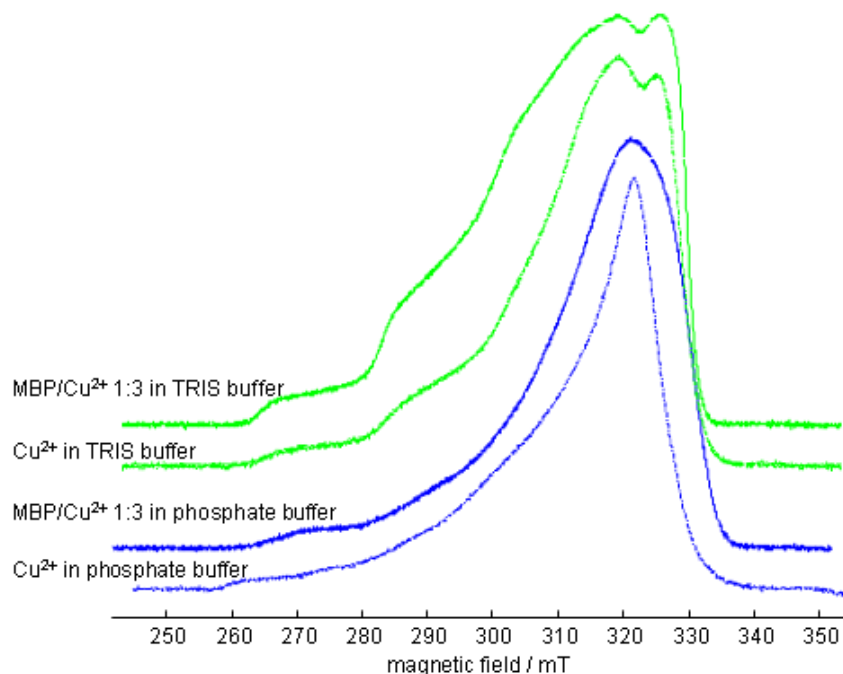


Fig. 3.6. ESE-detected EPR spectra of non-spin-labeled MBP and Cu^{2+} (1:3) in TRIS buffer (green) and phosphate buffer (blue) at 77 K (normalized to maximum). Spectra of Cu^{2+} in TRIS or phosphate buffer are shown as dashed lines.

The only small difference is found in the line width of both spectra (this fact was better resolved in the CW EPR measurements presented before). In contrast to these findings, the spectrum of MBP and Cu^{2+} (1:3) in phosphate buffer and the respective reference spectrum without MBP show significant differences. There is a significant change in the overall width of the signal, which is accompanied by shifts of the major spectral features towards a higher magnetic field in the presence of MBP.

Results

Upon variation of the molar ratios of MBP and Cu^{2+} in phosphate buffer, the achieved data are comparable to the results stemming from CW EPR measurements. Here, again there is a gradual change in the shape of the A_{\parallel} components towards broader peak structures and the occurrence of additional peaks with higher contents of Cu^{2+} within the samples (Fig. 3.7). Additionally, some changes are visualized in the g_{\perp}/A_{\perp} region of the spectra with a tendency towards a lower magnetic field and narrowed spectral structures with increased copper concentration. The couplings in the magnetic field region of about 320 – 335 mT of the respective CW EPR spectra were not observed here due to the limited resolution of the experiment. As for the ESE-detected measurements no simulations were performed due to the poor spectral resolution when compared with CW EPR measurements, which were simulated.

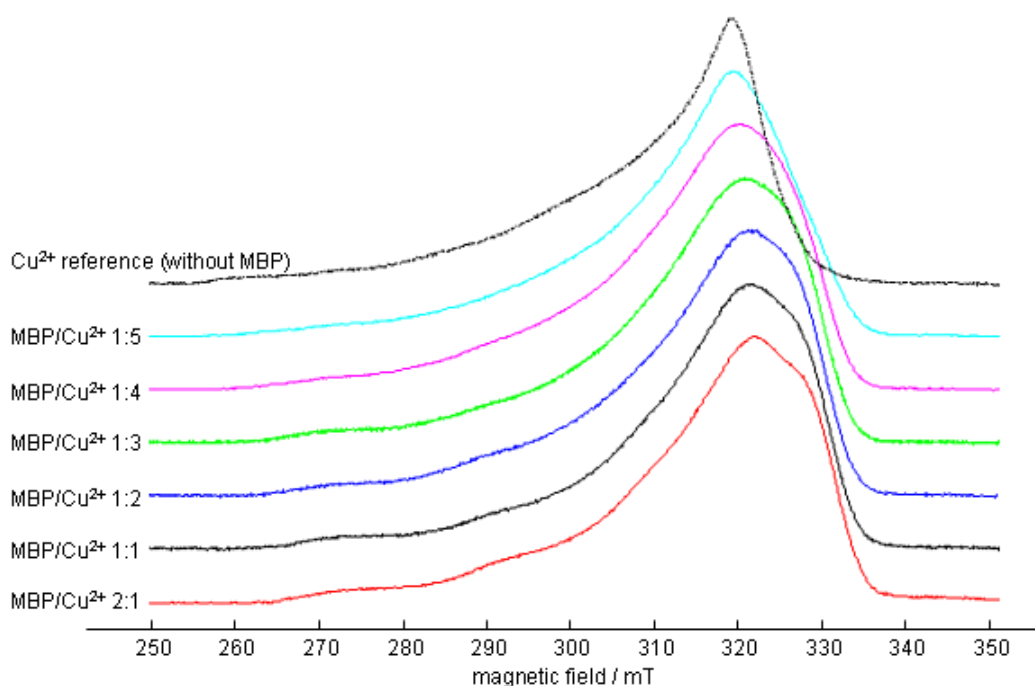


Fig. 3.7. ESE-detected EPR spectra of Cu^{2+} and non-spin-labeled MBP in phosphate buffer with different molar ratios of MBP and Cu^{2+} at 8 K (normalized to maximum). The reference spectrum of Cu^{2+} in phosphate buffer (without MBP) is shown in dashed lines on top of the plot.

3.1.3 2-Pulse ESEEM measurements

2-Pulse ESEEM experiments were performed to characterize the T_2 relaxation behavior of Cu^{2+} /MBP at 8 K at three different field positions 1, 2, and 3 of the respective ESE-detected EPR spectra (information about the exact location of the field positions is given in Fig. 2.1). While the field position 2 (maximum) lies well within the g_{\perp} regime of the spectrum, both in position 1 and 3 orientations towards the z-axis of the Cu-frame are selected. For summary, the samples

Results

containing MBP and Cu²⁺ with different molar ratios in phosphate buffer covered a set of T_2 relaxation times in the range of 2.9 – 4.3 μs (Table 3.2).

Table 3.2. T_2 relaxation time determined by 2-Pulse ESEEM for the spectral positions 1, 2 and 3 (Fig. 2.1).

<i>sample</i>	<i>2:1</i>	<i>1:1</i>	<i>1:2</i>	<i>1:3</i>	<i>1:4</i>	<i>1:5</i>	<i>reference</i>
$T_2(1) / \mu\text{s}$	3.36	3.14	2.99	2.86	2.92	3.3	4.01
$T_2(2) / \mu\text{s}$	3.59	3.3	3.2	3.09	3.05	3.71	4.35
$T_2(3) / \mu\text{s}$	3.24	3.19	3.07	2.92	3.01	3.53	3.94

When comparing the data at the same spectral detection positions, a clear tendency with variation of the MBP/Cu²⁺ ratio, is displayed. In general, long T_2 values are observed for the sample with the lowest copper content (MBP/Cu²⁺ 2:1). With increasing copper content, T_2 values decrease steadily up to a MBP/Cu²⁺ ratio of 1:3 or 1:4. Further increase of the Cu²⁺ concentration finally results in increasing T_2 values, again. For the 2-Pulse ESEEM experiments at position 1, the T_2 values of the 2:1 and 1:5 sample are almost on an equal level (3.36 μs and 3.3 μs), while for position 2 and 3, the values obtained for the 1:5 sample are slightly larger than those of the 2:1 sample. T_2 values in the reference sample in general tend towards values larger than ~4 μs , and are significantly larger than all T_2 values in samples with MBP.

The same tendency is observed for the stretch factors describing the polynomial order of the exponential decay detected by the 2-Pulse ESEEM experiment (data not shown).

3.1.4 HYSCORE measurements

HYSCORE measurements were performed at 8 K at the three different field positions indicated in Fig. 2.2. These experiments included samples with MBP and Cu²⁺ with different molar ratios in phosphate buffer as well as MBP and Cu²⁺ in TRIS buffer (MBP/Cu²⁺ 1:3) and the corresponding reference samples without MBP. Further, different τ -values (136 and 167 ns) have been tested in order to achieve optimum HYSCORE spectra.

The comparison between HYSCORE spectra performed with MBP and Cu²⁺ with the two different buffer conditions and a molar MBP/Cu²⁺ ratio of 1:3 reveal several characteristic spectral features (Fig. 3.8). Only the (-,+) (left hand side) and the (+,+) quadrants (right hand side) of the frequency domains have been plotted here. First, in the low frequency region cross peaks are observed at (1.6, 4.0) and (4.0, 1.6) MHz (indicated by red arrows). These do not occur in the reference spectra without MBP and are characteristic for double quantum ($|\Delta m_I|=2$) transitions $\nu_\alpha^{dq}, \nu_\beta^{dq}$ of distal imidazole ¹⁴N₆ nuclei from coordinated histidine side chains.⁵⁹⁻⁶⁰ Additional spectral features

Results

appear between 2 and 4.5 MHz at field positions 1 and 2, which are characteristic for nitrogen coupling with a high proportion of quadrupole coupling and will be treated in detail below. In addition to the well pronounced peaks of proton coupling at (14, 14) MHz characteristic ridge-like proton cross peaks appear at about (8, 20) and (20, 8) MHz in TRIS buffer (green arrows), with highest intensities observed at field position 1 or the reference sample (position 2). In position 3, and for MBP and Cu^{2+} in TRIS buffer, the characteristic anti diagonal ridges shift towards the diagonal with frequencies of (10, 15) and (15, 10) MHz. In phosphate buffer additional proton couplings were only observed at the z-direction (black arrows) and the reference measurement without MBP (green circles). In the reference sample also a pair of cross peaks centered at the ^{31}P Larmor frequency (5.498 MHz at 3187 G) with a splitting of 9.8 MHz (indicated by red circles) is evidenced. Measurements detected with $\tau = 136$ ns reveal well pronounced ridge-like proton couplings for the samples with MBP and Cu^{2+} in phosphate buffer, too (data not shown).

An additional series of HYSORE measurements of samples with varying MBP/ Cu^{2+} ratios was performed at 8 K at the three different field positions 1, 2, and 3 of the ESE-detected spectra ($\tau = 176$ ns). Focusing on the couplings, which are assumed to originate from weak couplings of coordinated Cu^{2+} to remote nitrogen atoms within the protein, only the corresponding (+,+) quadrants of the frequency domain of the original HYSORE spectra are plotted (Fig. 3.9), since there were no significant spectral changes in the (-,+) quadrant.

Again, cross peaks are observed at (1.6, 4.0) and (4.0, 1.6) MHz (indicated by red arrows) which are characteristic for double quantum ($|\Delta m| = 2$) transitions $\nu_{\alpha}^{dq}, \nu_{\beta}^{dq}$ of distal imidazole $^{14}\text{N}_6$ nuclei from coordinated His side chains. These couplings seem to be best resolved for MBP/ Cu^{2+} ratios of 1:2 and 1:3 at the g_{\perp} orientations (Fig 3.9, see detailed view on the top right corner). In general, they share almost equal intensities for all molar ratios of MBP and Cu^{2+} up to 1:4. For a ratio of MBP/ Cu^{2+} of 1:5 the cross peak intensity decreases. The same tendency is observed for the additional cross peaks at (3.1, 4.2) and (4.2, 3.1) MHz, which most obviously stem from couplings with surrounding non-coordinating backbone amides with $a_{\text{iso}}(^{14}\text{N}_{\text{am}}) \approx 1$ MHz.⁵⁹⁻⁶⁰ An additional diagonal peak seems to be located at the ^{23}Na Larmor frequency at ~ 3.6 MHz. At MBP/ Cu^{2+} ratios of 1:5 proton cross peaks comparable to those discovered in the Cu^{2+} reference sample in phosphate buffer (Fig. 3.8, **h**) seem to occur (data not shown).

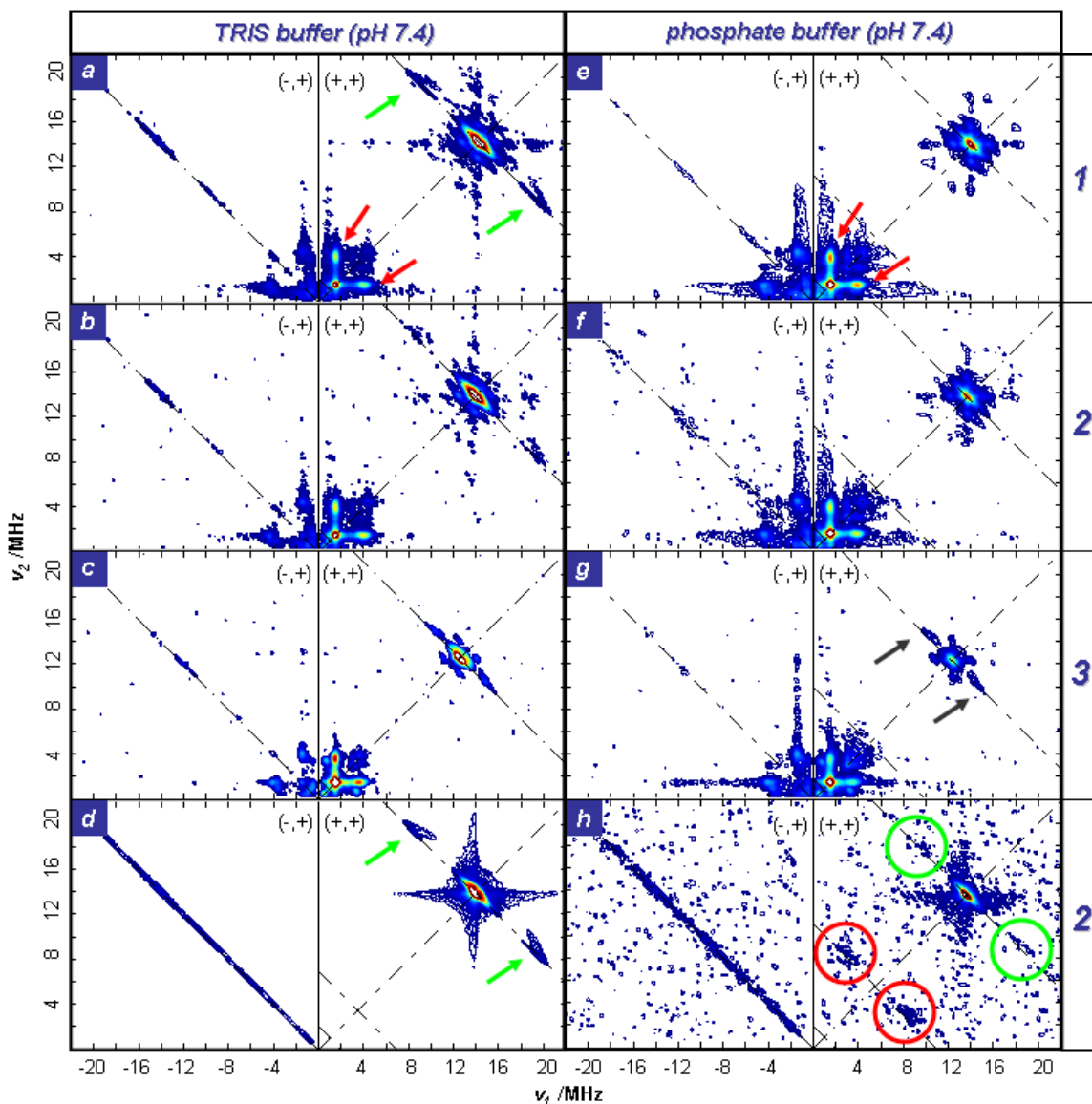
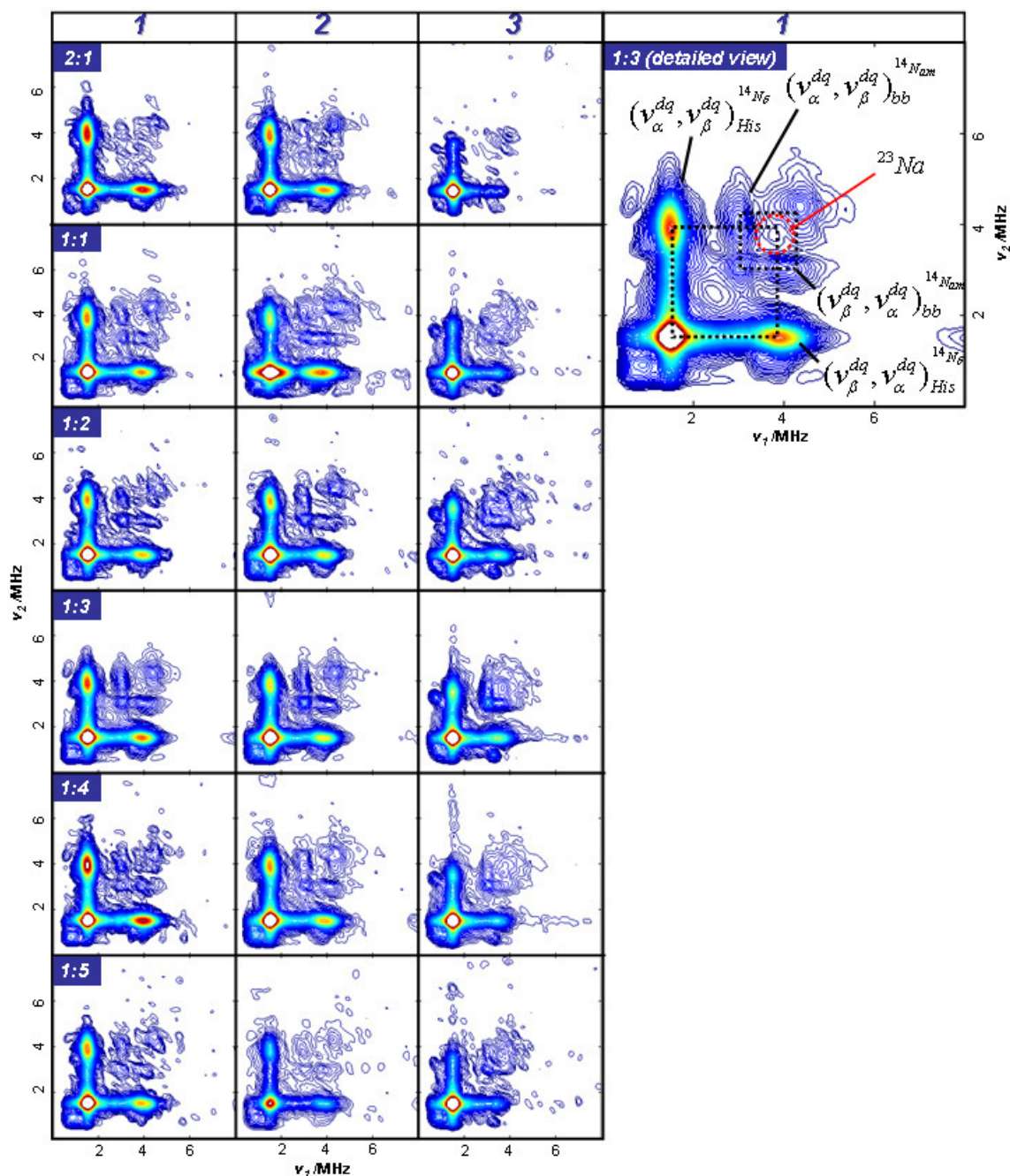


Fig. 3.8. X-band HSCORE spectra of MBP and Cu^{2+} in TRIS buffer and phosphate buffer at 8 K ($\tau = 176$ ns, pH 7.4) for the different field positions 1, 2, and 3 (Fig. 2.2). Only the $(-,+)$ and the $(+,+)$ quadrant of the frequency domains are plotted here. **a, b, c:** MBP and Cu^{2+} 1:3 in TRIS buffer. **d:** reference sample without MBP in TRIS buffer. **e, f, g:** MBP and Cu^{2+} 1:3 in phosphate buffer. **h:** reference sample without MBP in TRIS buffer. Cross peaks at (1.6, 4.0) and (4.0, 1.6) MHz (red arrows) are characteristic of $^{14}\text{N}_\delta$ His side-chain coordination. Additional proton couplings are observable at 14 MHz with well resolved ridge-like structures in the measurements in TRIS buffer (green arrows). In the phosphate buffer reference measurement additional cross peaks at the ^{31}P Larmor frequency (5.498 MHz at 318.7 mT) with a splitting of 9.8 MHz (indicated by red circles) and additional proton ridges at (10, 19) and (19, 10) MHz (green circles) are observed. For the samples with MBP content in phosphate buffer significant proton ridges are only detected in z-orientation (black arrows).

Results



4.0) and (4.0, 1.6) MHz are characteristic for $^{14}N_6$ His side-chain coordination and share equal intensities for all molar ratios of MBP and Cu^{2+} up to 1:4. For a MBP/ Cu^{2+} ratio of 1:5 the cross peak intensity decreases. The cross peaks are most pronounced at field positions 1 and 2. The same tendency is observed for additional cross peaks at (3.1, 4.2) and (4.2, 3.1) MHz, which most obviously stem from couplings with nearby non-coordinating backbone amide with $a_{iso}(^{14}N_{am}) \approx 1$ MHz and $4K \approx 3$ MHz. An additional diagonal peak appears at the ^{23}Na Larmor frequency at ~ 3.6 MHz.

3.1.5 DEER

3.1.5.1 Orientation dependence of Cu^{2+} -DEER measurements

With regard to the central aim of collecting structural information about MBP and its possible aggregation by DEER distance measurements, first, it was checked whether there is an orientation sensitivity of the resulting DEER data. This is necessary due to the very broad and orientation sensitive Cu^{2+} EPR spectrum. Measurements were performed at 8 K at six different field positions (covering large parts of the g_{\perp} and g_{\parallel} regions of the copper spectrum) for a MBP/ Cu^{2+} ratio of 1:1 in phosphate buffer. The frequency difference $\Delta\nu$ between pump pulse and observer pulses was fixed to 70 MHz (~ 2.5 mT) for all measurements. The residual DEER time traces after 3D background correction reveal a slow decay for data in the g_{\parallel} region (Fig. 3.10). Application of DEER in magnetic fields in the g_{\perp} region leads to a faster decay of the time trace within the first 400 ns compared to the DEER traces at low and high magnetic field (orientational selection of g_{\parallel}). In the DEER traces around g_{\perp} , also the highest modulation depth is reached, which is again decreased significantly with a higher selection of g_{\parallel} .

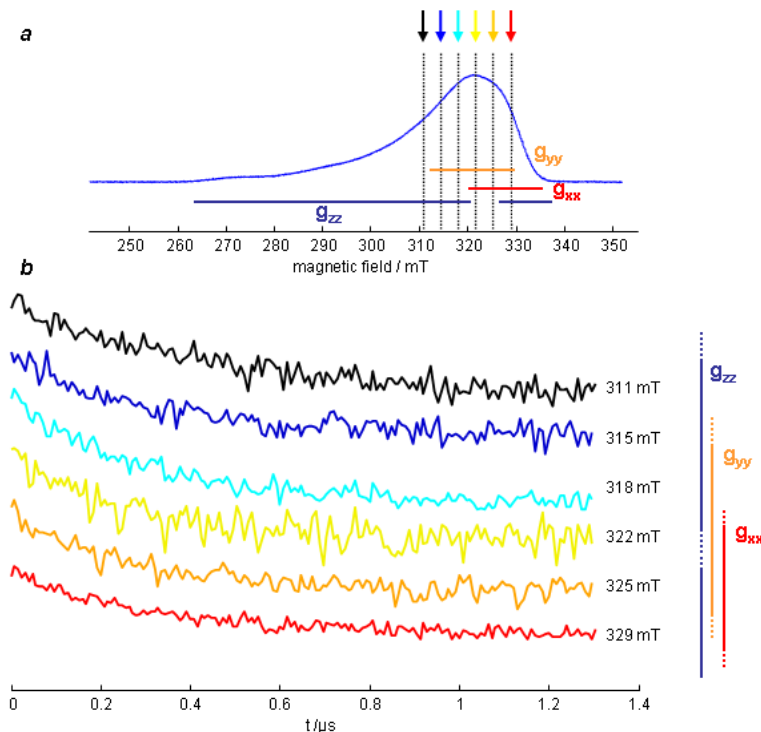


Fig. 3.10. **a:** Detection positions for DEER measurements within the g_{\parallel} and g_{\perp} regions of the ESE-detected EPR spectrum. **b:** Residual DEER time traces after 3D background correction with an MBP/ Cu^{2+} ratio of 1:1 in phosphate buffer at different magnetic field positions. $\Delta\nu$ between pump pulse and observer pulse was fixed to 70 MHz (~ 2.5 mT) for all measurements. In the low field region of the ESE-detected EPR spectrum the decay of the DEER time trace decreases slowly but with a relatively high modulation depth. With increasing magnetic field, the time traces decrease faster in the beginning (0 - 0.4 μs) and reach a maximum modulation depth at 318 mT. Measurements at higher magnetic field positions revealed steadily decreasing modulation depths.

Results

In the following, data analysis based on dipolar data (*i.e.* dipolar spectra obtained from background-corrected time traces after Fourier transformation) will only focus on the fraction of frequencies within a region of about -10 to -0.5 and 0.5 to 10 MHz of the symmetric spectrum. The central peak (-0.5 to 0.5 MHz) will not be interpreted further, since discrimination of individual dipolar couplings of low frequency from the experimental background is practically impossible for the acquired data.

In general, the respective dipolar spectra reveal the tendencies expected from the DEER time traces (Fig. 3.11). The slow decay in the time trace for the 311 mT field position accordingly results in only a moderate fraction of frequencies at -10 to -0.5 (0.5 to 10) MHz for the 311 mT field position. Towards 318 mT the Pake pattern gains in intensity for frequencies within -10 to -0.5 (0.5 to 10) MHz, which is correlated to a faster decay of the time trace within the first about 400 ns. With regard to the measurements performed at higher magnetic fields, the intensity of frequencies within these special regions decreases again (lower modulation depths in the time traces).

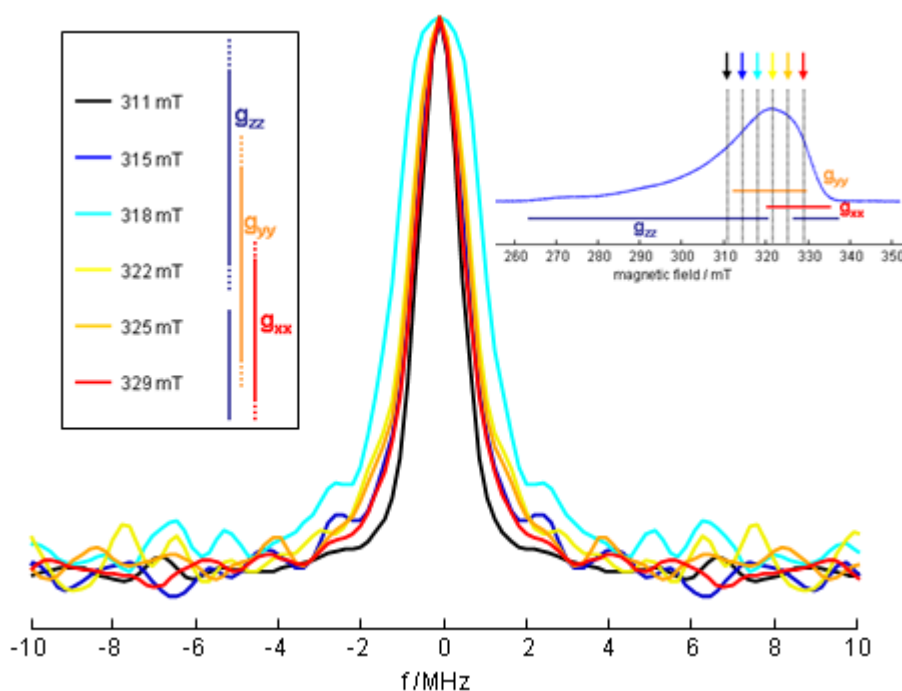


Fig. 3.11. Dipolar spectra of MBP/Cu²⁺ 1:1 in phosphate buffer recorded at different magnetic field positions (see picture in the upper right corner). $\Delta\nu$ between pump pulse and observer pulses was fixed to 70 MHz (~ 2.5 mT) for all measurements. The spectral intensity within about -10 to -0.5 and 0.5 to 10 MHz of the Pake pattern is weak for field positions within the g_{\parallel} (z) region and increases - until maximum intensities are reached for about 318 mT. Higher field positions again lead to decreased signal intensities within these regions.

3.1.5.2 DEER measurements with different MBP/Cu²⁺ ratios

DEER measurements based on different ratios of MBP and Cu²⁺ in phosphate buffer were performed at 8 K. The pump pulse was set to the maximum peak position of the correlated ESE spectra, while the observer pulses were shifted according to the desired orientation selection of the DEER measurement (Fig. 2.3). For the detection of the spins in g_{\parallel} (z_1) region, the observer pulses were shifted 6.2 mT from the maximum spectral peak position towards a lower magnetic field (except for the 1:3 sample: here ΔB was 22.5 mT) or 6.9 mT towards a higher magnetic field g_{\parallel} (z_2). Dipolar coupling to spins in g_{\perp} (xy) direction were detected with a shift of the observer pulses of 2.5 mT towards a lower magnetic field.

The background corrected data were analyzed according to the orientational dependence and for each molar MBP/Cu²⁺ ratio (Fig. 3.12, left column). With regard to the modulation depth the traces only varied to a small extent except for the measurements with higher Cu²⁺-content. Here, the modulation depth seems to be a bit lower for the measurements with spins observed in the z_2 direction (especially for the sample with an MBP/Cu²⁺ ratio of 1:4). In general, modulation depth is small for samples with molar ratios of 2:1, 1:1, and 1:2. Increased copper content then leads to increased modulation depth with maximum modulation depths in the 1:4 sample (~0.75). As for the 1:5 sample, modulation depth decreases again. Also the correlated, baseline corrected dipolar spectra were plotted together for the same measurement conditions (Fig. 3.12, right column). According to the detection orientation ax , z_1 and z_2 , at first glance, the largest deviations occur in the 2:1 and 1:5 samples. Here, experimental noise complicates interpretation of data to a great extent. In general, detailed spectral analysis was possible for the data with MBP/Cu²⁺ ratios of 1:1, 1:2, 1:3, and 1:4. A small intensity increase is observed in the region of about -10 to -0.5 and 0.5 to 10 MHz with increasing copper content. Maximum intensities seem to occur for a MBP/Cu²⁺ ratio of 1:3 (indicated by arrows). For 1:4 and 1:5 no additional intensity increase is observed. With regard to the orientation selectivity, data obtained in the z_2 direction seem to feature highest intensity of the frequencies in the range of -10 to -0.5 and 0.5 to 10 MHz.

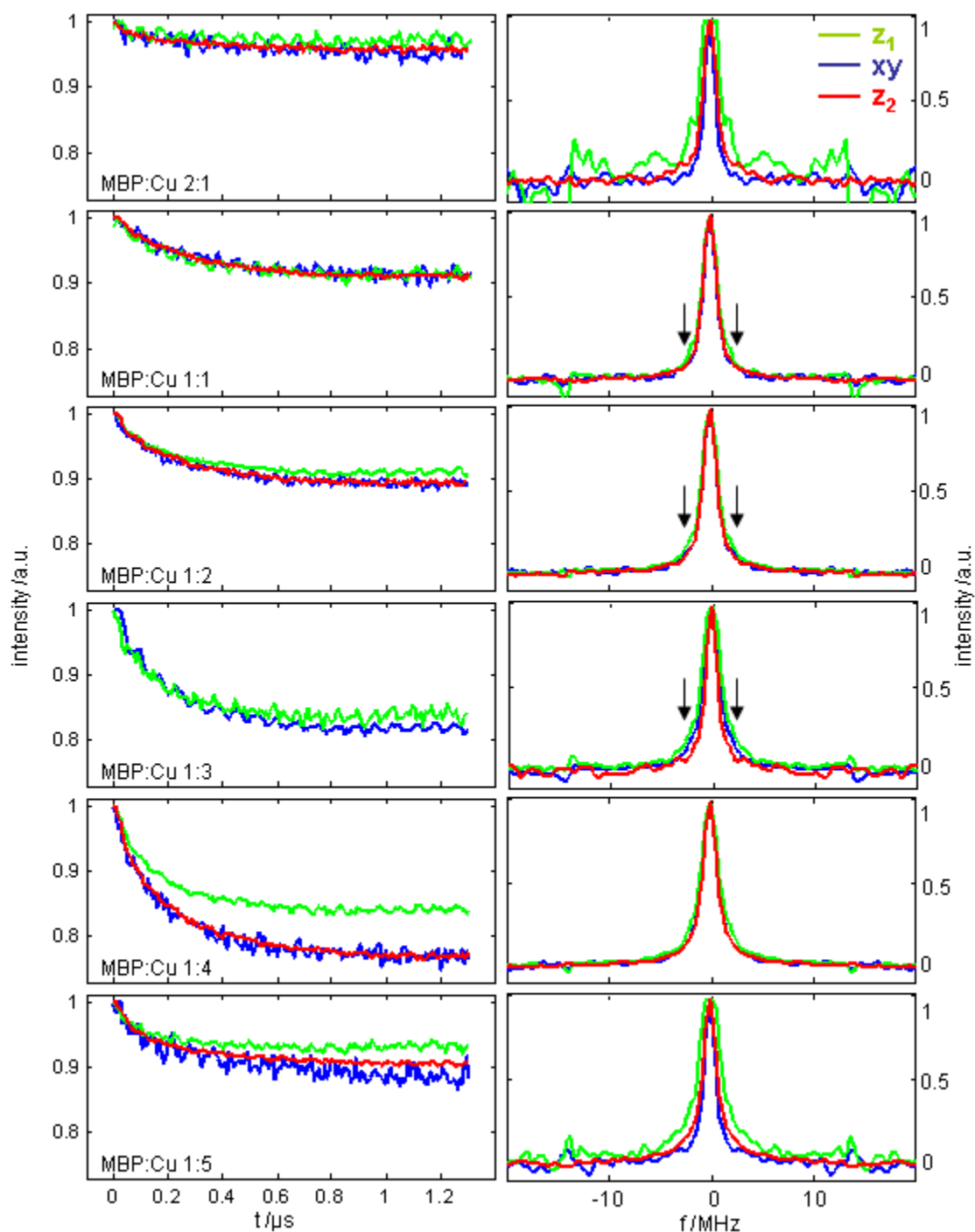


Fig. 3.12. 3D background corrected DEER time traces for X-band DEER measurements at 8 K of Cu^{2+} and MBP with different molar ratios in phosphate buffer (left column) and the according Fourier-transformed dipolar spectra (right column). Modulation depth between data obtained in xy , z_1 , and z_2 time traces only varies to a small extent for ratios of 2:1, 1:1, 1:2, and 1:3. Absolute depth values increase until maximum modulation depths are reached for a ratio 1:4. Higher copper contents again lead to decreased modulation depths. Dipolar spectra share a high level of similarity for observer orientation selectivity (data obtained for ratios of 2:1 and 1:5 are not involved in further spectral analysis due to low SNR). In detailed data analysis there seems to occur a gain in intensity for spectral features in the frequency range of about -10 to -0.5 and 0.5 to -0.5 and 0.5 to 10 MHz from 2:1 to 1:3. Higher copper concentrations do not lead to further spectral changes.

Results

DEER time traces and dipolar spectra were also plotted for each selection of observed spins to better compare effects based on Cu^{2+} concentration (Fig. 3.13). Here, again, highest modulation depths are detected for the 1:4 sample (for xy selectivity, the modulation depth for 1:3 is also on a high level). Higher or lower copper concentrations lead to decreasing modulation depths. With regard to the dipolar spectra detailed spectral analysis supports the findings presented already: With increasing copper concentrations spectral features gain in intensity within a frequency range of about -10 to -0.5 and 0.5 to 10 MHz, with maximum intensities detected for MBP/ Cu^{2+} ratios of 1:4. Further increasing copper content again results in a decreased spectral intensity for frequencies within about -10 to -0.5 and 0.5 to 10 MHz.

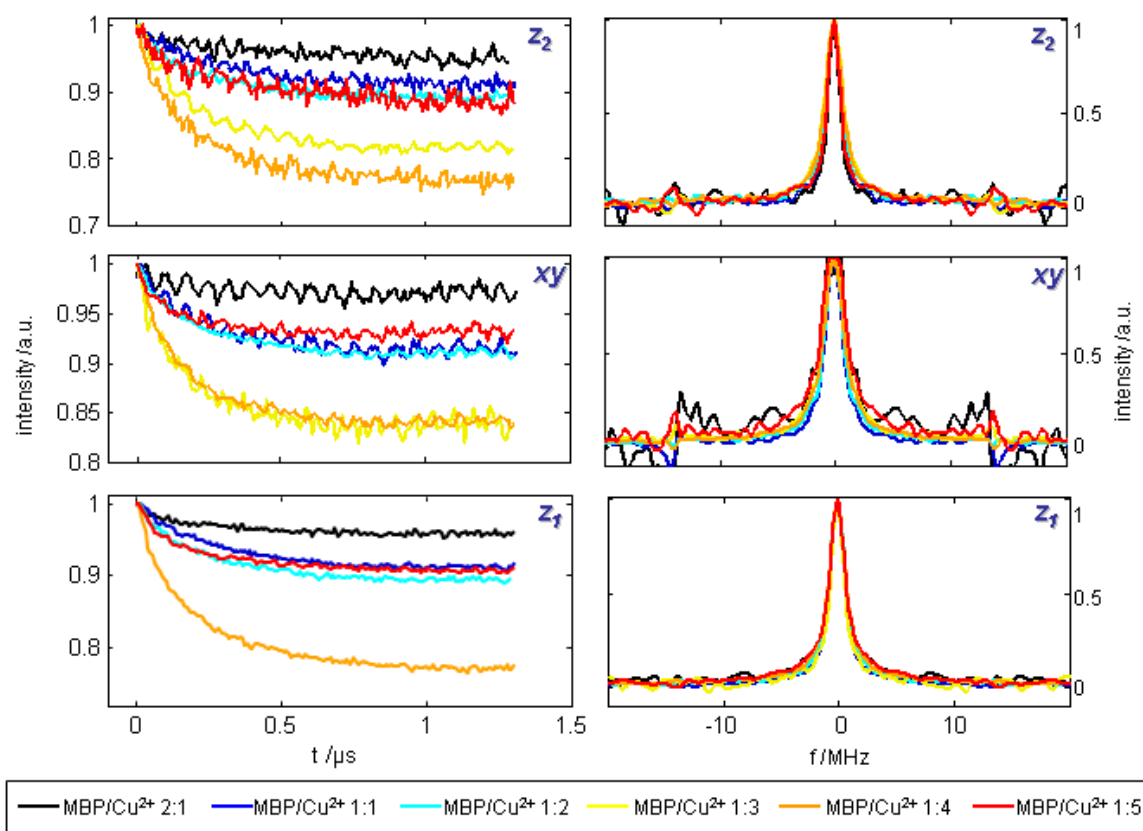


Fig. 3.13. 3D background corrected DEER time traces for X-band DEER measurements at 8 K of Cu^{2+} and MBP with different molar ratios in phosphate buffer grouped by observer orientation selection (left column) and correlated Fourier-transformed dipolar spectra (right column). Modulation depth of the DEER time traces increases for higher copper contents until a maximum modulation depth is reached for 1:4. Higher copper contents again lead to decreased modulation depths. Analysis of the dipolar spectra reveals increasing intensities for frequencies within a range of about -10 to -0.5 and 0.5 to 10 MHz from MBP/ Cu^{2+} ratios of 2:1 to 1:3. Higher copper concentrations again result in decreased intensities. For MBP/ Cu^{2+} ratios of 2:1 and 1:5 the interpretation of data was complicated by a high level of signal noise.

Results

In order to compare the intensities of frequencies in the range of about -10 to -0.5 and 0.5 to 10 MHz (which can be correlated to a medium length distance distribution around 2.8 nm), data sets obtained in xy-direction have been simulated for the molar ratios of 1:1, 1:2, 1:3, and 1:4 (Fig. 3.14).

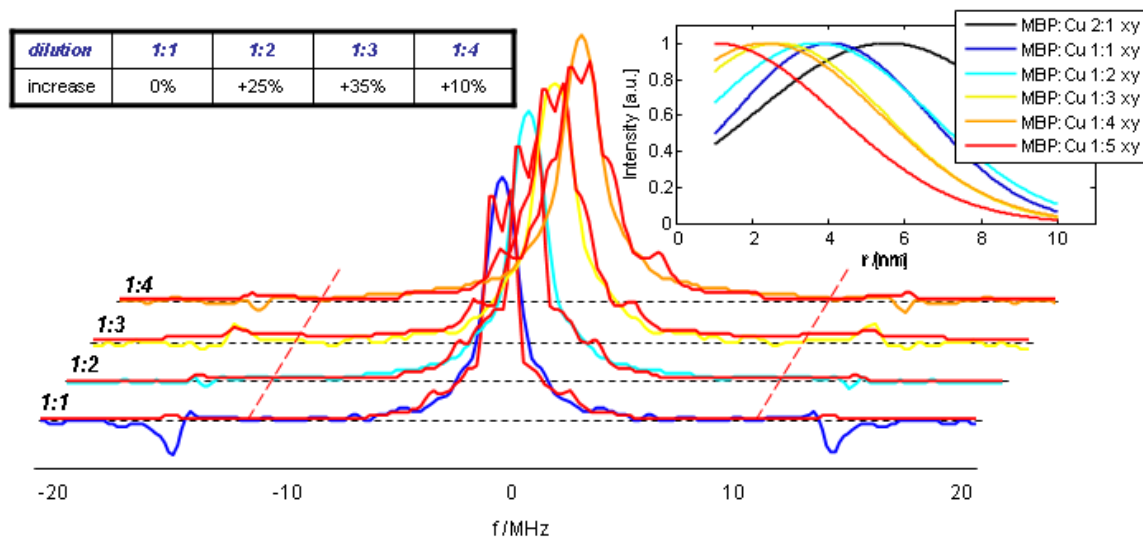


Fig. 3.14. Dipolar spectra and simulations (red) of MBP together with Cu^{2+} for the molar ratios of 1:1, 1:2, 2:3, and 1:4. At a ratio of 1:1 the dipolar spectrum is centered within a frequency range of about -10 to -0.5 and 0.5 to 10 MHz (indicated by red dashed lines) and simulated well with distances in the range of 2.85 (± 0.2) nm (and 4 nm for the central peak). For higher molar ratios up to 1:3 the signal intensity increases for the medium range frequencies corresponding to distances around 2.85 nm. Simulations work very well with the same distance input as for the 1:1-spectrum. The increase in intensity for the spectral fractions which can be correlated to a distribution of distances around 2.85 nm is summarized in the table in the top left corner. For an MBP/ Cu^{2+} ratio of 1:4 a broader distribution or additional smaller distances have to be introduced in order to gain better quality of the simulations. The distance distributions based on single Gaussian fitting are given in the top right corner depicting a general shift towards smaller distances for higher copper content within the samples.

Here, again, the significant part of the dipolar spectrum lies within about -10 to -0.5 and 0.5 to 10 MHz (indicated by red dashed lines). For simulations, distances are selected in the range of 2.85 (± 0.2) nm and 4 nm for the central peak. With increasing molar ratios up to 1:3, signal intensities increase for the medium range distances around 2.85 nm. Thus, simulations for all ratios up to 1:3 work very well with the distance parameters selected for the 1:1 ratio. With a molar ratio of 1:4 the dipolar spectrum seems to feature broadenings in the spectral border region. Here, simulations only lead to good results when a broader distance distribution or additional smaller distances are included. In general, the distance ratio contributing to the broadening of the dipolar spectra increases stepwise with highest increments for the steps from 1:1 to 1:2 and 1:2 to 1:3. This situation is also very well reflected by single Gaussian fittings. Here, the observed distributions shift from larger to smaller distances with increasing copper content.

Results

Also the effect of buffer conditions on the possible interaction of MBP molecules was tested by EPR measurements. A comparison of DEER data obtained with samples of MBP and Cu^{2+} (1:3) in phosphate buffer (50 mM) and TRIS buffer (50 mM) reveals strongly reduced modulation depth of the background corrected time data for the sample preparation in TRIS buffer (Fig. 3.15, **a**).

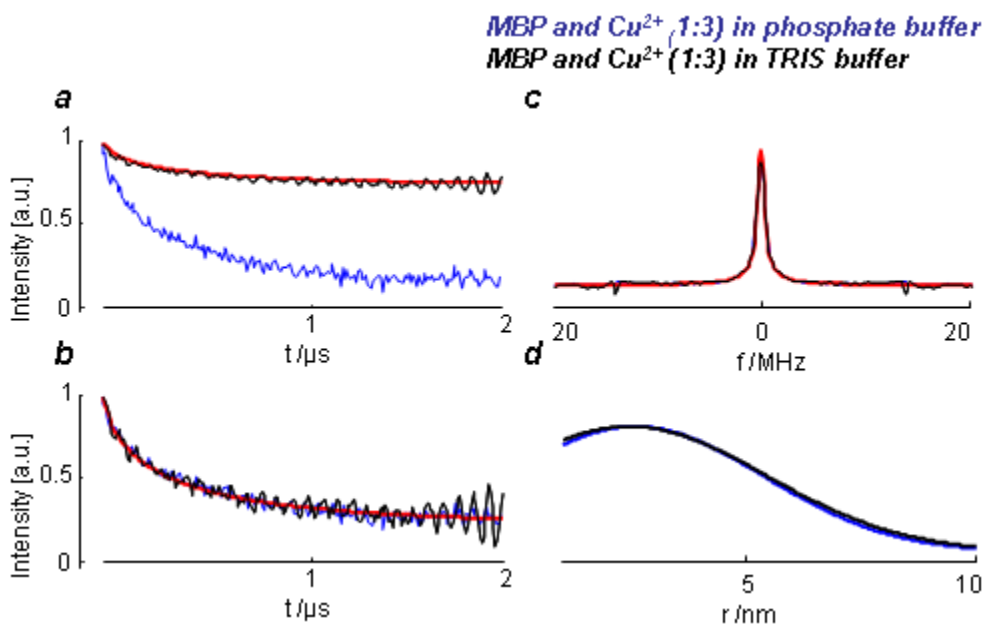


Fig. 3.15. DEER data obtained for measurements with MBP and Cu^{2+} (1:3) in phosphate buffer and TRIS buffer (50 mM) 8 K. **a:** background corrected time data. **b:** background corrected time data with modulation depth scaling. **c:** Fourier transformed dipolar spectra with simulations for Gaussian distance distributions. **d:** Gaussian distance distributions obtained for simulation of the dipolar spectra. Despite the effect of reduced modulation depth for the sample preparation in TRIS buffer no significant differences are observed.

Nevertheless, modulation depth scaling indicates the same overall spectral shape of both time traces (Fig. 3.15, **b**) and also results in almost identical dipolar spectra for both measurements (Fig. 3.15, **c**). Again, both spectra seem to feature a significant fraction of distance contributions around 3 nm, as shown by simulations. As a result, also the distance distributions obtained by single Gaussian fitting of the dipolar data share a very high level of similarity (Fig. 3.15, **d**).

3.2 EPR experiments based on spin-labeled MBP in solution

3.2.1 CW EPR measurements

CW EPR measurements with spin-labeled MBP in solution (3 mM, pure sample) were measured at 77 K (Fig. 3.16). Please note, that all abbreviations of sample names are summarized in Tab. I (page 111, Appendix).

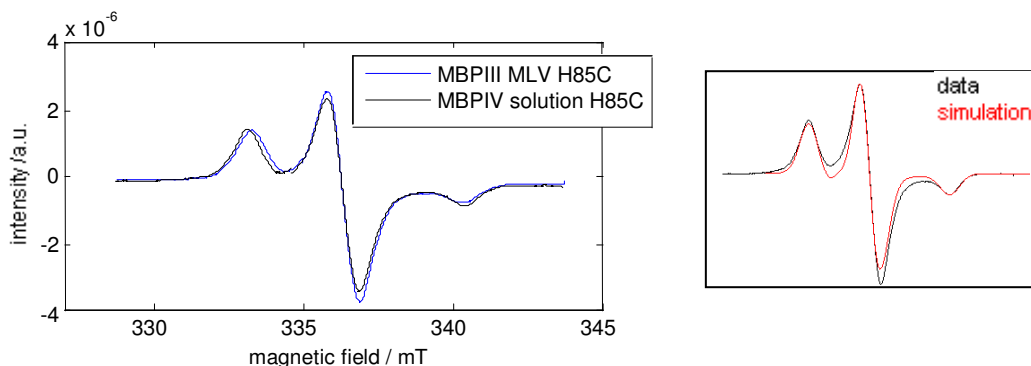


Fig. 3.16. CW EPR spectrum of MBP spin labeled MBP H85C in solution at 77 K and simulation (red spectrum on the right). Additionally, the spectrum of MBP in MLVs (LPR 567:1) was plotted as reference (all data integral normalized). At 77 K, the spectral width of MBP H85C in solution is broader than the one of MBP H85C in MLVs while the spectral shape is roughly the same for both spectra. Simulation parameters for MBP IV H85C in solution: $g_{xx}=2.0092$, $g_{yy}=2.0054$, $g_{zz}=2.0021$; $A_{xx}=13.62$ MHz, $A_{yy}=14.82$ MHz, $A_{zz}=100.89$ MHz; MBP III H85C in MLVs: same parameters, but $A_{zz}=97.89$ MHz.

In general, the spectra of MBP H85C in solution and MBP H85C in MLVs (plotted as reference) share the same spectral features, but additionally, $2A_{zz}$ is increased from 70.8 mT for MBP in MLV H85C to about 72.9 mT for MBP H85C in solution, a difference of about 2.1 mT. Simulation parameters for the two spectra only significantly vary for the hyperfine coupling A_{zz} (97.89 MHz for MBP H85C in MLVs and 100.89 MHz for MBP H85C in solution).

Additional measurements with spin-labeled MBP in solution were performed at room temperature (Fig. 3.17). The spectral shape of MBP in MLVs and MBP in LUVs (as reference spectrum) differs significantly. The spectrum of MBP in MLVs represents a characteristic nitroxide 3-line spectrum while the lines are significantly broadened for MBP H85C in MLVs. Simulations were performed with $g_{xx}=2.0092$, $g_{yy}=2.0054$, $g_{zz}=2.0021$ and $A_{xx}=13.62$ MHz, $A_{yy}=14.82$ MHz, $A_{zz}=108.89$ MHz and a rotation correlation time $\tau=3$ ns (for comparison: MBP II H85C: same g values, $A_{xx}=13.62$ MHz, $A_{yy}=14.82$ MHz, $A_{zz}=97.89$ MHz, $\tau=12.5$ ns).

Results

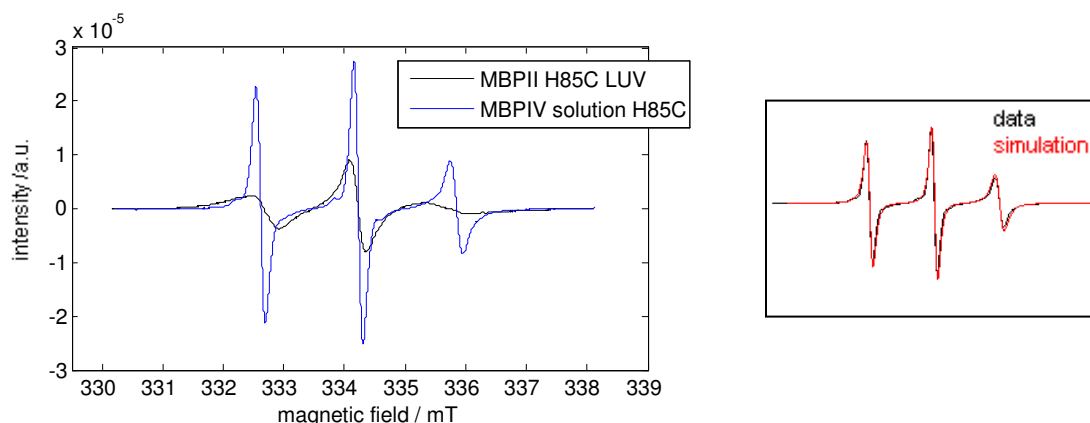


Fig. 3.17. CW EPR spectra of MBP spin labeled MBP H85C in solution at room temperature and simulation (red spectrum, boxed picture on the right). MBP II H85C LUV was plotted as reference (all data integral normalized). At room temperature the spectral shape of MBP IV and MBP II diverge significantly. MBP IV represents a characteristic nitroxide line spectrum while the lines are broadened to a high extent for MBP II H85C in LUVs. Simulation parameters for MBP IV H85C in solution: $g_{xx}=2.0092$, $g_{yy}=2.0054$, $g_{zz}=2.0021$; $A_{xx}=13.62$ MHz, $A_{yy}=14.82$ MHz, $A_{zz}=108.89$ MHz; $\tau = 3$ ns.

3.2.2 ESE-detected EPR measurements

ESE-detected EPR measurements were performed with MBP H85C in solution (pure) and samples with additions of non-spin-labeled MBP CI resulting in samples with fixed ratios of spin-labeled MBP H85C and non-spin-labeled MBP CI. The ratios were 1:1, 1:2, and 1:3 (labeled-to-non-labeled protein, Fig. 3.18).

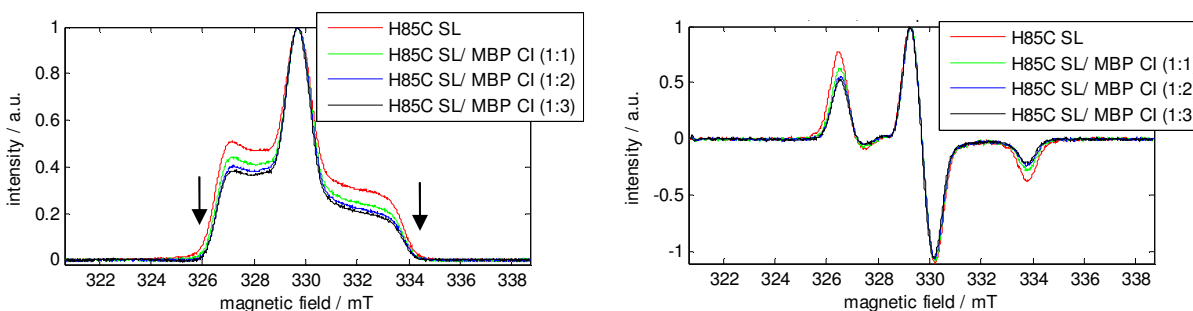


Fig. 3.18. ESE-detected EPR spectra of spin-labeled MBP H85C together with non-spin-labeled MBP CI (different ratios, left) and the correlated 2.5 G pseudomodulated spectra (right) detected at 20 K (integral normalized). The spectral width decreases significantly with increasing content of non-spin-labeled MBP (indicated by black arrows).

The addition of non-spin-labeled MBP CI leads to significantly decreased signal widths in the outer regions (indicated by black arrows) and a flattened shape of the overall spectrum.

3.2.3 2-pulse ESEEM measurements

2-pulse-ESEEM X-band measurements were performed at 50 K with ratios of spin-labeled MBP H85C to non-labeled MBP CI of 1:1, 1:2, and 1:3. Like before, measurements were performed at the position of the maximum and 2.5 mT towards a smaller magnetic field in the respective ESE spectrum (the latter values are given in parentheses, see Fig. 2.1 for details, Table 3.3). Real (bulk) physical concentrations were ~ 0.33 mM spin-labeled MBP H85C for all samples.

Table 3.3. Transversal relaxation times (T_2 time, in ns) determined by 2p-ESEEM at optimized attenuation of the pulse microwave and maximum spectral peak position. Values in parentheses stem from measurements performed at a position with a field-shift of -2.5 mT from maximum position (physical concentration of spins: 0.33 mM)

<i>sample</i>	<i>pure</i>	<i>1:1</i>	<i>1:2</i>	<i>1:3</i>
T_2 /ns	620 (790)	760 (960)	910 (1070)	930 (1070)

The T_2 times are in the range of about 600 (800) ns to 900 (1100) ns and increase for higher contents of non-spin-labeled MBP CI. At this point it has to be noted that sample 1:2 was prepared from sample 1:3 by adding additional spin-labeled MBP.

3.2.4 Instantaneous Diffusion measurements

Measurements were performed at 50 K with ratios of spin-labeled MBP H85C to non-labeled MBP CI of 1:1, 1:2, and 1:3 (like before). Data analysis clearly indicates that there is a dependence of the phase recovery time on the pulse flip angle and data. The linear fitting of the data leads to excellent results with very good correlation coefficients. The calculated spin concentrations were in the range of about 0.5 to 1.4 mM (real concentration of spins: 0.3 mM, Table 3.4).

Table 3.4. Spin concentrations determined by instantaneous diffusion measurements at the maximum spectral peak position. Values in parentheses are from measurements with a magnetic field-shift of -2.5 mT from maximum position.

<i>sample</i>	<i>pure</i>	<i>1:1</i>	<i>1:2</i>	<i>1:3</i>
c /mM	1.4 (0.8)	1.1 (0.5)	0.8 (0.4)	0.6 (0.1)

The local concentration of spins steadily decreases with increased contents of non-spin-labeled MBP CI within the sample. Values of 1.4 (0.8) mM for pure spin-labeled MBP H85C solution are opposed to values of about 0.6 (0.1) mM for the highest dilution with non-spin-labeled protein (1:3), which represents only ~ 40% of the concentration of the pure sample.

3.2.5 DEER measurements

DEER measurements were performed at 20 K with MBP H85C in solution (pure) as well as samples with ratios of spin-labeled MBP H85C to non-labeled MBP CI of 1:1, 1:2, and 1:3. The frequency difference $\Delta\nu$ between pump pulse and observer pulses was fixed to 70 MHz (~ 2.5 mT) for all measurements (Fig. 3.19, only data for the pure sample and the 1:1 and 1:3 dilutions are shown).

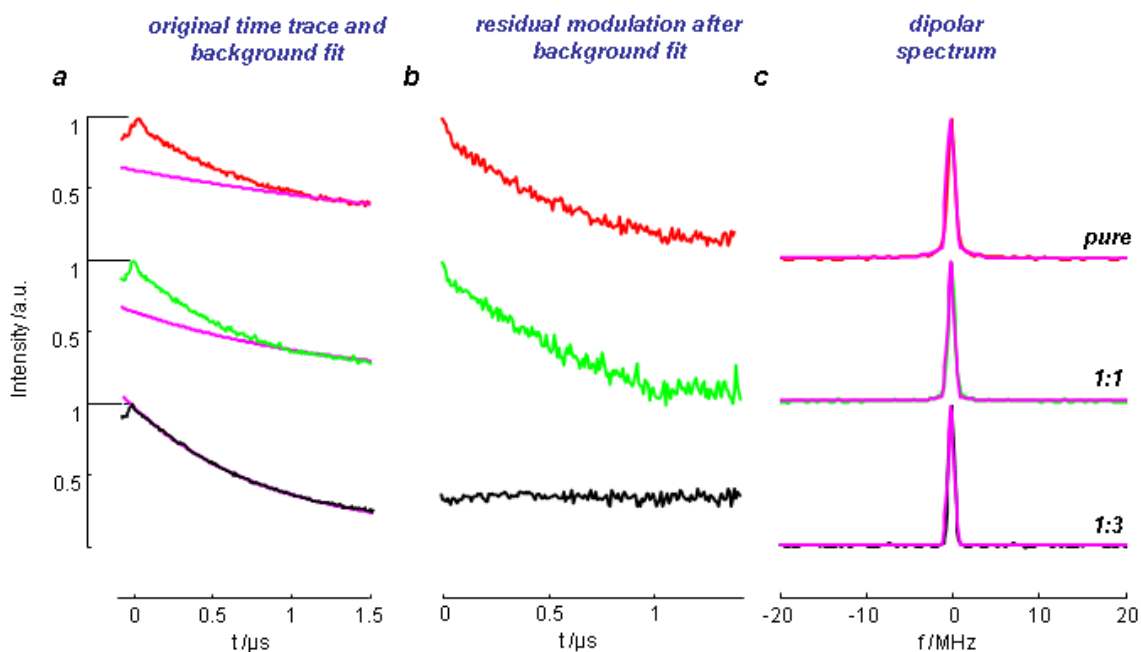


Fig. 3.19. Data obtained by DEER measurements at 20 K with MBP H85C in solution as well as samples with molar ratios of MBP H85C to unlabeled MBP CI of 1:1 and 1:3. $\Delta\nu$ between pump pulse and observer pulses was fixed to 70 MHz (~ 2.5 mT) for all measurements (Fig. 2.3). **a:** The original time traces deviate from a purely exponential decay for the pure MBP H85C and the 1:1 dilution. For the 1:3 dilution, the time trace is entirely given by the experimental background. **b:** Only for pure MBP H85C and the 1:1 dilution there is a significant modulation of the background corrected time trace. **c:** Dipolar spectra consisting of a residual background artifact (as seen in the dipolar spectrum of the 1:3 dilution without modulation) and spectral broadening in the frequency region of about -4 to -0.5 and 0.5 to 4 MHz containing the distance information. Simulations of the dipolar spectra worked best by assuming a dominant distance of about $3.0 (\pm 0.3)$ nm with a decreasing intensity for higher dilutions (pure: 100%; 1:1: 42%; 1:3: 5%)

In the original DEER time traces for the pure sample and the sample with 1:1 dilution a significant part of the spectrum can be considered to stem from detected distances within the sample (fit for the experimental background in magenta, Fig. 3.19, **a**). At a dilution of 1:3 the whole trace spectrum seems to entirely consist of experimental background. This interpretation is clearly supported by the plot of the residual modulation in time domain after background correction. Here, a remaining modulation is only observed for the pure MBP H85C and the 1:1 dilution (Fig. 3.19, **b**). In the 1:3 dilution no residual modulation is found. Nevertheless, also for these data the dipolar spectrum reveals a peak that can therefore be considered as a background artifact (Fig. 3.19, **c**). Thus, the significant distance information seems to be represented in the spectral

Results

regions of about -4 to -0.5 and 0.5 to 4 MHz, as can be seen by the significantly broadened spectra of the pure sample and the 1:1 dilution within this frequency region. Simulations of the dipolar spectra led to the best results with a dominant distance of about 3.0 (± 0.3) nm. From simulations of the dipolar spectra it becomes clear that higher dilutions result in decreasing intensities of the distance distribution around 3 nm. The simulations comprise 100% in pure MBP H85C, 42% in the 1:1 dilution, and only about 5% in the 1:3 dilution.

The sample with a ratio of 1:2 was prepared in a different way compared to the other samples of the dilution. It was prepared by adding spin-labeled MBP to the 1:3 sample in order to probe stability of the proposed MBP aggregates. In fact, the addition of labeled MBP to the 1:3 dilution did not result in more detectable distances (neither in the original time data nor in the dipolar spectrum) which indicates that MBP, which aggregated during the preparation of the 1:3 dilution sample, persists and does not allow significant formation of new spin-labeled MBP aggregates resulting in detectable distances (data not shown).

3.3 EPR experiments on spin-labeled MBP in artificial membrane vesicles

3.3.1 CW EPR measurements

CW EPR measurements with spin-labeled MBP in artificial membrane vesicles were performed with sets of MBP in LUVs and a lipid-to-protein-ratio (LPR) of 378:1 (referred to as 'MBPI'), MBP in LUVs (LPR 567:1, referred to as MBPII), and MBP in MLVs (LPR 567:1, referred to as MBPIII; Fig. 3.20). Please note, that all abbreviations of sample names are summarized in Tab. I (page 111, Appendix). CW EPR spectra of the different spin-labeled MBP samples in artificial membrane vesicles revealed no significant variations within one set of samples (MBPI, MBPII, and MBPIII). Only for the CW spectrum of MBPI H85C there seems to occur a slight signal broadening with respect to the other samples ($\Delta 2A_{zz}=0.35$ mT). In the measurements with MBPIII the spectral width of S17C seems to be narrowed to a small extent (red curve, $\Delta 2A_{zz}=0.95$ mT). Simulation of the spectra lead to good results for $g_{xx}=2.0092$, $g_{yy}=2.0054$, $g_{zz}=2.0021$, $A_{xx}=13.62$ MHz, $A_{yy}=14.82$ MHz, and $A_{zz}=100.89$ MHz for MBPI and II and $A_{zz}=97.89$ MHz for MBPIII.

Additional measurements were performed at room temperature for MBPII (Fig. 3.21). Spectra of samples with labeling positions S17C, CS159C, and S17C/S159C exhibit only small changes of the overall spectral shape. Small differences only occur for the intensities of the three line peaks. The spectrum of the sample labeled at the H85C position yields a clear broadening of all spectral features. Rotational correlation times from spectral simulation of are $\tau =12.5$ ns for H85C and $\tau =5$ ns for S17C, S159C, and S17C/S159.

Results

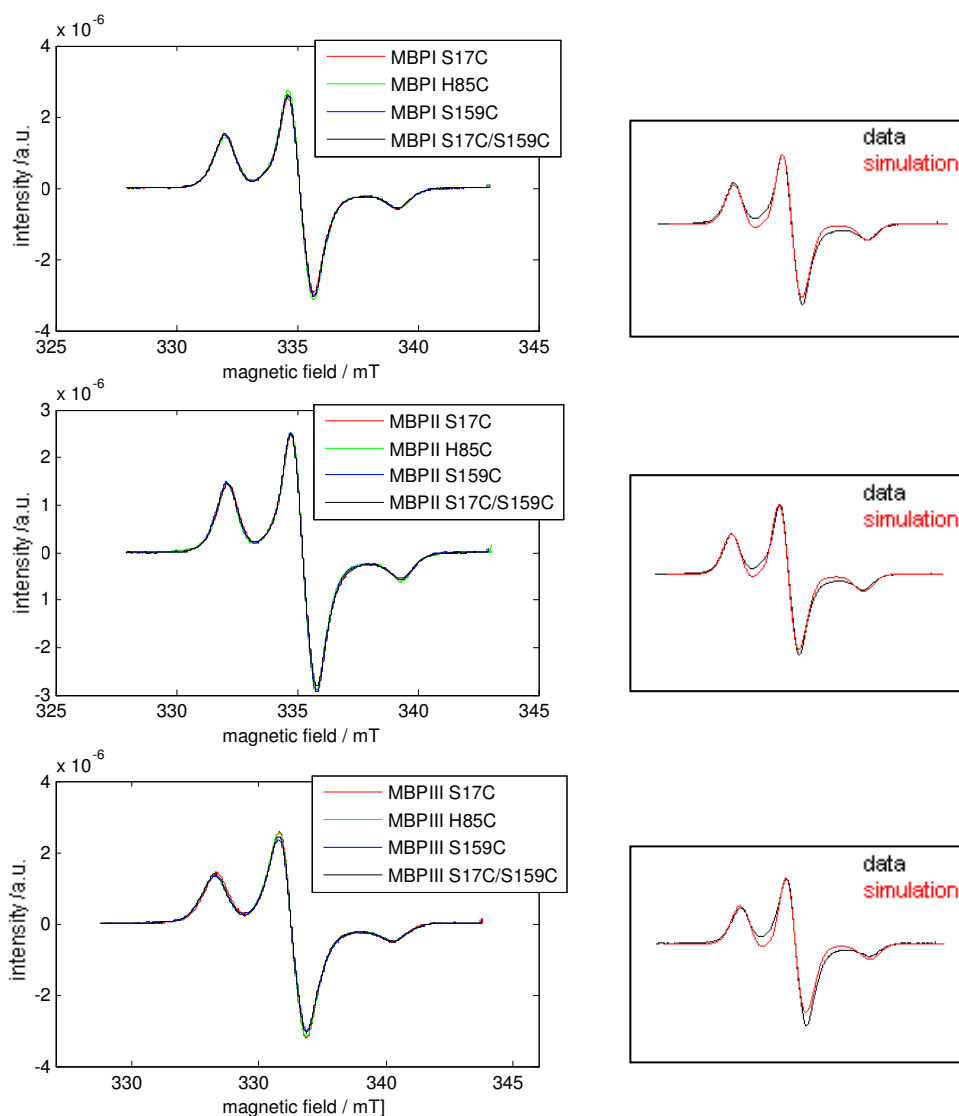


Fig. 3.20. CW EPR spectra of MBP in LUVs LPR 378:1 (MBPI, on top) detected at 103 K, MBP in LUVs LPR 567:1 detected at 103 K (MBP II, in the middle), and MBP in MLVs LPR 567:1 (MBP III, on the bottom) detected at 77 K (integral normalized). General spectral shape, peak positions, and signal width are almost the same for all spectra in one sample set. Only the CW EPR spectrum of MBPI H85C seems to feature a slightly broadened signal. For the MBP III sample set the spectrum of S17C seems to be narrowed to a small extent. Simulations (on the right) were performed with the following simulation parameters for MBPI and MBP II: $g_{xx}=2.0092$, $g_{yy}=2.0054$, $g_{zz}=2.0021$; $A_{xy}=13.62$ MHz, $A_{yy}=14.82$ MHz, $A_{zz}=100.89$ MHz. MBP III: $A_{zz}=97.89$ MHz.

Results

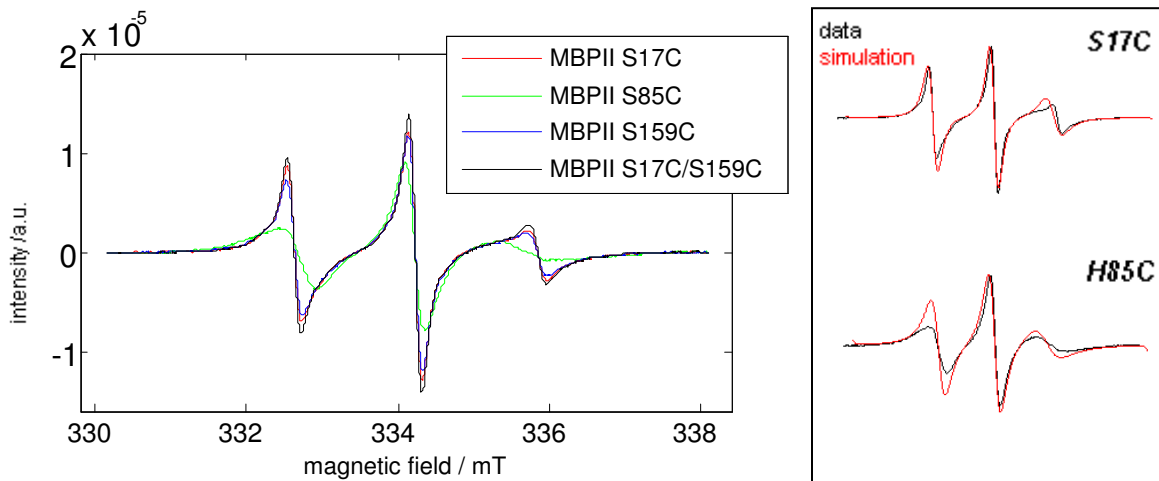


Fig. 3.21. CW EPR spectra of MBPII in LUVs LPR 567:1 (MBPI, on top) detected at room temperature (integral normalized) and simulations for S17C (also representative for S159C and S17C/S159C) and H85C. Spectra of the samples with labeling position S17C, S159C, and S17C/S159C reveal only slight spectral differences. They differ only in the intensities of the three line peaks. With respect to the spectrum of H85C a clear broadening of all spectral features is observed. Simulation parameters for S17C: $g_{xx}=2.0092$, $g_{yy}=2.0054$, $g_{zz}=2.0021$; $A_{xx}=13.61$ MHz, $A_{yy}=14.81$ MHz, $A_{zz}=101.89$ MHz, $\tau =5$ ns.; H85C: $A_{zz}=97.89$ MHz, $\tau =12.5$ ns.

Additional CW EPR measurements at 77 K were performed with samples of MBPI H85C with and without NaCl (~500 mM final concentration, Fig. 3.22). The resulting spectra approximately feature the same spectral shape but simulations indicate that the spectrum measured with NaCl tends to show a more Lorentzian shape of the peaks which correlates to a slightly broadened peak structure at its border regions.

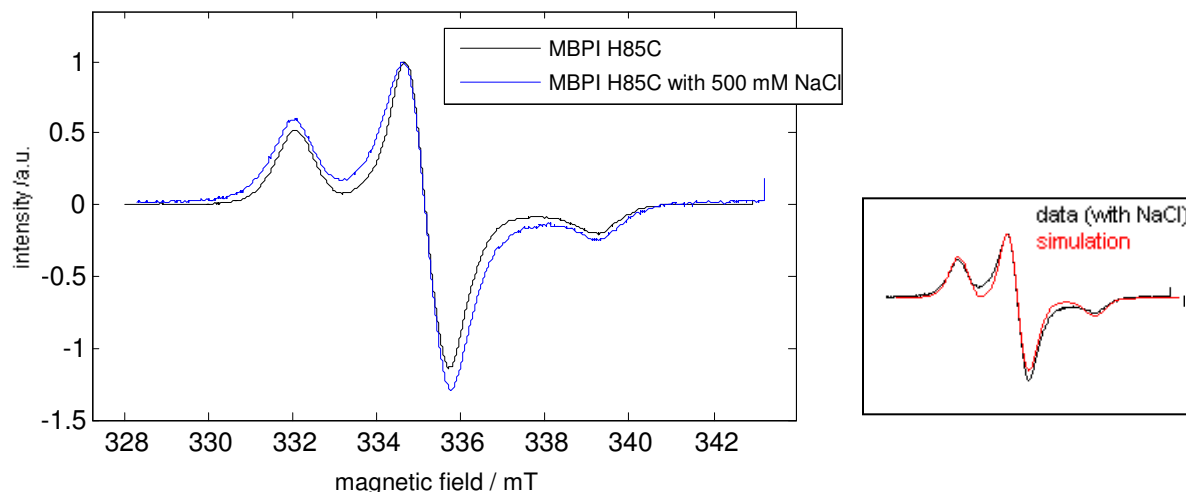


Fig. 3.22. CW EPR spectra of MBPI H85C with and without NaCl (500 mM final concentration) detected at 77 K (integral normalized). The spectra feature similar spectral shape with tendency of slightly broadened peaks for the measurements including NaCl. Simulation parameters for MBPI H85C with NaCl: $g_{xx}=2.0092$, $g_{yy}=2.0054$, $g_{zz}=2.0021$; $A_{xx}=13.62$ MHz, $A_{yy}=14.82$ MHz, $A_{zz}=100.89$ MHz for both samples.

3.3.2 ESE-detected EPR measurements

ESE-detected EPR measurements were performed with MBPI, II, and III at 20 and 50 K. ESE measurements resulted in very similar spectra for all sets of spin-labeled MBP in artificial membrane vesicles at both temperatures (Fig. 3.23, spectra at 50 K not shown). Small differences within the sample sets only occur, like in the CW EPR measurements, for the MBPI H85C sample, where slight line broadening is observed. Again, in the MBPIII sample set (MBP in MLVs), S17C seems to feature a slightly smaller signal width when compared to the other samples of the set. Only in the ESE spectrum of MBPI H85C, a slight signal broadening is observable. For the MBPIII sample set the spectrum of S17C seems to be slightly narrowed. In addition to the plots for comparison of the ESE-detected spectra within one sample set, which were just presented, plots for MBP with the same spin labeling position but different LPR or membrane vesicle conditions have been analyzed (Fig. 3.24).

Results

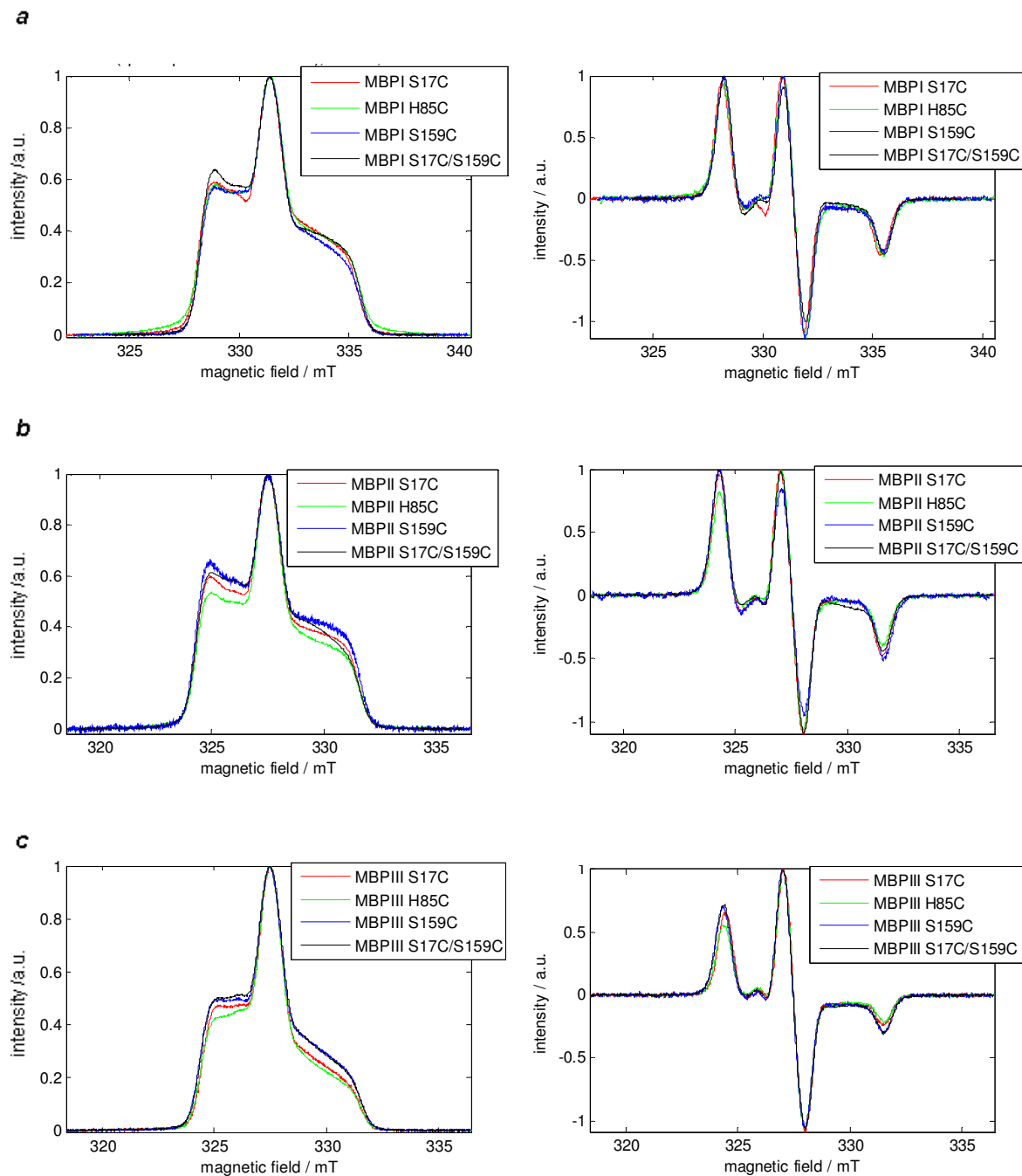


Fig. 3.23. ESE-detected EPR spectra of spin-labeled MBP in LUVs LPR 378:1 (MBPI) **a**, in LUVs LPR 567:1 (MBPII) **b**, and in MLVs LPR 567:1 (MBPIII) **c**, detected at 20 K (left column). The respective, pseudomodulated spectra are shown on the right (normalized to maximum). General spectral shape, peak positions, and signal width are almost the same for all spectra within one sample set. Only the ESE spectrum of MBPI H85C seems to show a slightly broadened signal. With respect to the MBPIII sample set the spectrum of S17C seems to be slightly narrowed.

Results

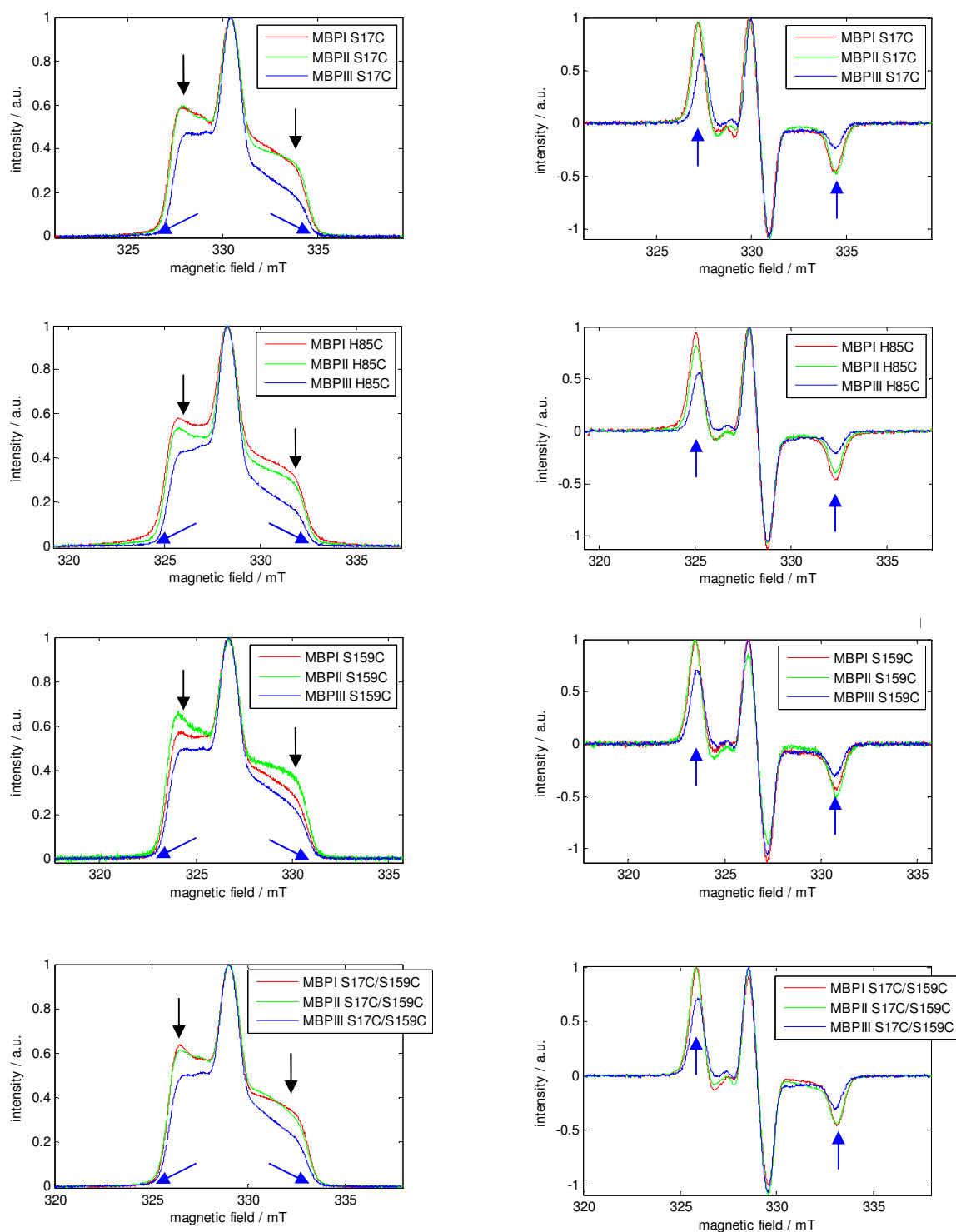


Fig. 3.24. ESE-detected EPR spectra of spin-labeled MBP plotted in groups according to the spin labeling position at 20 K (left column). The respective pseudomodulated spectra are shown on the right (normalized to maximum). In general, comparison of the spectral shape reveals small differences for MBP I and II. MBP III features a flattened shoulder region when compared to MBP I or II (indicated by the arrows). Also the spectral width is reduced ($\Delta B=0.25$ mT), which is better observable in the pseudomodulated spectra (see blue arrows).

Results

No significant differences in the spectral shape of data stemming from MBPI and II are found. Differences in the plots for one labeling position only occur for spectra of MBPIII, which feature significantly flattened shoulder regions and a lower line width, which can be seen both in the border regions of the ESE spectra and the outer peaks of the pseudomodulated spectra (indicated by blue arrows).

Also, the influence of thawing and re-freezing on the sample was tested by ESE detected measurements with samples of MBPI and II H85C at 20 and 50 K (Fig. 3.25). The ESE detected spectra of the thawed and re-frozen samples of MBPI and MBPII showed a significantly smaller line width ($\Delta B \sim 0.1$ mT).

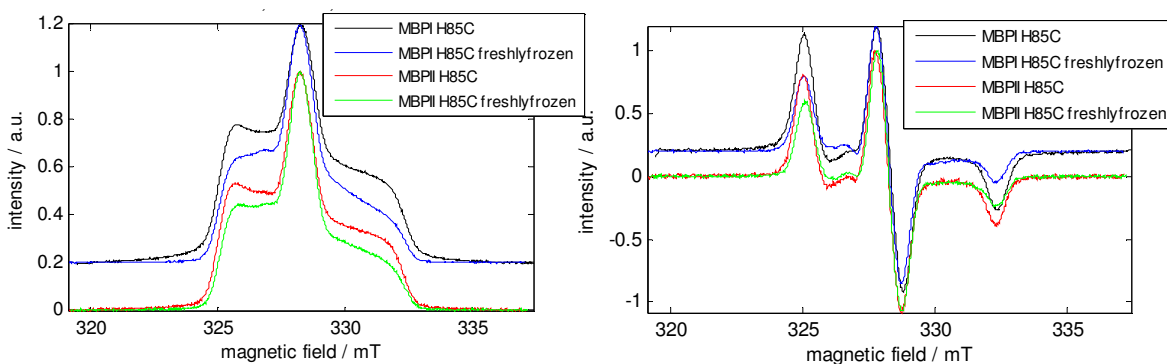


Fig. 3.25. ESE-detected EPR spectra of spin-labeled MBPI H85C (left) and the pseudomodulated spectra ($\Delta B = 0.25$ mT, right) at 20 K. A significant decrease of the spectral line width ($\Delta B = 0.1$ mT) is detected for the thawed and re-frozen MBP samples.

Again, the effect of NaCl on MBP samples was tested. NaCl was added to samples of MBPI S17C and S17C/S159C to establish a final NaCl concentration of about 500 mM. In this case, the obtained spectra do not significantly vary from the original spectra without NaCl (Fig. 3.26).

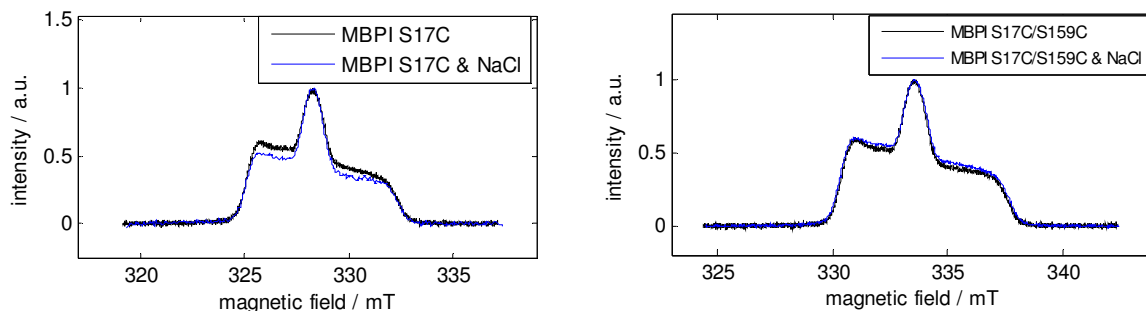


Fig. 3.26. ESE-detected EPR spectra of spin-labeled MBPI S17C (left) and S17C/S150C (right) together with 500 mM NaCl (maximum normalized). No significant spectral variations are observed here.

3.3.3 2-pulse ESEEM measurements

2 pulse-ESEEM at 50 K was performed systematically with MBP in LUVs and a lipid-to-protein ratio of 378:1 (MBPI), a lipid-to-protein ratio of 567:1 (MBPII), and MBP in MLVs with a lipid-to-protein ratio of 567:1 (MBPIII) in order to determine phase recovery times (transversal relaxation, T_2 time) of the different samples. Measurements were performed at the position of the maximum and 2.5 mT towards a smaller magnetic field in the ESE-detected EPR spectrum (the latter values are given in parentheses, Table 3.5).

Table 3.5. Transversal relaxation times (T_2 time, in ns) determined by 2p-ESEEM at optimized attenuation of the pulse microwave and maximum spectral peak position. Values in parentheses stem from measurements with a B_0 -shift of -2.5 mT from maximum position for the 2p-ESEEM measurements (Fig. 2.1).

	<i>sample</i>	<i>S17C</i>	<i>H85C</i>	<i>S159C</i>	<i>S17C/S159C</i>
T_2 time /ns	MBPI LUV	470 (660)	560 (820)	-	450 (630)
T_2 time /ns	MBPII LUV	530 (760)	610 (840)	529 (720)	539 (800)
T_2 time /ns	MBPIII MLV	640 (860)	800 (1160)	798 (1020)	708 (920)

The T_2 times are in the range of about 450 (660) ns to 560 (820) ns for MBPI, 530 (760) ns to 610 (840) ns for MBPII, and 640 (860) ns to 800 (1160) ns for MBPIII. In general, T_2 times measured at the z-shoulder (Max-2.5 mT) were about 1.5 times larger than those measured at maximum position. Additionally, there seems to be a tendency of increasing T_2 times from MBPI and MBPII in LUVs to MBPIII in MLVs. Values of samples with the labeling position H85C feature the highest T_2 times in each sample set.

The addition of NaCl to MBPI S17C results in T_2 times of about 420 (590) ns, which are comparable to those without NaCl. Further, MBPII H85C was thawed and re-frozen again in order to study the effects caused by the freeze-thaw-mechanism. Here, values of about 1060 (1520) ns are measured, an increase of about 1.7 times in comparison to the non-thawed samples.

3.3.4 Instantaneous Diffusion measurements

Measurements on all three sets of membrane-bound MBP samples were performed at 50 K. Data analysis clearly indicates that there is a dependence of phase recovery time on the pulse flip angle (Fig. 3.27).

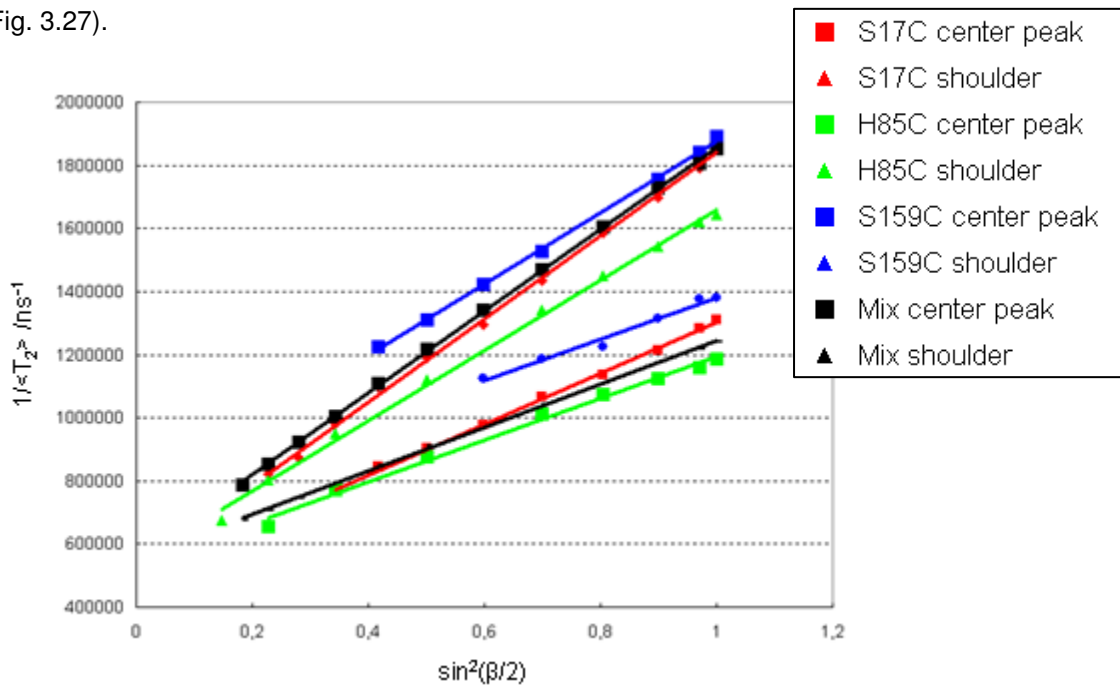


Fig. 3.27. Relaxation times T_2 plotted against the flip angle β in the form $1/\langle T_2 \rangle$ (in ns) vs. $\sin^2(\beta/2)$. Data points obtained for instantaneous diffusion measurements performed at the maximum peak position of the ESE-detected EPR spectra are marked with squares, data points from measurements obtained at the position of the maximum -2.5 mT are marked with triangles (see Fig. 2.1 for detail). For all measurements linear correlations are observed and fitted. Resulting slopes and correlation coefficients were in a well acceptable data range and used for further analysis.

Linear fittings were performed in order to further analyze the data. The final, calculated spin concentrations were in the range of about 0.6 to 1.8 mM for all samples (Table 3.6).

Table 3.6. Local spin concentrations determined by instantaneous diffusion measurements at maximum spectral peak position. Values in parentheses stem from measurements with a B_0 -shift of -2.5 mT from maximum position for the 2p-ESEEM measurements.

	<i>sample</i>	<i>S17C</i>	<i>H85C</i>	<i>S159C</i>	<i>S17C/S159C</i>
<i>c/mM</i>	MBPI LUV	2.8 (1.6)	2.8 (1.6)	-	3 (1.8)
<i>c/mM</i>	MBPII LUV	2.6 (1.6)	2.2 (1.3)	2.2 (1.3)	2.6 (1.4)
<i>c/mM</i>	MBPIII MLV	1.8 (0.9)	1.8 (0.9)	1.4 (0.8)	1.5 (0.8)

Results

The experimentally obtained local spin concentration in one sample set only changes slightly. Comparison of the values detected at maximum peak position and the values stemming from measurements at the low-field shoulder position of the correlated ESE spectrum differ by a factor of about 1.7 – 2 (with higher values for the maximum position). Another trend is reflected by the decreasing concentrations for the sample sets in the order from MBPI (~2.9 mM) over MBPII (~2.4 mM) to MBPIII, which feature the smallest concentration of spins (~1.6 mM).

The spin concentration for the experiment with MBPI S17C/S159C and NaCl is calculated to about 3.5 (2.2) mM, about 1.15 times higher than without NaCl. Thawing and re-freezing of MBPII H85C leads to measured spin concentrations of about 1.6 (0.6) mM (about 72% of the original value).

3.3.5 3-pulse ESEEM measurements

3-pulse ESEEM was performed at 20 K with MBP_{II} H85C and the whole set of MBP_{III} samples with $\tau=136$ ns and $\tau=176$ ns in order to resolve couplings to nuclei in the molecular neighborhood (< 1 nm) of the attached spin labels. Besides the typical coupling of about 14 MHz for protons an additional coupling of about 2.2 MHz is observed for all samples, with increased intensities for the samples MBP_{III} H85C and MBP_{II} H85C (Fig. 3.28).

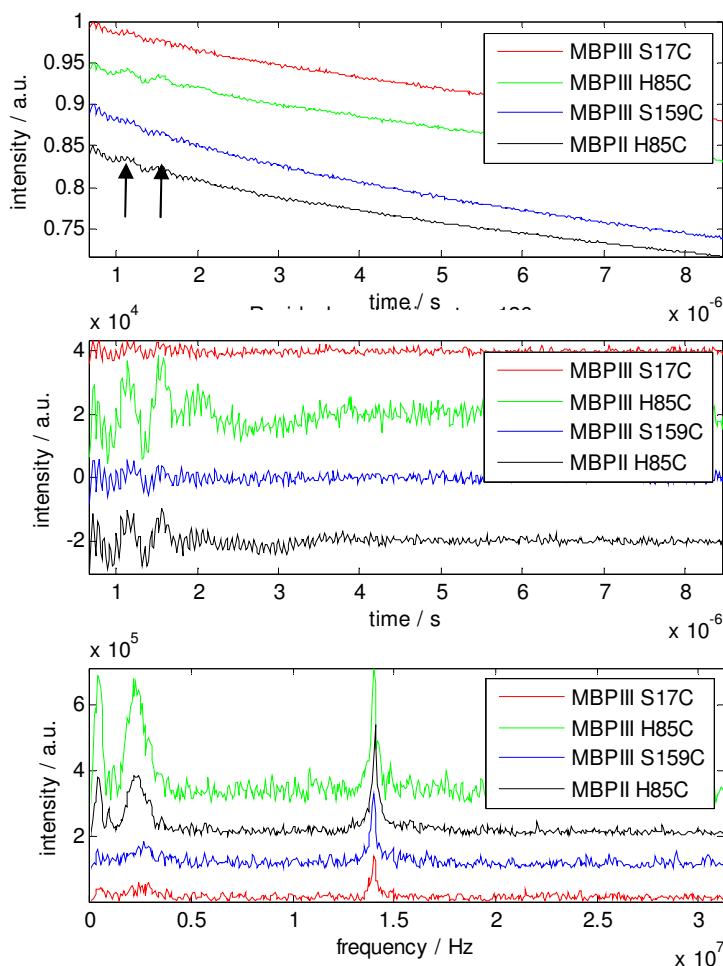


Fig. 3.28. 3-pulse ESEEM experiments measured at 20 K with MBP_{II} H85C and MBP_{III} S17C, H85C, and S159C for $\tau=136$ ns (see Fig. 2.2 for details). **a:** Original 3-pulse ESEEM time data. **b:** Residual modulations after background fitting with a stretched exponential. **c:** Frequency spectrum after Fourier transformation. Besides the dominant coupling frequency of about 14 MHz for proton coupling there is another dominant frequency at about 2.2 MHz, which is best observed for $\tau=136$ ns for measurements with MBP_{III} H85C and MBP_{II} H85C and is already observable in the original time trace (indicated by black arrows).

3.3.6 HYSORE measurements

X-band HYSORE experiments were performed at 20 K with samples in artificial membrane vesicles MBPIII S17C, H85C, and S159C as well as MBPII H85C (at this point it should be mentioned that MBPII H85C was thawed for a special purpose before it was frozen again for HYSORE measurements). In the HYSORE spectra well pronounced ridges appear along the antidiagonal in the (+,+) quadrants of the frequency spectrum for all samples besides the characteristic matrix peak of the protons at 14 MHz (Fig. 3.29, indicated by black arrows). An additional peak is observed at the position of the ^{31}P Larmor frequency ($\nu_P=5.6$ MHz at 327.8 mT, indicated by red arrows) for the samples MBPIII S17C and H85C and, like in 3-pulse ESEEM measurements, a further peak at 2.2 MHz, which seems to be most dominant for MBPII H85C and MBPIII H85C with relation to the intensities of the other peaks (magenta arrows). A correlation ridge at the position of the ^{13}C Larmor frequency ($\nu_C=3.5$ MHz at 327.8 mT, indicated by green arrows) is obtained for all samples. In the strong coupling quadrant (-,+) ridge-like structures appear in the lower right corners (with $A \approx 2 - 8$ MHz, grey arrows) together with additional ridges along the antidiagonal in the central part of the quadrant (indicated by red dotted circles).

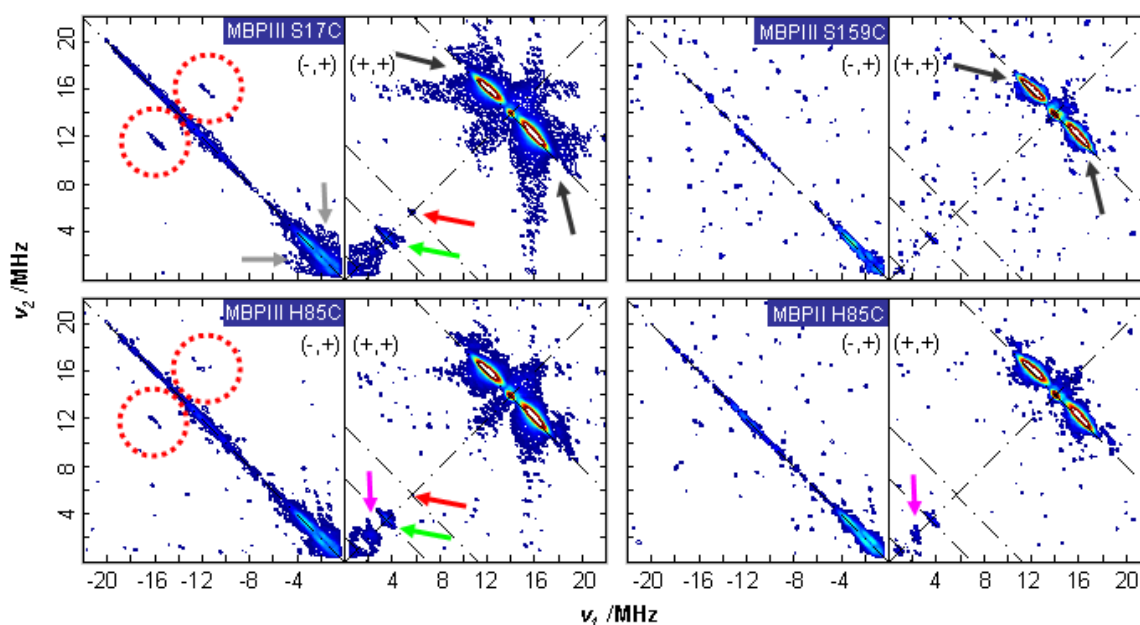


Fig. 3.29. X-band HYSORE spectra of MBPIII S17C, H85C, and S159C and MBPII H85C at 20 K ($\tau = 136$ ns). Only the (-,+) and the (+,+) quadrant of the frequency domains are plotted here (see Fig. 2.2 for details). In the weak coupling quadrant of the frequency spectra the characteristic cross peak of weak proton coupling at ~ 14 MHz is obtained for all samples with additional proton correlation ridges along its antidiagonal. A further cross peak is detected at the ^{31}P Larmor frequency ($\nu_P=5.6$ MHz at 327.8 mT, indicated by red arrows). Samples of MBPIII S17C and H85C reveal a correlation ridge orientated along the antidiagonal at the ^{13}C Larmor frequency ($\nu_C=3.5$ MHz at 327.8 mT, indicated by green arrows). In the strong coupling quadrant pronounced spectral features occur in the region of 0 – 4 MHz for all spectra which are accompanied by additional ridges along the antidiagonal at about 14 MHz.

3.3.7 DEER measurements

DEER measurements are the central experiment for obtaining structural information about MBP in solution and together with artificial membrane vesicles. Under the latter conditions, measurements were performed with two sets of different lipid composition of the vesicles (LUVs and MLVs). Additionally, for the LUVs, two different lipid-to-protein ratios have been selected for measurements: MBPI with an LPR of 376:1 and MBPII with an LPR of 567:1. Measurements, with solely changing lipid-to-protein ratios (MBPI vs. MBPII), show very similar results. In the following, the results for the lipid-to-protein ratio of 567:1 (MBPII) are presented in detail.

Original DEER time data were background corrected using a 3D background fit. 3D background fitting was selected, first, because it represents the most simple background model and, second, because comparison to e.g. data analysis performed with a 2D background model (as could be assumed with regard to the artificially introduced membranes) did not lead to significant differences.

The resulting residual time traces for the different samples of MBP in vesicles reveal no dominant modulations but resembled one modulation spanning the whole time scale of the measurement. In the measurements of MBPII significant differences are observed for the modulation depth of the different spectra (Fig. 3.30, **a**). While modulation depths of the samples S17C, S159C, and S17C/S159C vary only to a small extent, the modulation depth is decreased for H85C. Additionally, the spectrum of H85C seems to lack specific contributions leading to a faster spectral decrease in the beginning of the spectrum, which is present for the other samples (indicated by black arrows). With respect to the Fourier transformed dipolar spectra, again, only small spectral differences are observed between S17C, S159C, and S17C/S159C (Fig. 3.30, **b**). Compared with the spectrum of H85C they feature a higher proportion of spectral fractions in the region of about 2 to 5 MHz (and -2 to -5 MHz, respectively). Therefore, the dipolar spectrum of H85C seems to be narrower than those of the other samples. Simulations of the Pake patterns reveal a distribution of distances in a medium range of about 2.5 (\pm 0.3) nm. Finally, optimizations indicate a significant proportion of distances in the range of 2.5 (\pm 0.3) nm and a distance of the center peak of about 4.1 nm for S17C, S159C, and S17C/S159C. With regard to H85C the spectrum is best simulated for parameters of about 2.5 (\pm 0.3) nm (like before, but with decreased intensity (~40%)) and a distance for the center peak of about 4.2 nm. Data were also analyzed by fitting a single Gaussian to the dipolar data (Fig. 3.30, **c**). Here, only slight variations in distance distributions are observed with a trend towards higher distances for S17C, H85C, and S17C/S159C.

Results

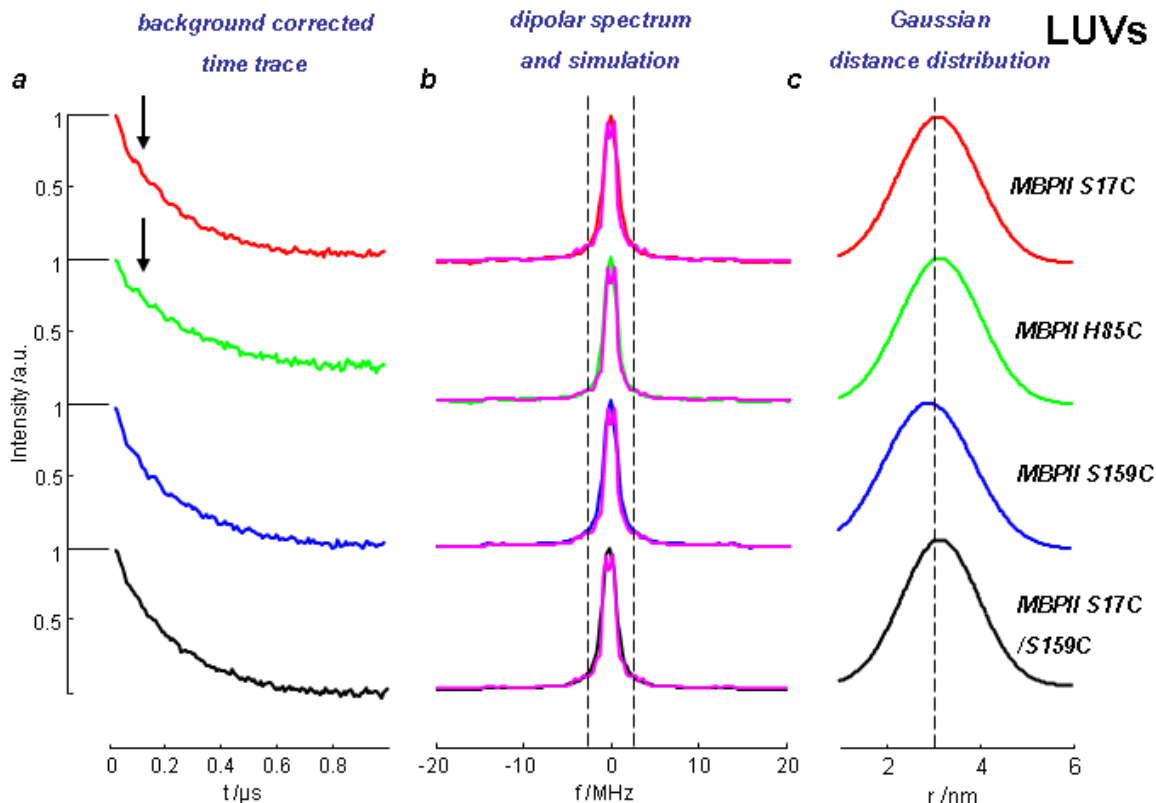


Fig. 3.30. DEER data obtained for measurements with spin-labeled MBP (different labeling positions) in LUVs (LPR 567:1) at 50 K with a detection time of 1100 ns (for details see Fig. 2.3). **a:** 3D background corrected DEER time data. **b:** Fourier transformed dipolar spectra with simulations (magenta). **c:** Gaussian distance distribution fitted to the dipolar spectra.

DEER measurements on spin labeled MBP in MLVs in general reveal the same trends as the measurements in LUVs presented above. The background corrected time traces of S17C, S159C, and S17C/S159C show greater modulation depths than for H85C (Fig. 3.31, **a**). With respect to the data of MBP in LUVs, modulation depth seems to be decreased by a factor of about 0.8 for all samples here (total values: MBPII 0.48, MBPIII: 0.58). Again, short distances do not contribute to the early region of the time trace of H85C (marked by arrows) compared to the other samples. These findings are also supported by the dipolar spectra, which feature an even narrower spectrum for the H85C labeling position in MLVs than in LUVs. The spectra of S17C, S159C, and S17C/S159C, though, remain unchanged (Fig. 3.31, **b**). The broadest spectrum is observed for S159C, with a pronounced intensity increase in the border region of the dipolar spectrum (indicated by red arrows). Simulations of the dipolar spectra refer to distance values of about 2.85 (± 0.2) nm for the medium distance region and about 4.2 nm for the central peak for S17C, S159C, and S17C/S159C. For H85C, simulations reveal a distance of about 4.25 nm for the central peak and decreased intensities ($\sim 40\%$) of the distances in the medium range (2.85 ± 0.2) nm. Simulation of the spectrum for S159C succeeds best with an intensity increase of about

Results

15% for the medium range distances. Distance distributions based on Gaussian fitting to the dipolar spectrum, for the MLV samples, indicate increased proportions of longer distances for the H85C labeling position (Fig. 3.31, **c**). S159C features a higher fraction of shorter distances, which is consistent with the pronounced broadenings in the dipolar spectrum.

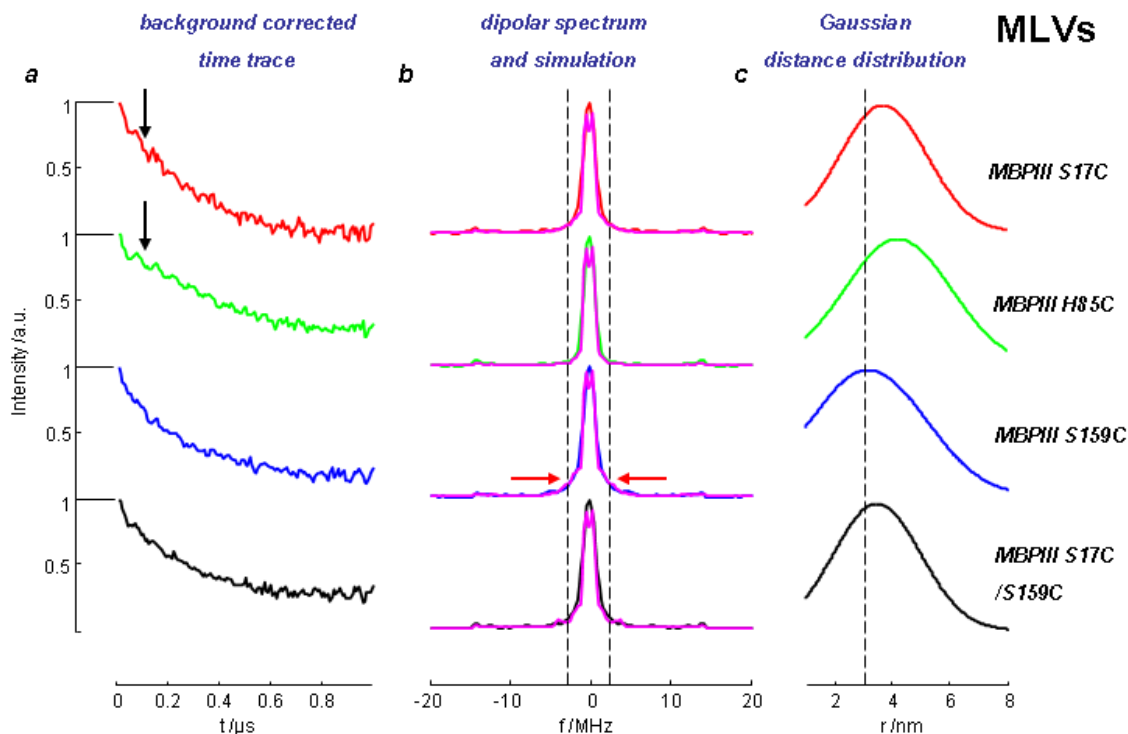


Fig. 3.31. DEER data obtained for measurements with spin-labeled MBP (different labeling positions) in MLVs (LPR 567:1) at 20 K with a detection time of 1100 ns. **a**: 3D background corrected DEER time data. **b**: Fourier transformed dipolar spectra with simulations (magenta). **c**: Gaussian distance distribution fitted to the dipolar spectra.

Additional data analysis was performed using the possibility of spin counting within the *DEERAnalysis* software package. Based on a reference sample with a well defined system of two coupled spins at a fixed distance (2.8 nm), the relative fraction of coupled spins was determined for the observed DEER time data with spin labeled MBP (Table 3.7).

Table 3.7. Results for spin counting experiments obtained with the *DEERAnalysis* software for MBPI, MBPII, and MBPIII. All input spectra were normalized to a time axis of 1000 ns for comparison. The numbers give can be interpreted as the number of spins interacting through dipolar couplings (on average).

	<i>sample</i>	<i>MBPI</i>	<i>MBPII</i>	<i>MBPIII</i>
№ spins	S17C	1.8	2.05	1.8
№ spins	H85C	2.3	1.75	1.5
№ spins	S159C	1.75	2	1.7
№ spins	S17C/S159C	2.2	2	1.6

Results

For measurements with MBPI and II (MBP in LUVs), about two coupled spins are responsible for the DEER results. With respect to MBPIII (in MLVs) a slightly decreased number of about 1.6 - 1.7 spins are characteristic for the observed DEER data. No special trends within one sample set are observed since deviations of the values seem to lie within measurement error. Only H85C of the sample set I and II deliver slightly decreased numbers of coupled spins.

DEER measurements were performed at d_2 values of 1100 ns, 1500 ns, and 2400 ns in order to study effects of the characteristic DEER dipolar evolution times τ_2 (d_2 ; interpulse delay between pump- and observer pulse) on the obtained DEER results. The data were systematically analyzed for MBPII S17C based on dipolar spectra (Fig. 3.32, **a**).

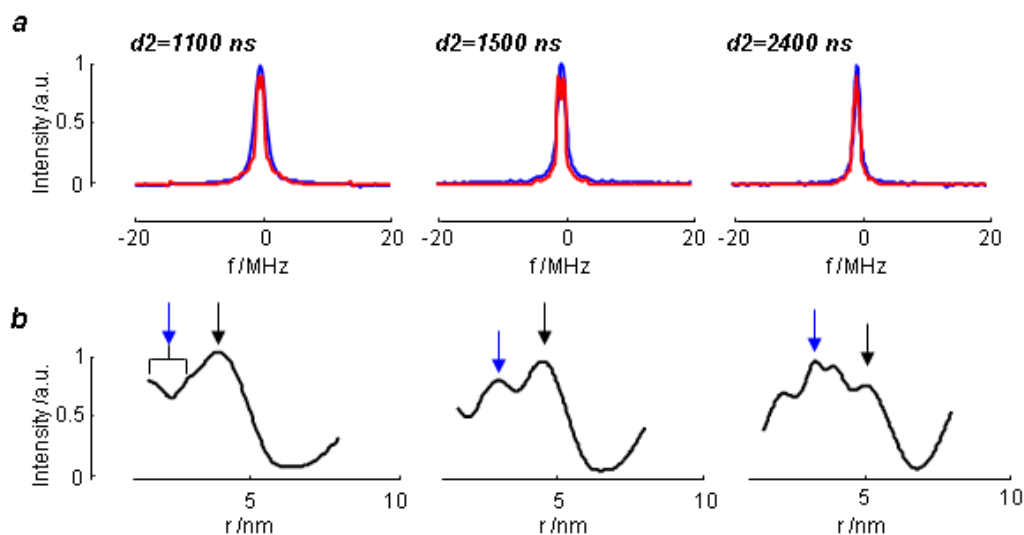


Fig. 3.32. DEER dipolar data for measurements with spin-labeled MBP S17C in LUVs (LPR 567:1) at 20 K with detection times (d_2) of 1100, 1500, and 2400 ns). **a**: Fourier transformed dipolar spectra with simulations (red) after 3D background correction. **b**: DEER distance distributions of the same data obtained by *DEERAnalysis* with Tikhonov regularization.

Simulations of the dipolar spectra work well for $\tau_2/d_2=1100$ ns with a proportion of medium range distances of about $2.5 (\pm 0.2)$ nm for the spectral border regions and 4.1 nm for the central peak (like presented before, MBP in LUVs). For $d_2=1500$ ns, the retrieved distances are $2.8 (\pm 0.2)$ nm and 4.2 nm. For $d_2=2400$ ns, distances of $3.2 (\pm 0.3)$ and 5.33 nm are obtained, respectively. *DEERAnalysis* with Tikhonov regularization delivers values of about 3.9 nm for the maximum peak of the distance distribution (Fig. 3.32, **b**, indicated by black arrows) and several peaks around 2.5 nm (indicated by blue arrows) for $d_2=1100$ ns. Distances for $d_2=1500$ and 2400 ns are about 2.8 and 3.1 nm for the medium range distances and 4.5 and 5.3 nm for the largest distance peak. The observed values match well with the values simulated manually in the frequency domain and reflect a steady increase of the absolute values of the distances with

Results

increasing d_2 times. For the distance distribution obtained by *DEERAnalysis* at 2400 ns the medium range distance represents the dominant part of the distribution. These results indicate that modification of d_2 only leads to slight changes of the characteristic distances detected so far (*i.e.* a distance of about 2.5 nm for $d_2=1100$ ns resembles a distance of about 3 nm for $d_2=2400$ ns). This means that the characteristic distance of about 2.5-2.8 nm detected for all measurements with spin-labeled MBP (d_2 times of 1100 ns) most likely tend towards about 3 nm in reality, since greater d_2 times (like e.g. 2400 ns) minimize the influence of background artifacts and lead to more reliable results.

Further DEER measurements were performed probing the effect of NaCl addition (~500 mM) to MBP in artificial membrane vesicles as well as a test checking whether thawing and re-freezing of MBP samples results in variation of DEER data (Fig. 3.33). One effect of NaCl and thawing and re-freezing of the sample (or the sample preparation) is represented by the reduced modulation depth for both measurements as can be seen in the original background corrected time traces (Fig. 3.33, **a**). The overall spectral shape of the time traces of MBP with NaCl and without NaCl as well as of the normal and re-frozen MBP samples are almost identical, as is best seen with modulation depth scaling for the time traces of both measurements (Fig. 3.33, **b**). Therefore also the dipolar data of both pairs of DEER measurements are almost identical and were fitted with the same parameters of the original samples (MBP without NaCl and MBP which was not thawed and re-frozen, Fig. 3.33, **c**). Distance distributions obtained from measurements do not reveal any significant variations (Fig. 3.33, **d**). The slight shift in the time traces for the re-frozen MBP stems from the higher level of proton coupling at about 14 MHz.

Results

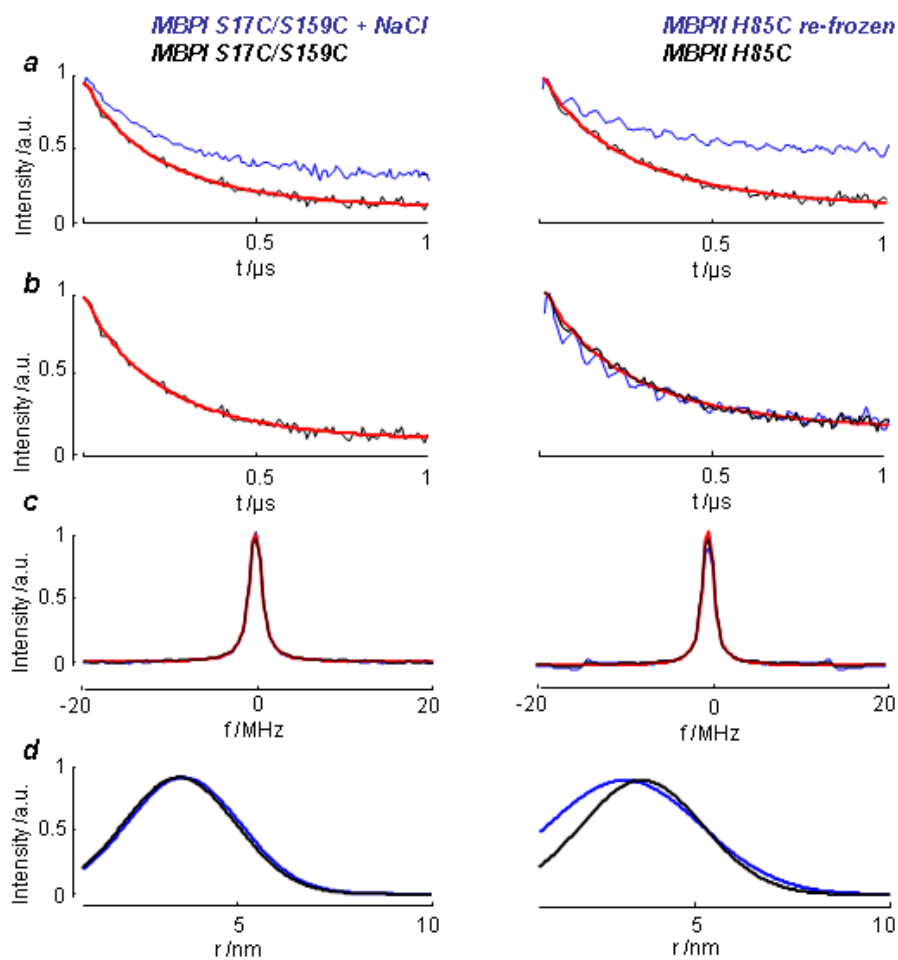


Fig. 3.33. DEER data obtained for measurements with MBPI S17C with and without NaCl (~500 mM, left column) and MBPII H85C which has been thawed and re-frozen (right column) at 50 K. **a:** background corrected time data. **b:** background corrected time data with modulation depth scaling. **c:** Fourier transformed dipolar spectra with simulations for Gaussian distance distributions. **d:** Gaussian distance distributions obtained for simulation of the dipolar spectra. Despite the effect of significantly reduced modulation depth for MBP with NaCl and re-frozen MBP no significant differences with respect to the reference measurements of MBP without NaCl and the standard MBPII H85C sample, respectively, are observed.

4. Discussion

4.1 MBP in Solution: Evidence of aggregation of individual MBP molecules

4.1.1 The interaction of Cu²⁺ and MBP

The interaction of MBP and a characteristic selection of divalent metal ions results in a number of biologically relevant effects. The most important effects are observed when MBP interacts with Zn²⁺ or Cu²⁺ ions. Under physiological conditions the Zn²⁺ concentration within the cytoplasm of standard myelin tissue, for example, reaches remarkably high values of about 50 μM. Findings like this led to the assumption that there is a myelin-stabilizing effect induced by interaction of MBP and Zn²⁺. Cu²⁺ is also taken up by myelin membranes, and from results based on calorimetric measurements and equilibrium dialysis, it is known that the uptake of Cu²⁺ by MBP takes place even on a higher level than for Zn²⁺. Additionally, several other effects based on MBP and Zn²⁺ together with phosphate are known, which include: *i*) the formation of cryptic aggregates as studied by light scattering or *ii*) fluorescence studies, in which a significant quenching of the fluorescence intensity of the single tryptophan residue contained in the MBP (residue number 113) was observed by interaction with Cu²⁺ and a blue shift for interaction with Zn²⁺. Further, there are direct hints for a zinc binding site (residues 23-26: His-Ala-Arg-His) within the MBP sequence. Together with the information that MBP is able to bind two copper ions in one molecule and the fact that the sequence includes several additional histidines, it was one aim of this study to shed light on the interaction of MBP and divalent metal ions.

In this respect it was of greatest advantage that Cu²⁺ is EPR active. In an axially symmetric coordinated copper, which from the CW EPR spectra is clearly found here, the singly occupied molecular orbital (SOMO, the molecular orbital occupied by the unpaired electron) is the $d_{x^2-y^2}$ orbital within the square planar x- y-plane, which allows for a significant overlap with ligand orbitals. Therefore, Cu²⁺ represents an intrinsic spin probe to study the interaction of MBP and divalent metal cations. Standard CW EPR and also pulse EPR measurements were hence regarded as a promising tool to gain more information about e.g. binding conditions, the number of potential binding sites, interacting amino acid residues and the effect of the Cu²⁺ uptake by MBP on the structure of the protein.

The experimental conditions selected here enabled to study the hyperfine couplings of the electron spin with nuclear spins like e.g. ¹H(I=1/2), ¹⁴N(I=1), ³¹P(I=1/2), ²³Na(I=3/2) of directly

coordinated ligands or nuclei within the immediate environment. This, in turn, allows the assignment of couplings to potential coordination partners of Cu^{2+} within the protein. Due to the characteristic effects of phosphate on MBP interaction with divalent metal ions, phosphate buffer (pH 7.4) has been selected as the optimum buffer solution. Phosphate, unlike TRIS, has no intrinsic nitrogen atoms, which could be coordinated to the central Cu^{2+} ion as well and such hamper interpretation.

Characterization of Cu^{2+} binding sites by CW EPR

Standard CW EPR measurements were performed in phosphate buffer at 77 K for molar ratios of MBP C1 (the least modified charge isomer of MBP) and Cu^{2+} of 2:1, 1:1, 1:2, 1:3, 1:4, and 1:5 (Fig. 3.3). At first glance, it becomes obvious that each single spectrum is comprised of more than one spectral component. For each measured MBP/ Cu^{2+} ratio the measured spectra clearly **consist of different fractions of Cu^{2+} species**, which significantly differ in their characteristic EPR parameters (g - and A -tensor values). This can be seen most clearly in the g_{\parallel} region of the spectra (Table 3.1). Simulation of the data revealed that two species of copper (species I and II) dominate the CW spectrum for a molar ratio of 2:1, which only slightly differ in g_{\perp} (2.041 vs. 2.043) and A_{\perp} (27 vs. 27 MHz), but feature significant differences for g_{\parallel} (2.211 vs. 2.253) and A_{\parallel} (575 vs. 550 MHz). Additionally, the g -values of both species are significantly lower and values for hyperfine coupling significantly higher than literature values for free Cu^{2+} dissolved in water and the reference measurements in buffer without MBP ($g_{\perp} = 2.053$, $g_{\parallel} = 2.39$, $A_{\perp} = 13$ MHz, $A_{\parallel} = 410$ MHz), which implicates that Cu^{2+} species I and II share EPR features, which significantly differ from those of free copper ions (species IV). The higher g -values and the lower hyperfine coupling constants for free copper are caused by high contributions of spin orbit coupling due to larger spin population at the central ion and due to larger spin-orbit contributions with oxygen-orbitals of water (the ligand in this case). In the 2:1, sample species I amounts to 60% of the total Cu^{2+} within the sample. The CW spectrum also reveals additional characteristic couplings of about 50 MHz in the g_{\perp} region of the CW EPR spectrum for a protein to copper ratio of 2:1, which is a clear indication of hyperfine couplings between the free electron of the copper and coordinated nitrogen nuclei. This implicates that at least one of the copper species I and II is directly coordinated to MBP, the only source for nitrogen-based ligands in the samples. With increasing copper content the relative intensity of species II steadily increases up to ~65% for molar ratios of 1:2 and 1:3. The maximum intensities of the nitrogen-based splitting pattern were also reached for molar ratios of 1:2 to 1:3. Simulations of CW EPR spectra with molar ratios of MBP and copper of 1:3, 1:4, and 1:5 deliver a slight re-increase in intensity of the fraction of copper species I with respect to the total copper amount within the samples (~22% for a ratio of

1:5). At ratios of 1:4 and 1:5 a significant part of the spectrum is represented by free copper (2% and 20%, respectively). A fourth species of copper (species III, $g_{\perp} = 2.045$, $g_{\parallel} = 2.26$, $A_{\perp} = 27$ MHz, $A_{\parallel} = 560$ MHz), has to be introduced to obtain the good fits shown in Fig. 3.4, which is similar to species II and could be attributed to copper, which is coordinated more loosely in peripheral regions between MBP molecules.

Evidence for Cu²⁺-assisted MBP aggregation

Based on the simulation parameters of species I, II, and III, their intensities, the characteristic nitrogen coupling discovered in the spectra together with the results of DEER distance data the different species may be characterized in more detail. Simulation parameters are in good agreement with the assumption that at a ratio of MBP and Cu²⁺ of 2:1 we detect, first, Cu²⁺ bound to single MBP molecules (species I) and, second, Cu²⁺ bound to the same MBP molecule but at a different, the second, binding site (species II). This is also supported by equilibrium dialysis experiments, which strongly indicate a positive cooperativity for the two binding sites ($K=0.083$ μM^{-1} , $n=1.8$). The almost equal appearance of two bound copper species upon addition of MBP can be interpreted such that even at an excess of MBP the two binding sites in the same MBP molecules are saturated with Cu²⁺ and that only a minor fraction (hence the slight excess of species I vs. species II) has *only* the first binding site filled. Results from DEER measurements show maximum modulation depths (and thus maximum number of interacting electron spins) for the ratios of 1:3 and 1:4 and the dominating Cu²⁺ species (in CW EPR) for these ratios is clearly represented by species III. This can be interpreted in two ways: *i*) either the third type of Cu²⁺ is loosely attached to the outside of single MBP molecules or *ii*) the formation of MBP aggregates. Closer inspection of the \mathbf{g} and hyperfine coupling tensor of species III clearly favors the interpretation that species III is representative for Cu²⁺ ions coordinated to aggregated MBP molecules with both intrinsic binding sites saturated. The spectral features within the g_{\perp} region of the spectrum - only referred to as nitrogen couplings so far - are very similar to those of species II. Simulations revealed that four nitrogen atoms are also included in the copper coordination sphere of species III, which is not only reflected by the characteristic couplings of about 37 MHz in the g_{xx} and g_{yy} region of the CW EPR spectrum. If this third species originated from a loosely bound Cu²⁺, one would expect that either one of the nitrogen coordinations were significantly different from those of species one or two or even that one of the six ligands were replaced by water. This would lead to at least one of the \mathbf{g} or \mathbf{A} tensor elements being much closer to the value of copper without MBP, which is clearly not the case. Since this species basically only occurs at MBP/Cu²⁺ ratios of 1:3 and higher, these findings agree with the picture that species III is indicative of aggregate formation.

A schematic picture of the MBP-Cu²⁺ interaction derived from the results is given below (Fig. 4.1). For low concentrations of copper within the sample, isolated (and potentially also aggregated) MBP molecules are present which may or may not have Cu²⁺ coordinated. Cu²⁺ ions bound to MBP are detected as species I (red, first binding site) and as species II (light green, second binding site). Due to positive cooperativity there are (almost) always two ions bound to one MBP molecule. With increasing copper concentrations more and more Cu²⁺ ions bound to “filled”, possibly aggregated MBP molecules are detected (increasing modulation depth in DEER measurements) but at an MBP/Cu²⁺ ratio of 1:2 the maximum modulation depth is not yet reached. This only happens when even more Cu²⁺ is added to the sample. A number of about 3-4 Cu²⁺ ions is necessary to observe maximum modulation depth, which directly indicates, that the additional Cu²⁺ somehow leads to increased interaction/aggregation or stabilization of MBP molecules and a third species of bound copper was needed for optimum CW EPR simulation (species III, dark green).

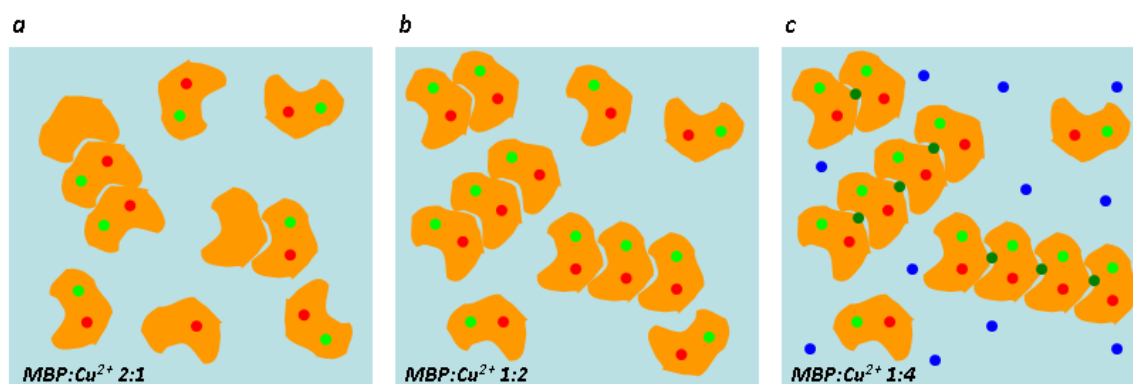


Fig. 4.1. Schematic picture for the interaction of MBP and Cu²⁺. **a:** For a molar ratio of MBP/Cu²⁺ of 2:1 there are may be both isolated and aggregated MBP molecules within the sample. Only a fraction of the molecules is coordinated by copper ions. Cu²⁺ bound to the first binding site is shown in red (species I), Cu²⁺ which is bound to the second binding site is shown in light green (species II). According to the positive cooperativity it is most likely that the uptake of one Cu²⁺ results in the uptake of a second Cu²⁺ within one molecule **b:** With increasing copper concentration and the occupation of all free binding sites, the DEER modulation depth increases. **c:** With even more copper (molar ratios of about 1:4), an additional species of coordinated copper is observed (species III, shown in dark green), which leads to significantly increased levels of MBP aggregation (indicated by maximum modulation depth in DEER measurements). Additionally, a fraction of non-bound Cu²⁺ is observed (species IV).

Additional support for this picture comes from T_2 relaxation measurements, which yield shortest T_2 times for the ratios 1:3 or 1:4 (representative for a higher level of molecular interaction, Table 3.2). Increasing T_2 values for the MBP/Cu²⁺ ratio 1:5 are a clear indication of increased amounts of free copper in the sample with less chemical interaction to the direct ligands and the molecular vicinity. As the measured value of T_2 is an ensemble value of all electron spins in the sample, with more free Cu²⁺ it approaches the even higher T_2 values of the reference sample.

The outer ligand sphere of the Cu²⁺ binding sites

At this point, the HYSORE experiments with the same samples in phosphate buffer (Fig. 3.9) may now give a more detailed view on the ligand sphere of bound copper ions. Here, the 2D spectra revealed cross peaks at (3.1, 4.2) and (4.2, 3.1) MHz. Several studies that have dealt with Cu²⁺ binding to proteins have shown that such couplings originate from hyperfine couplings with surrounding, non-coordinating backbone amides with $a_{\text{iso}}(^{14}\text{N}_{\text{am}}) \approx 1$ MHz.⁵⁹⁻⁶⁰ These peaks reach their maximum intensity for a ratio of 1:4. One can thus conclude that the dominant Cu²⁺ species at this ratio (species III) most likely features slightly more couplings to backbone amides than species I and II. Additional couplings are observed at (1.6, 4.0) and (4.0, 1.6) MHz, which are characteristic for double quantum ($|\Delta m| = 2$) transitions $\nu_{\alpha}^{\text{dq}}, \nu_{\beta}^{\text{dq}}$ of distal imidazole ¹⁴N_δ nuclei from coordinated histidine (His) side chains.⁵⁹⁻⁶⁰ These couplings are well resolved for all MBP/Cu²⁺ ratios, but are diminished in intensity for the measurements along the molecular z-direction and at low copper content. This situation could be explained by the following assumptions: First, histidines play an important role (*i.e.* at least but likely more than one of the nitrogen-based ligands is a histidine imidazole) in the coordination for all detected Cu²⁺ species and, second, there seems to be a slight orientation selection for the Cu²⁺ coupled to the imidazole nitrogen at low copper concentrations. *i.e.* they are slightly preferred as ligands in the molecular xy plane. This situation changes with molar ratios of 1:2 and 1:3. Here the couplings within z orientation seem to be on an equal level to the ones in xy orientation, again indicating an additional binding site.

The dimension of MBP aggregates

Additional information about the possible dimensions of the MBP aggregates was accessible by simulation of the dipolar spectra obtained from DEER measurements (Fig. 3.12, 3.13). Here, a characteristic distance distribution around about 3 (± 0.2) nm is predominant in all samples. Only for higher copper contents (MBP/Cu²⁺ ratios of 1:4 and 1:5) additional shorter distances are observed in the dipolar data (Fig. 3.14). These distances could be correlated with new, shorter distances originated by species III, appearing at high copper concentrations. The fact that the dipolar spectra, besides these new frequencies indicative of shorter distances, are similar to those at smaller MBP/Cu²⁺ ratios implicates that the coordination of Cu²⁺ species III takes place in an approximately fixed orientation and distance of the coordinated Cu²⁺ species I and II in the MBP molecules. The binding of the third species of copper that probably supports the aggregation of MBP molecules apparently does not induce changes in the MBP molecules that would lead to alterations of distance and orientation of the first two bound copper ions. The

appearance of the slightly shorter distances together with the appearance of species III allows the conclusion that the binding site of this third Cu^{2+} ion in the aggregates is at most 3 nm from the two binding sites in the individual MBP molecules, which hence gives a size estimate of individual MBP molecules. This also means that species III is situated between two aggregated MBP molecules.

The role of the buffer on MBP aggregation

In general, also the phosphate groups, or rather the absence of other nitrogen-based ligands, are present in the interplay of MBP and Cu^{2+} . CW and ESE EPR measurements with MBP and Cu^{2+} in TRIS buffer (molar ratio 1:3) revealed only slight differences when compared with the reference sample without MBP. This clearly indicates less overall interactions of Cu^{2+} with MBP in TRIS buffer compared to the measurements in phosphate buffer (Fig. 3.15). This is also reflected by the modulation depths of the DEER measurements, which are significantly lower than those of the measurements in phosphate buffer. On the other hand, resulting distance distributions are independent of the buffer choice (Fig. 3.15). Thus, MBP seems to self-aggregate into structures of comparable shape also within TRIS buffer together with Cu^{2+} and even without phosphate, but the resulting MBP aggregation seems to take place on a much lower level. As described before, TRIS buffer with its intrinsic nitrogen atoms apparently is a competitive ligand for Cu^{2+} , reducing the number of MBP-based ligands for Cu^{2+} .

Cu^{2+} DEER orientation selection

DEER measurements, which were performed with MBP and copper ions (MBP/ Cu^{2+} ratio 1:1) in order to study possible orientation selection for Cu^{2+} DEER reveal only small differences for the detected dipolar data (Fig. 3.10, 3.11). A tendency towards slightly increased dipolar signal intensity for the relevant frequencies around -10 to -1 and 1 to 10 MHz for measurements in the g_{\perp} region can be correlated to the overall detection of a higher number of spins with xy orientation (when compared to those detected along the z orientation).

The lack of a defined orientation selection of the dipolar interaction is a clear indication that the two copper binding sites do not have a fixed orientation towards each other. This is conclusive evidence that there is a large degree of conformational freedom of the MBP backbone in solution to sample almost the complete orientation space, which in turn means that while there is a rather defined distance between the two sites (~3 nm), the orientation of the binding sites is more or less random. From the DEER data we cannot derive the exact shape of the individual MBP

molecules in solution, but the remarkably stable and rather well-defined distance between the two binding sites indicates that there is preferred conformation in solution.

4.1.2 Spin-labeled MBP in solution: MBP aggregation even without Cu^{2+}

To test whether MBP even aggregates in pure solution conditions, DEER measurements with spin labeled MBP in standard preparation buffer (20 mM Hepes-NaOH (pH 7.4) and 10 mM NaCl) were performed (Fig. 3.19). Here, again, a characteristic distance of about 3 nm is observed, even in solution and without Cu^{2+} or phosphate. Dilution of the spin labeled MBP with non-labeled MBP CI results in a decreased DEER modulation depth and a decreased detection of the 3.0 nm distance, which clearly indicates that the observed distance is a significant distance between individual MBP molecules.

Further hints for MBP aggregation stem from Instantaneous Diffusion measurements of nitroxide spin-labeled MBP without Cu^{2+} (Table 3.4). For the solutions/dilutions of spin labeled MBP together with unlabeled MBP CI, the 'local' concentration of spins is increased by factors of about 5 for the pure, undiluted sample, about 3.6 for the 1:1 diluted sample, and 2 in case of a 1:3-dilution, where no significant MBP aggregation was detected by DEER measurements (here accurate values for the physical concentration of spins were accessible). A factor of about two is within the experimental error for the estimation of 'local' spin concentration by Instantaneous Diffusion. Nevertheless, a remaining factor of about 2.5 between 'local' concentration of spin labels and the real, physical concentration is most obviously indicative of a significant MBP aggregation in the standard sample buffer.

4.2 Structure determination of spin labeled MBP in artificial membrane vesicles

Previous knowledge of MBP in membranes

MBP represents an intrinsically unstructured, peripheral membrane protein. With standard methods for structure determination of proteins only fragmentary information about MBP structure could be obtained. Part of this data is based on methods such as electron microscopy and light scattering, which only feature characteristic resolutions of about several nanometers or need a intermediate to long-ranged order and only allow specifying the general dimensions of MBP or aggregates of MBP. In studies using enhanced transmission electron microscopy (TEM) methods hollow cylindrical shapes formed from MBP were found (inner radius: 3nm, outer radius: 5.5 nm, height: 4.7 nm, Fig. 1.6, **c**). In this study, it is not exactly clear whether single MBP molecules,

dimeric structures, or aggregates of MBP were observed. Studies of hexahistidine-tagged MBP on artificial model membranes as studied by TEM revealed aggregates with a diameter of about 3 - 4 nm and potential, multilamellar arrangements featuring characteristic 4.8 nm repeats (Fig. 1.6, **b**). Information about intramolecular, structural characteristics was obtained by solution NMR proposing several helical regions in the dissolved MBP (Fig. 1.7). Only one of these helical regions has been confirmed by EPR studies of MBP associated to artificial model membranes. Efforts in order to form stable and pure MBP crystals for structure determination based on crystallography have not been successful, and led to the fact that MBP was entitled “uncrystallisable”.

EPR spectroscopy reveals structure and supramolecular assemblies of MBP in membranes

Due to the lack of experimental methods for the characterization of unstructured or only partly structured macromolecular systems, pulse EPR spectroscopy, probing the *local* environment, may give further insight into MBP structure or possible interactions of MBP molecules. In order to establish sample conditions with a maximum analogy to the physiological conditions, where MBP is attached to the outer part of the myelin membranes, MBP samples were prepared together with artificial membrane vesicles. The composition of these artificial membranes was chosen such that it mimics the composition of characteristic lipids in myelin at physiological conditions. Based on these sample conditions a selection of three individually spin-labeled MBP samples was used in order to gain further structural information by standard CW and pulse EPR experiments. One preparation of MBP was spin-labeled near the N-terminus at position 17 (referred to as S17C), one within the only clearly assignable helical structure at position 85 (H85C) and a third one at position 159 in the C-terminal region of the protein (S159C). Additionally, a mixture of the proteins labeled at position 17 and of proteins labeled at position 159 was used for measurements.

This sample set was selected in order to obtain an experimental system which delivers very characteristic EPR data for a broad spectrum of scenarios for possible MBP structures and supramolecular assemblies (Fig. 4.2). The only (so far understood) function of MBP in the myelin sheath is the stabilization of the sheath by connecting individual membranes. Hence, the results presented in Chapter 3 are in the following interpreted in light of these possible functional scenarios and the most likely scenario(s) will be discussed in detail.

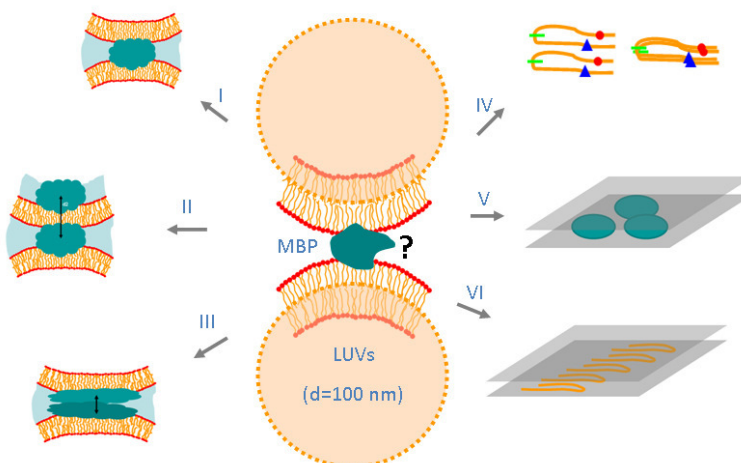


Fig. 4.2. A small collection of possible MBP structures and supramolecular assemblies formed from MBP.

Scenario I - No MBP aggregation: In this case we should not be able to detect any distance by DEER measurements at all (Fig. 4.3). Addition of NaCl and thawing/freezing of the sample, as also performed in this study, should not lead to significant changes detected by EPR measurements. This scenario is clearly at variance with our results.

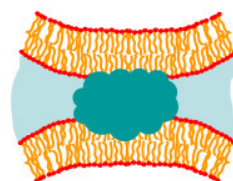


Fig. 4.3. Isolated MBP bridging two membranes

Scenario II - No MBP aggregation but molecules are located on opposing sides of the artificial membranes: In this case we should be able to detect a specific distance distribution by DEER experiments (Fig. 4.4).

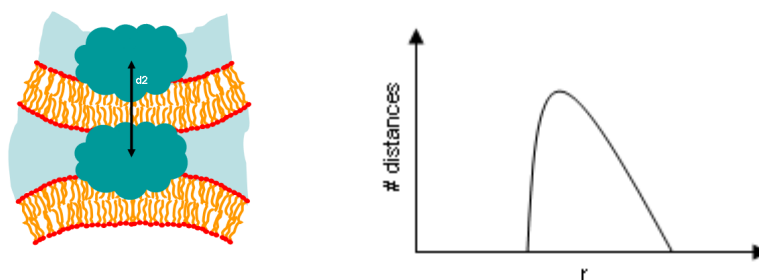


Fig. 4.4. Isolated MBP molecules on opposing sides of one membrane and theoretic distance distribution.

In this distance distribution, we should observe an intensity maximum at a well defined minimum distance where the two MBPs are positioned precisely adjacent to each other with respect to the neighboring membranes. This situation is illustrated in the picture describing scenario II on the left hand side of Fig. 4.4. Any variation from this orientation results in greater distances between the MBPs, which are represented in the long tail towards larger distances depicted in Fig. 4.4 (right hand side) and increase until the experimental limits are reached (in our case this would be at about 5.5 nm) and the intensity of the distance distribution vanishes. Modifications of the artificial membranes with regard to its thickness should lead to a shift of the maximum position in the distance distribution. This was investigated in this study by changing the composition of the membrane and preparing MBP in MLVs of increased membrane thickness. In these samples (MBP III) a significant shift of the maximum peak position towards larger distances should be observable. This was clearly not the case, as can be seen by comparing the DEER results in LUVs (thinner membranes) and MLVs (thicker membranes).

In addition, variations of the lipid-to-protein-ratio (LPR) should lead to different dipolar couplings and distance distributions. This was checked by measuring two sets of otherwise identical sets of MBP samples, namely MBPI (LPR 376:1) and MBPII (LPR 567:1). Less spin labeled protein should result in less detectable distances for isolated conditions, which again was not observed. Finally, addition of NaCl could possibly lead to a release of MBP bound to the membrane. Thawing and freezing of the sample should not lead to significant changes detected by EPR measurements.

Scenario III - dimerization of MBP (dimers of stretched MBP molecules): In this case we should be able to detect a characteristic set of dipolar couplings and the according distances for each labeling position (Fig. 4.5), depending on parallel (black arrows) or anti-parallel orientation (red arrows) of the monomers. Distance data should not be sensitive towards a modification of membrane thickness but should change with the LPR.

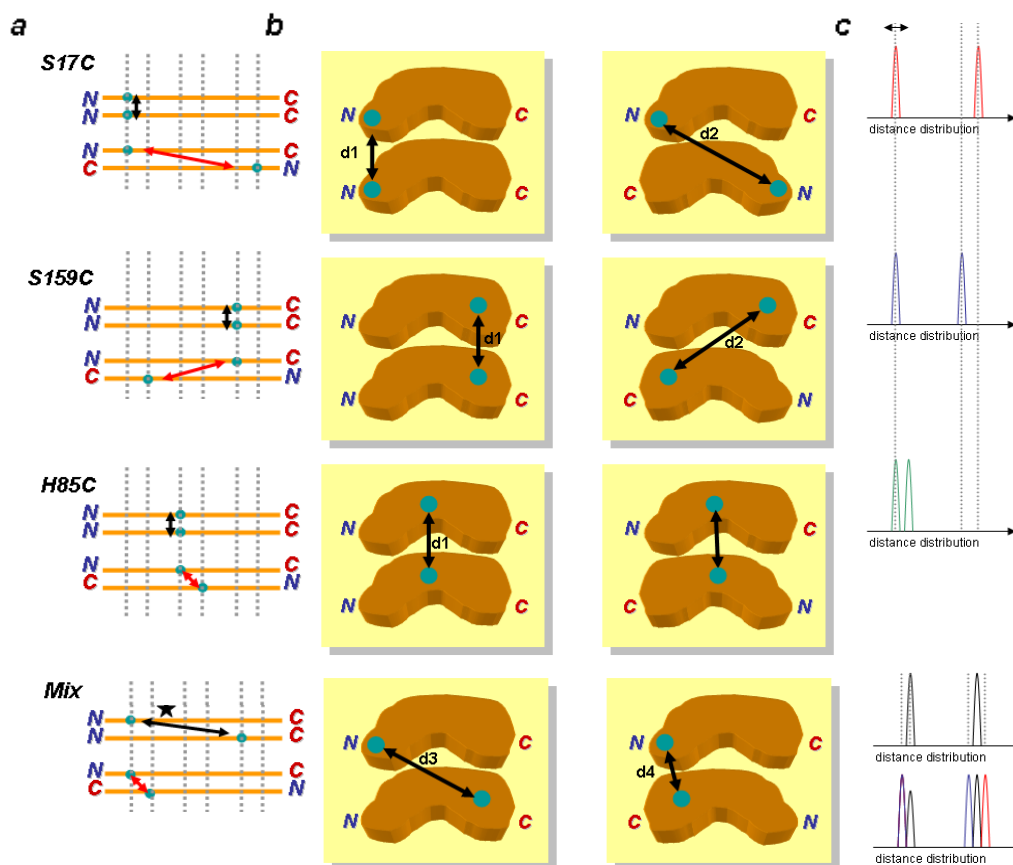


Fig. 4.5. Dimers of stretched MBP monomers: **a**: Draft of MBP dimers and distances observed for parallel (black) or anti-parallel alignment of the monomers (red). **b**: Different scheme of possible MBP interaction. **c**: Resulting distance distributions. For the mix sample only the new combination of labeling sites is shown.

Obviously, the detection of almost identical dipolar spectra as in this study is not in agreement with this scenario.

Following scenarios are not *per se* at variance with the experimentally obtained data:

Scenario IV - dimerization of MBP (dimers of stretched MBP hairpins): In this case we have to distinguish two general cases: In the first case, monomers are associated along the long side of the molecules. For parallel interaction, DEER measurements would result in one relatively narrow distance distribution for all labeling positions ($\sim 2 - 3.5$ nm, Fig. 4.6, **a**). Antiparallel interaction would result in individual distance distributions for all labeling positions (Fig. 4.6, **b**). In a second case, monomers are dimerized along the small side of the monomers (Fig. 4.6, **c**). Here, DEER measurements would result in distance data of about 3 - 6 nm (upper case) or a characteristic distribution for each labeling position (lower case). In general, distance data should,

again, not be sensitive to modification of membrane thickness but reveal sensitivity towards changes of the LPR. There would be no further specifications for results stemming from the other EPR measurements.

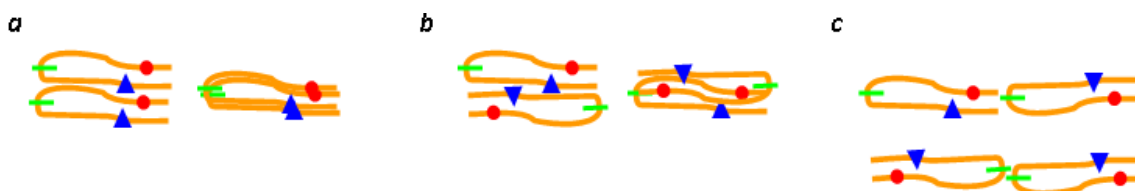


Fig. 4.6. Dimers of hairpin like MBP monomers: **a**: Dimers with parallel alignment interacting along the long side. **b**: Dimers with antiparallel alignment interacting along the long side. **c**: Dimers interaction along the short side. Legend: red circles: labeling position 17; green bars: labeling position 85; blue triangles: labeling position 159.

The following scenarios focus on the aggregation of individual MBP molecules of different shape:

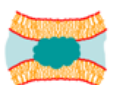
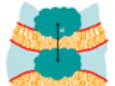
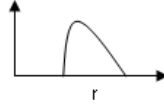



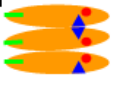
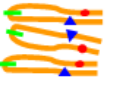
Scenario V - aggregation of globular MBP molecules: Here, all DEER measurements should reveal a relatively broad distance distribution with a maximum at about 4-5 nm. There would be no further specifications for results stemming from the other EPR measurements.

Scenario VI - aggregation of hairpin-like MBP monomers: This would finally lead to the same properties explained for the dimerization model of hairpins. For the aggregation of the more cigar-like MBPs along the long side of the molecules and parallel orientation, DEER measurements would result in one relatively narrow distance distribution for all labeling positions (~ 2 -3.5 nm). Antiparallel alignment should result in characteristic, though rather broad, distance distributions for the different labeling positions (most likely larger than 3.5 nm). In the second case, the hairpin like monomers aggregate to rows along the short side of the molecules. Here a distance distribution of about 4 - 6 nm should be predominant. Again, there would be no further specifications for results stemming from the other EPR measurements.

In particular the validity of the latter three scenarios can be tested by comparing the expected DEER data with the experimentally obtained results (for summary see Table 4.1).

Discussion

Table 4.1. Possible scenarios for structure and supramolecular assemblies of MBP and the characteristic features which should be observed.

	<i>interaction type</i>	<i>detection of distances?</i>	<i>sensitive to membrane diameter?</i>	<i>sensitive to LPR?</i>	<i>characteristic distance distribution?</i>
I	 <i>no aggregation</i>	no	no	no	no
II	 <i>no aggregation but intra-membrane distances</i>	yes	yes	yes	
III	 <i>dimers</i>	yes	no	yes	<i>individual distances for each labeling position</i>
IV	 <i>dimers</i>	yes	no	yes	<i>only one dominating distance</i>
V	 <i>interacting globular MBPs</i>	yes	no	yes	<i>only one broad distance distribution</i>
VI	 <i>interacting cigar-like MBPs</i>	yes	no	yes	<i>one rather narrow distance distribution</i>
	 <i>interacting cigar-like MBPs</i>	yes	no	yes	<i>one rather narrow distance distribution</i>

First, the general detection of distances of about 3 (± 0.2) nm in all MBP samples strengthens the assumption that MBP molecules do aggregate in artificial membrane vesicles. Note that a similar aggregation was observed in phosphate buffer and together with Cu^{2+} . As described above already, the interaction of isolated MBP within two artificial membranes is not supported by the experimental data (scenario I).

Also the picture that MBP molecules could be attached on opposing sides of one membrane (scenario II), can be regarded as rather unlikely, since measurements performed with vesicles featuring significantly larger membrane diameters (MLV) lead to the same results as measurements performed with membrane vesicles with smaller membrane diameters (2.55 nm vs. 2.8 nm, Fig. 3.30, 3.31).

The characteristic distance distributions assumed for dimers of parallel or antiparallel alignments of stretched MBP monomers are obviously not observed here, either (scenario III).

The scenario implementing dimerization of hairpin shaped monomers is only plausible for parallel interaction along the long sides of the molecules (anti-parallel orientation would lead to specific, broad distance distributions for each labeling position) or interaction along the short side (upper model in Fig. 4.6, **c**), which would most obviously result in distances larger than the detected ~ 3 nm.

The remaining scenarios all describe aggregation of MBP molecules of differing, individual shape. For aggregation of globular MBP molecules a broad distribution is expected. Since the obtained data reflect rather narrow or at least medium widths of distance distributions it is most likely that individual MBP molecules are not globular but rather feature a characteristic, less symmetric shape. The detected distances of about 3 nm would favor more cigar-like MBP monomers and a tendency of MBP interaction along the long side of the molecule (Fig. 4.7, **a**), since distances between spin labels interacting on the short side of the molecules would be significantly larger (theoretical length of stretched MBP: ~ 12 nm). The cigar-like shape of the monomer could be well realized by a hairpin structure (Fig. 4.7, **b**).

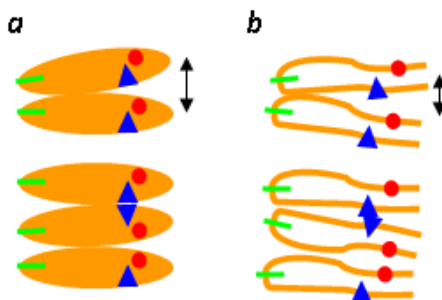


Fig. 4.7. Schematic picture for the interaction of MBP molecules as dimers or larger aggregates. **a**: Cigar-like MBP monomers interact along the long side of the molecules with a resulting distance distribution around about 3 nm. Flips around the long axis of the molecules do not influence the resulting statistical distribution around the 3 nm maximum due to averaging. **b**: Hairpin structure of the MBP monomers account for the cigar-like dimensions of the MBP molecules.

Regarding the question, whether MBP interacts with one or two membranes the overall dimension of the supramolecular aggregates favors MBP molecules interacting with two membranes at the same time (Fig. 4.8, **a**). A 3 nm distance, just for physiological conditions, would turn out to be too large for two molecules within the major dense line (only ~ 1.7 nm in diameter), when each of the molecules should be in contact with only one membrane (Fig. 4.8, **b**).

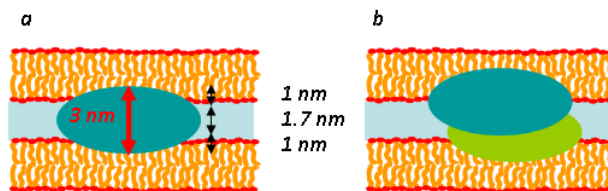


Fig. 4.8. Scheme of the interaction of MBP molecules and the artificial membranes with values for the physiological penetration depth of MBP and the distance between two myelin membranes (in black). **a:** Cigar-like MBP monomers with contact to two membranes at the same time **b:** Two interacting MBP molecules, where each of the MBP molecules interacts with only one membrane. Here most obviously deeper penetration into the membranes takes place, which is not in line with data stemming from physiological studies of MBP in myelin membranes.

Together with the results obtained by measurements with un-labeled MBP in phosphate buffer and Cu^{2+} , which indicated a significant aggregation of MBP molecules in solution, also results of spin labeled MBP with artificial membranes clearly indicates MBP aggregation.

Values detected for the 'local' concentration of spins were comparable within one sample set but decreased from about 2.9 mM for MBPI over 2.3 mM for MBPII to 1.6 mM for MBPIII and 1.4 mM for pure MBP IV in solution. With regard to the estimated physical concentration of spin labels (MBPI and II: 0.2 mM, MBPIII: 0.13 mM), the 'local' concentration is increased by a factor of about 10 for MBPI-III and by a factor of about 5 for MBP in solution.

4.3 Properties of the chemical vicinity of the spin labels within MBP

Additional EPR measurements were performed in order to study the chemical neighborhood of the spin-labels, which were attached to MBP. A first aim of these measurements was to rule out whether there are interactions between the spin labels in the close molecular neighborhood. Any greater differences in the chemical properties (hydrophobicity, polarity, etc.) of the neighborhood should finally lead to significant changes in the general shape of CW and ESE-detected EPR spectra for the different spin label positions, like e.g. changes of the hyperfine tensor element A_{zz} , which dominates the width of low-temperature EPR spectra. Another point of interest was to find out if there are any effects of spin-spin (electron spin vs. electron spin or electron spin vs. nuclear spin) interactions at short distances (*i.e.* up to 2 nm). Electron spin interactions should result in a significant line broadening of the characteristic ESE signal through dipolar couplings that depend strongly on the interspin distance ($V(r) \propto r^{-3}$).

Remarkably, CW and ESE EPR measurements resulted in very similar spectra for MBPI and MBPII at 20 and 50 K indicating no significant variations in the direct molecular neighborhood of the spins for the different labeling position (Fig. 3.23, 3.24). Only in the case of MBPI H85C one could assume line broadening at the flanks of the spectrum, indicating spin-spin interactions at

short distances. These results are not confirmed with MBP_{II}, where no significant line broadening could be observed. A final explanation for this single observed difference cannot be given here.

In general, a significant variation of spin-spin interaction should result in much greater variations of the EPR spectra. Since this was not observed here, short distances (up to 2 nm) between spin labels are either not present at all or very similar for all MBP samples. It can thus be safely concluded that in the aggregated MBP molecules that are labeled at three different sites not only the spin-label distances detectable with DEER, but also those short distances that are prominent in CW/ESE EPR are virtually identical in all samples.

In MBP in MLVs (MBP_{III}), $2A_{zz}$ was decreased significantly, which has the main origin in the different composition of the membrane lipids (Fig. 3.24). Possibly, the penetration depth of MBP molecules into the MLV membrane is significantly different from that in LUVs. The decrease of the z-hyperfine component indicates a strongly reduced polarity of the chemical environment in MLVs. Again, remarkably, the shift in $2A_{zz}$, when changing from LUVs to MLV, is identical for all labeling positions. Additional characterization of the chemical neighborhood of the spin labels was possible by the T_2 measurements. In general, values for the different labeling positions in one sample set (MBP I, MBP II, MBP_{III}) are similar: about 500 ns for MBP_I, 610 ns for MBP_{II}, and 800 ns for MBP_{III} (detected at maximum position of the ESE spectra, Table 3.5). There is a significant trend towards longer T_2 times for MBP_{II} and MBP_{III}, which is most likely caused by a decreased amount of MBP aggregates due to the reduced overall protein concentration: MBP_I: 0.2 mM at LPR 378:1; MBP_{II}: 0.2 mM at LPR 567:1; MBP_{III} ~0.13 mM at LPR 567:1). This assumption is also supported by data obtained from measurements with thawed and re-frozen MBP (Fig. 3.25). Here, again all experiments indicate a decreased number of aggregated MBP molecules and T_2 values are finally about 1.7 times higher than before the procedure.

Further characterization of the local surroundings of the spins was possible by results stemming from simulations of CW spectra detected at room temperature (Fig. 3.16, 3.21). Here, the most important information can be obtained by determination of the rotational correlation time τ , which is sensitive to the molecular dynamics of the spin label which is influenced by e.g. the site of spin-label attachment, the overall mobility of the side-chain and the local, effective viscosity/mass of the rotating side chain. Simulations reveal a significant difference of τ -values for MBP H85C in LUVs ($\tau=12.5$ ns) and in solution ($\tau=3$ ns). Since the solution-sample lacks the artificial membrane vesicles but is prepared with the same spin-labeled proteins as the LUV sample, this large change of molecular motion of the spin-label is a direct consequence of the strong interaction of the helical region with the membranes of the LUVs. The two other labeling sites, 17, 159, apparently do not interact with the membranes as strongly as the 85 position. An additional effect, due to a restricted molecular motion by the helix itself, results in an entirely different spectral shape of the MBP II H85C-sample as compared to the other sites. For the latter labeling

positions, τ -values of about 5 ns indicate that molecular motion is clearly less influenced by effects which restrict molecular motion of the spin label.

Further insights into the interaction of the electron spin of the spin labels and its chemical vicinity are accessible by ESEEM-based experiments. Specific interactions of the free electron spin and remote nuclei (like e.g. ^{14}N) can be detected by 3-pulse ESEEM measurements or HYSCORE. Results obtained from 3-pulse ESEEM measurements of MBP in artificial membrane vesicles (MBPIII) and (MBPII) reveal a significant fraction of couplings at about 2.2 MHz with maximum intensity for the H85C labeling position (Fig. 3.28). From HYSCORE experiments, one can conclude that there is one characteristic coupling to nitrogen at about 2.2 MHz for the H85C labeling position (Fig. 3.29). In general, for all labeling positions couplings at the Larmor frequency of ^{31}P are observed, most likely indicating interactions with lipid phosphates or phosphate buffer.

5. Conclusions and Outlook

Conclusion

In this work a wide variety of EPR techniques was used in order to study the structure of myelin basic protein (MBP) and of possible MBP aggregates as well as the interaction of MBP with divalent copper ions (Cu^{2+}). MBP (+19 net positive charge) has been reported to take up divalent metal ions (mainly Zn^{2+}), which has been shown to have a stabilizing effect on the myelin sheath. An efficient biological, myelin-based insulation around the axons of the central nervous system (CNS) and the peripheral nervous system (PNS) is indispensable for proper transmission of nervous signals. Any structural perturbations within the myelin sheath result in severe microbiological processes, which can even lead to the complete degradation of the myelin sheath and the nervous axons in the typical disease pattern of multiple sclerosis (MS). Cu^{2+} is also known for its specific interaction with MBP. The uptake of Cu^{2+} by MBP (quantified by equilibrium dialysis and calorimetric experiments) in the presence of phosphate was reported to promote formation of cryptic aggregates in solution, as studied by light scattering, and led to a quenching of the tryptophan fluorescence (residue 113) observed by fluorescence spectroscopy.

Based on these findings and the advantage that Cu^{2+} is EPR active, copper EPR measurements were performed, which substantially expanded the knowledge about MBP and Cu^{2+} interactions. Continuous wave (CW) EPR and electron spin echo (ESE-detected) EPR experiments with Cu^{2+} and non-spin-labeled MBP C1 (the least modified MBP isoform isolated from humans) in the presence of phosphate enabled to identify three species of MBP-bound copper, which were further characterized upon variation of the molar ratios of MBP/ Cu^{2+} . Results suggested the following interaction mechanism (Fig. 5.1).

Apparently, isolated MBP as well as aggregated MBP coexist within the sample solution. The addition of Cu^{2+} results in the occupation of a first Cu^{2+} binding site of MBP. Positive cooperativity (which was reported based on thermodynamic studies) results in population of a second Cu^{2+} -binding site in MBP when more Cu^{2+} is added. Even higher Cu^{2+} concentrations trigger a remarkable molecular self-assembly of MBP, Cu^{2+} , and phosphate, which was characterized by pulse EPR methods. Results from electron spin echo envelope modulation EPR measurements (ESEEM) and double electron electron resonance EPR experiments (DEER) strongly indicated a higher proportion of aggregated structures for an excess of 3 - 4 Cu^{2+} per one MBP, which is probably closely correlated to the appearance of Cu^{2+} that binds MBP (or possibly two MBPs at the same time) at an interface region and allows the formation of MBP aggregates.

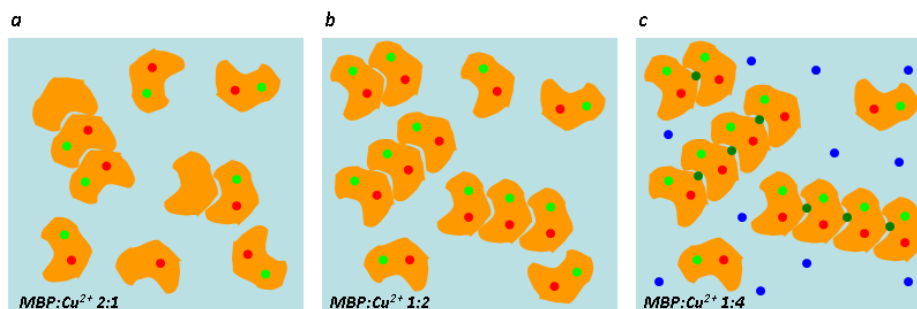


Fig. 5.1. Schematic picture for the interaction of MBP and Cu^{2+} . **a:** For a molar ratio of MBP/ Cu^{2+} of 2:1 there may be both, isolated and aggregated MBP molecules within the sample. Only a fraction of the molecules is coordinated by copper ions. Cu^{2+} bound to the first binding site is shown in red (species I), Cu^{2+} which is bound to the second binding site is shown in light green (species II). According to the positive cooperativity it is most likely that the uptake of one Cu^{2+} results in the uptake of a second Cu^{2+} within one molecule **b:** With increasing copper concentration and the occupation of all free binding sites, the DEER modulation depth increases. **c:** With even more copper (molar ratios of about 1:4), an additional species of coordinated copper is observed (species III, shown in dark green), which leads to significantly increased levels of MBP aggregation (indicated by maximum modulation depth in double electron electron resonance (DEER) measurements). Additionally, a fraction of non-bound Cu^{2+} is observed (species IV, shown in blue).

Important information about the ligand sphere of the MBP-bound Cu^{2+} ions was obtained. CW EPR measurements indicated a number of four directly coordinated ^{14}N nuclei for MBP-bound Cu^{2+} (likely correlated to Cu^{2+} that is bound to the first or the second binding site). With hyperfine sublevel correlation (HYSCORE) experiments it was possible to identify $^{14}\text{N}_\delta$ of imidazole side chains from histidines, suggesting the importance of histidines for Cu^{2+} coordination, and non-coordinating $^{14}\text{N}_{\text{am}}$ of backbone amides, both of which in the outer ligand sphere of the Cu^{2+} ions.

An estimation of the general dimensions of the observed MBP aggregates was enabled by double electron electron resonance (DEER) spectroscopy. With respect to the biological model system of MBP in the myelin membrane, this work is an entirely new approach to elucidate the structure of MBP or supra-molecular assemblies of MBP. This new approach is an expansion from the standard methods of structure determination like X-ray diffraction of 3D crystals, which delivered no structural information due to the lack of adequate 3D crystals. Even the related nuclear magnetic resonance (NMR) spectroscopy only yielded only partial insights such as the estimation of local mobility of the protein backbone within the MBP molecules. Since alternative methods like cryo electron microscopy already characterized particles and lamellae-like structures based on 2D crystals of MBP, it was one aim of this work to gain additional structure information of possible MBP aggregates by EPR spectroscopy. Due to an already well established procedure for MBP spin-labeling, which had e.g. been used to identify a characteristic helical structure in MBP (residues 82-93) with CW EPR methods, a set of previously investigated samples was accessible for pulse EPR spectroscopic studies. .

Conclusions and Outlook

Structural information was pursued with the detection of dipolar couplings and hence specific distances between the spin-labels on the MBP molecules. The selection of samples with the different spin-labeling positions allowed for identification and validation/falsification of different possibilities for MBP interaction. The experiments were performed with spin-labeled MBP in solution and spin-labeled MBP in artificial membrane vesicles mimicking the physiological microenvironment of MBP within the myelin sheath. In this context, a rather narrow or at least intermediately broad distance distribution of about 3 (± 0.2) nm was found for spin-labeled MBP in solution buffer, spin-labeled MBP in artificial membrane vesicles of different thickness as well as for non-spin-labeled MBP and Cu^{2+} . Thus, there is direct evidence for aggregation of MBP in general and self aggregation of MBP even in solution, *i.e.* without Cu^{2+} or phosphate, and in lipid bilayer membranes. The most plausible picture of MBP interaction derived from the observed dipolar/distance data and the EPR results in general is given in Fig. 5.2: Individual MBP molecules likely assume an anisotropic shape, which is neither globular nor stretched but which is “cigar”-like, possibly formed from a hairpin structure. One MBP interacts with two membranes at the same time and additionally with neighboring MBP molecules along the long side of the ellipsoid in order to form characteristic MBP aggregates.

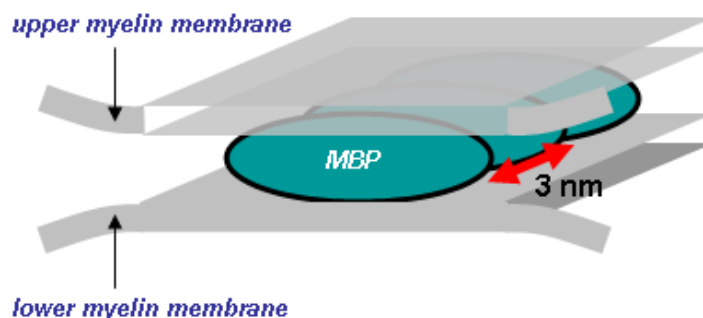


Fig. 5.2. Schematic picture of MBP interaction. The cigar-like MBP molecules simultaneously interact with the upper and lower lipid membrane. The interaction between the MBP molecules takes place along the long side of the molecules. DEER measurements show characteristic distances of about 3 nm between the aggregated MBP molecules, which does not significantly depend on the position of the spin-labels within the molecules. The cigar-shape could be the final result of the formation of a hairpin structure of MBP.

Additional support for MBP aggregation, in general, arises from 2-pulse ESEEM and instantaneous diffusion measurements, which clearly indicate an enhanced level of molecular interaction and ‘local’ spin density, as could be best seen for measurements including dilutions of spin-labeled MBP and unlabeled MBP. Clear hints for well structured MBP aggregates were also found by adding NaCl to the sample and a thawing and re-freezing procedure. The results indicate that the structure of the aggregates in general remained the same, while the overall amount of aggregated MBP decreased due to charge screening upon salt addition.

Conclusions and Outlook

Also, the properties of the chemical environment of the spin labels within MBP were studied with CW and ESE EPR measurements. In this context, the micro vicinity around the three different spin labeling positions share a remarkably high level of similarity according to hydrophobicity/polarity or spin-spin-interactions, which is perfectly in agreement with the MBP interaction model presented here. At low temperatures ($T < 107$ K) the EPR spectra are dominated by the chemical environment around the spin label, *i.e.* by the conformation and position of MBP in the membranes. At room temperature, also the molecular dynamics are present and influenced such as the reduced spin label mobility in the helix (for the labeling position within the helix, residues 82 - 93) is resolved and reflected in the molecular rotational correlation times gained from CW EPR measurements.

In conclusion, CW and pulse EPR experiments deliver new and remarkable insights into the important biological system of MBP and MBP in lipid bilayers. The methods performed here for the first time gave evidence for MBP aggregation and even gave information of local (supra-) molecular structure of MBP aggregates in solution and in lipid bilayer vesicles. This work is only a first step, describing the supra-molecular structure of MBP and the interaction of MBP with divalent metal ions in the case of the “healthy” charge isomer C1. A similar study on the charge-reduced isomers (like C8) may reveal differences between the healthy and MS case and finally may shed light on the question how these interactions are linked to molecular processes in neurodegenerative diseases like multiple sclerosis.

Outlook

Thus, CW EPR spectroscopy, and pulse EPR spectroscopy in particular, can be regarded as a very promising tool for future studies focusing on the effect of different charge states of MBP on the molecular conformation or the aggregated MBP. Since the charge of the MBP molecule determines the level of molecular interaction of the immuno-dominant epitope with the biological apparatus of the auto-immune system, DEER distance measurements allow for a charge-dependent insight into the assembly of MBP molecules.

In general, to obtain more information about the structure of MBP, it will be advantageous to apply site-directed spin-labeling (SDSL) to MBP mutants with two internal cysteinyl groups (double mutants). SDSL and DEER would then enable distance measurements between spin-labels within one MBP molecule. The selection of different labeling sites would finally allow for a rough 3D structure prediction of single MBP molecules.

An additional aim is to study pH effects on MBP aggregation. In this work, the pH was set to pH 7.4 throughout all measurements, mimicking physiological conditions. Evidence for a very

Conclusions and Outlook

sensitive interplay of pH and molecular interaction was reported from calorimetric measurements based on MBP and the uptake of divalent metal ions.

The stepwise degradation of the protein by exo-peptidase digestion could be another very interesting approach in order to determine the position of the Cu^{2+} binding sites within the protein. Such, it could be checked whether the reported Zn^{2+} binding site (residues 23 - 26) also serves as Cu^{2+} binding site. Additionally, the idea of a Cu^{2+} -mediated protein folding model with a final hairpin structure could be tested.

Another approach to detect the possible Cu^{2+} binding sites could be the selective introduction of isotopes into the MBP molecule (^{15}N labeled histidines, e.g.) for HYSCORE measurements, which could finally allow for rough determination of the Cu^{2+} binding sites within the protein.

Finally, DEER measurements with spin-labeled MBP and Cu^{2+} at the same time may allow measuring distances between the MBP-bound Cu^{2+} and the spin label (at the respective spin labeling position within the protein). Thus, also this approach could allow for a rough determination of the Cu^{2+} binding sites within the protein.

Appendix

A summary of the abbreviations of sample names which were used in this work is given below (Table. I).

Table I. Summary of abbreviations of sample names, which were used within this work.

<i>MBP</i>	<i>preparation</i>	<i>specification</i>	<i>abbreviation</i>
spin-labeled <i>rmMBPC1</i>	buffer+LUVs	LPR 378:1	MBPI
spin-labeled <i>rmMBPC1</i>	buffer+LUVs	LPR 567:1	MBPII
spin-labeled <i>rmMBPC1</i>	buffer+MLVs	LPR 567:1	MBPIII
spin-labeled <i>rmMBPC1</i>	buffer	-	MBPIV

· **List of Abbreviations and Symbols**

a.u. - arbitrary units

a_{iso} - isotropic hyperfine coupling constant

β_e - Bohr magneton

B - magnetic induction

CD - circular dichroism (spectroscopy)

CW - Continuous Wave

DEER - Double Electron Electron Resonance

EPR - Electron paramagnetic Resonance

ESE - Electron Spin Echo

ESEEM - Electron Spin Echo Envelope Modulation

FT - Fourier Transformation

MBP - Myelin Basic Protein

mM - $1 \cdot 10^{-3}$ mol/l

MTSSL - [1-oxyl-2,2,5,5-tetramethyl-D-pyrroline-3-methyl]methanethiosulfonat spin label

mw - microwave

nm - $1 \cdot 10^{-9}$ m

NMR - Nuclear Magnetic Resonance

Proxyl-IAA - Proxyl-3-(2-iodoacetamido)

ref. - reference

rm - recombinant murine

S17C - denotes a mutation of serin (residue number 17 within the protein sequence) to cysteine

SDSL - site directed spin labeling

τ - rotational correlation time

T - absolute temperature in Kelvin

TEM - Transmission Electron Microscopy

TRIS - tris(hydroxymethyl)aminomethane

X-band - microwave frequency range og ~9.1 GHz to ~9.8 GHz

References

1. Abrahams, J.P., et al., *STRUCTURE AT 2.8-ANGSTROM RESOLUTION OF F1-ATPASE FROM BOVINE HEART-MITOCHONDRIA*. Nature, 1994. **370**(6491): p. 621-628.
2. Sottocas.Gl, et al., *AN ELECTRON-TRANSPORT SYSTEM ASSOCIATED WITH OUTER MEMBRANE OF LIVER MITOCHONDRIA - A BIOCHEMICAL AND MORPHOLOGICAL STUDY*. Journal of Cell Biology, 1967. **32**(2): p. 415-&.
3. Wallin, E. and G. von Heijne, *Genome-wide analysis of integral membrane proteins from eubacterial, archaean, and eukaryotic organisms*. Protein Science, 1998. **7**(4): p. 1029-1038.
4. Wright, P.E. and H.J. Dyson, *Intrinsically unstructured proteins: Re-assessing the protein structure-function paradigm*. Journal of Molecular Biology, 1999. **293**(2): p. 321-331.
5. Plaxco, K.W. and M. Gross, *Cell biology - The importance of being unfolded*. Nature, 1997. **386**(6626): p. 657-&.
6. Romero, P., et al., *Thousands of proteins likely to have long disordered regions*. Pac Symp Biocomput, 1998: p. 437-48.
7. Dunker, A.K., et al., *Flexible nets - The roles of intrinsic disorder in protein interaction networks*. Febs Journal, 2005. **272**(20): p. 5129-5148.
8. Iakoucheva, L.M., et al., *The importance of intrinsic disorder for protein phosphorylation*. Nucleic Acids Research, 2004. **32**(3): p. 1037-1049.
9. Uversky, V.N., C.J. Oldfield, and A.K. Dunker, *Showing your ID: intrinsic disorder as an ID for recognition, regulation and cell signaling*. Journal of Molecular Recognition, 2005. **18**(5): p. 343-384.
10. Vucetic, S., et al., *Flavors of protein disorder*. Proteins-Structure Function and Genetics, 2003. **52**(4): p. 573-584.
11. Uversky, V.N. and A.L. Fink, *Conformational constraints for amyloid fibrillation: the importance of being unfolded*. Biochimica Et Biophysica Acta-Proteins and Proteomics, 2004. **1698**(2): p. 131-153.
12. Yee, A., et al., *An NMR approach to structural proteomics*. Proceedings of the National Academy of Sciences of the United States of America, 2002. **99**(4): p. 1825-1830.

References

13. Sedzik, J. and D.A. Kirschner, *IS MYELIN BASIC-PROTEIN CRYSTALLIZABLE*. *Neurochemical Research*, 1992. **17**(2): p. 157-166.
14. Arroyo, E.J. and S.S. Scherer, *On the molecular architecture of myelinated fibers*. *Histochemistry and Cell Biology*, 2000. **113**(1): p. 1-18.
15. Baumann, N. and D. Pham-Dinh, *Biology of oligodendrocyte and myelin in the mammalian central nervous system*. *Physiological Reviews*, 2001. **81**(2): p. 871-927.
16. Kramer, E.M., A. Schardt, and K.A. Nave, *Membrane traffic in myelinating oligodendrocytes*. *Microscopy Research and Technique*, 2001. **52**(6): p. 656-671.
17. Dangond, F., *Disorders of Myelin in the Central and Peripheral Nervous Systems*. Butterworth/Heinemann, Woburn, MA., 2002.
18. Moscarello, M.A., *Myelin basic protein, the "executive" molecule of the myelin membrane*. *Cell Biology and Pathology of Myelin*, 1997. **4**: p. 13-25.
19. Musse, A.A., J.M. Boggs, and G. Harauz, *Deimination of membrane-bound myelin basic protein in multiple sclerosis exposes an immunodominant epitope*. *Proceedings of the National Academy of Sciences of the United States of America*, 2006. **103**(12): p. 4422-4427.
20. Saboury, A.A., N. Sarri-Sarraf, and S. Saidian, *Thermodynamics of binding copper ion by myelin basic protein*. *Thermochimica Acta*, 2002. **381**(2): p. 147-151.
21. Riccio, P., et al., *SPECIFICITY OF ZINC-BINDING TO MYELIN BASIC-PROTEIN*. *Neurochemical Research*, 1995. **20**(9): p. 1107-1113.
22. Cavatorta, P., et al., *MYELIN BASIC-PROTEIN INTERACTION WITH ZINC AND PHOSPHATE - FLUORESCENCE STUDIES ON THE WATER-SOLUBLE FORM OF THE PROTEIN*. *Biophysical Journal*, 1994. **66**(4): p. 1174-1179.
23. Berlet, H.H., H. Bischoff, and F. Weinhardt, *DIVALENT METALS OF MYELIN AND THEIR DIFFERENTIAL BINDING BY MYELIN BASIC-PROTEIN OF BOVINE CENTRAL-NERVOUS-SYSTEM*. *Neuroscience Letters*, 1994. **179**(1-2): p. 75-78.
24. Harauz, G., et al., *Myelin basic protein - diverse conformational states of an intrinsically unstructured protein and its roles in myelin assembly and multiple sclerosis*. *Micron*, 2004. **35**(7): p. 503-542.

References

25. Harauz, G., N. Ishiyama, and I. Bates, *Analogous standard motifs in myelin basic protein and in MARCKS*. *Molecular and Cellular Biochemistry*, 2000. **209**(1-2): p. 155-163.
26. Beniac, D.R., et al., *Three-dimensional structure of myelin basic protein .I. Reconstruction via angular reconstitution of randomly oriented single particles*. *Journal of Biological Chemistry*, 1997. **272**(7): p. 4261-4268.
27. Shanshiashvili, L.V., et al., *Adhesion and clustering of charge isomers of myelin basic protein at model myelin membranes*. *Archives of Biochemistry and Biophysics*, 2003. **419**(2): p. 170-177.
28. Bax, A. and S. Grzesiek, *METHODOLOGICAL ADVANCES IN PROTEIN NMR*. *Accounts of Chemical Research*, 1993. **26**(4): p. 131-138.
29. Libich, D.S. and G. Harauz, *Backbone dynamics of the 18.5 kDa isoform of myelin basic protein reveals transient alpha-helices and a calmodulin-binding site*. *Biophysical Journal*, 2008. **94**(12): p. 4847-4866.
30. Libich, D.S. and G. Harauz, *Solution NMR and CD spectroscopy of an intrinsically disordered, peripheral membrane protein: evaluation of aqueous and membrane-mimetic solvent conditions for studying the conformational adaptability of the 18.5 kDa isoform of myelin basic protein (MBP)*. *European Biophysics Journal with Biophysics Letters*, 2008. **37**(6): p. 1015-1029.
31. Polverini, E., et al., *Binding of the proline-rich segment of myelin basic protein to SH3 domains: Spectroscopic, microarray, and Modeling studies of ligand conformation and effects of posttranslational modifications*. *Biochemistry*, 2008. **47**(1): p. 267-282.
32. Shoemaker, B.A., J.J. Portman, and P.G. Wolynes, *Speeding molecular recognition by using the folding funnel: The fly-casting mechanism*. *Proceedings of the National Academy of Sciences of the United States of America*, 2000. **97**(16): p. 8868-+.
33. Ward, J.J., et al., *Prediction and functional analysis of native disorder in proteins from the three kingdoms of life*. *Journal of Molecular Biology*, 2004. **337**(3): p. 635-645.
34. Boggs, J.M., *Myelin basic protein: a multifunctional protein*. *Cellular and Molecular Life Sciences*, 2006. **63**(17): p. 1945-1961.
35. Scherer, S.S. and E.J. Arroyo, *Recent progress on the molecular organization of myelinated axons*. *Journal of the Peripheral Nervous System*, 2002. **7**(1): p. 1-12.

References

36. Boullerne, A.I., et al., *Anti-S-nitrosocysteine antibodies are a predictive marker for demyelination in experimental autoimmune encephalomyelitis: Implications for multiple sclerosis*. Journal of Neuroscience, 2002. **22**(1): p. 123-132.
37. Deferra, F., et al., *ALTERNATIVE SPLICING ACCOUNTS FOR THE 4 FORMS OF MYELIN BASIC-PROTEIN*. Cell, 1985. **43**(3): p. 721-727.
38. Givogri, M.I., E.R. Bongarzone, and A.T. Campagnoni, *New insights on the biology of myelin basic protein gene: The neural-immune connection*. Journal of Neuroscience Research, 2000. **59**(2): p. 153-159.
39. Asipu, A. and G.E. Blair, *REGULATION OF MYELIN BASIC-PROTEIN GENE-TRANSCRIPTION IN GLIAL-CELLS*. Biochemical Society Transactions, 1991. **19**(2): p. S85-S85.
40. Hill, C.M., et al., *Effects of the osmolyte trimethylamine-N-oxide on conformation, self-association, and two-dimensional crystallization of myelin basic protein*. Journal of Structural Biology, 2002. **139**(1): p. 13-26.
41. Hill, C.M.D., et al., *Terminal deletion mutants of myelin basic protein: new insights into self-association and phospholipid interactions*. Micron, 2003. **34**(1): p. 25-37.
42. Dawson, R., et al., *The N-terminal domain of p53 is natively unfolded*. Journal of Molecular Biology, 2003. **332**(5): p. 1131-1141.
43. Bates, I.R., et al., *Membrane-anchoring and charge effects in the interaction of myelin basic protein with lipid bilayers studied by site-directed spin labeling*. Journal of Biological Chemistry, 2003. **278**(31): p. 29041-29047.
44. Kim, J.K., et al., *Multiple sclerosis - An important role for post-translational modifications of myelin basic protein in pathogenesis*. Molecular & Cellular Proteomics, 2003. **2**(7): p. 453-462.
45. Wood, D.D., et al., *Acute multiple sclerosis (Marburg type) is associated with developmentally immature myelin basic protein*. Annals of Neurology, 1996. **40**: p. 18-24.
46. Schweiger, A., Jeschke, G., *Principles of Pulse Electron Paramagnetic Resonance*. Oxford University Press, 2001.
47. Steinhoff, H.J., et al., *High-field EPR studies of the structure and conformational changes of site-directed spin labeled bacteriorhodopsin*. Biochimica Et Biophysica Acta-Bioenergetics, 2000. **1457**(3): p. 253-262.

References

48. Freed, J.H. and G.K. Fraenkel, *THEORY OF LINEWIDTHS IN ELECTRON SPIN RESONANCE SPECTRA*. Journal of Chemical Physics, 1963. **39**(2): p. 326-&.
49. Kivelson, D. and S. Lee, *THEORY OF ELECTRON-SPIN-RESONANCE PARALLEL-EDGE LINES OF SLOWLY TUMBLING MOLECULES*. Journal of Chemical Physics, 1982. **76**(12): p. 5746-5754.
50. Barnes, J.P., et al., *A multifrequency electron spin resonance study of T4 lysozyme dynamics*. Biophysical Journal, 1999. **76**(6): p. 3298-3306.
51. Dzuba, S.A., *Librational motion of guest spin probe molecules in glassy media*. Physics Letters A, 1996. **213**(1-2): p. 77-84.
52. Stoll, S. and A. Schweiger, *EasySpin, a comprehensive software package for spectral simulation and analysis in EPR*. Journal of Magnetic Resonance, 2006. **178**(1): p. 42-55.
53. Hinderberger, D., H.W. Spiess, and G. Jeschke, *Dynamics, site binding, and distribution of counterions in polyelectrolyte solutions studied by electron paramagnetic resonance spectroscopy*. Journal of Physical Chemistry B, 2004. **108**(12): p. 3698-3704.
54. Shlesinger, M.F. and E.W. Montroll, *ON THE WILLIAMS-WATTS FUNCTION OF DIELECTRIC-RELAXATION*. Proceedings of the National Academy of Sciences of the United States of America-Physical Sciences, 1984. **81**(4): p. 1280-1283.
55. Madi, Z.L., S. Van Doorslaer, and A. Schweiger, *Numerical simulation of one- and two-dimensional ESEEM experiments*. Journal of Magnetic Resonance, 2002. **154**(2): p. 181-191.
56. Jeschke, G., et al., *Dipolar spectroscopy and spin alignment in electron paramagnetic resonance*. Chemical Physics Letters, 2000. **331**(2-4): p. 243-252.
57. Pannier, M., et al., *Determination of ion cluster sizes and cluster-to-cluster distances in ionomers by four-pulse double electron electron resonance spectroscopy*. Macromolecules, 2000. **33**(21): p. 7812-7818.
58. Pannier, M., et al., *Dead-time free measurement of dipole-dipole interactions between electron spins*. Journal of Magnetic Resonance, 2000. **142**(2): p. 331-340.
59. Kofman, V., et al., *Two-dimensional pulsed EPR spectroscopy of the copper protein azurin*. Journal of the American Chemical Society, 1996. **118**(5): p. 1201-1206.

References

60. Drew, S.C., et al., *Pleomorphic Copper Coordination by Alzheimer's Disease Amyloid-beta Peptide*. *Journal of the American Chemical Society*, 2009. **131**(3): p. 1195-1207.

· **Acknowledgements**

I would like to take this opportunity to express my deepest gratitude towards all the people who supported me, and enabled me to have such a nice and comfortable time within the Spiess-group at the MPI-P.

Foremost, I want to thank Dr. Dariush Hinderberger for the unlimited support, even under conditions, which could be best described as 'not physiologic', and for a diploma thesis, which could not have been more interesting after all (a typical win win win situation!).

I also wish to thank Prof. Harald Paulsen, who accompanied me on my mission within the MPI-P (being one of two biologists in total in our group), an important advisor and supporter, and, fortunately, also the first referee of this diploma thesis.

My deepest gratitude is also to Prof. Hans W. Spiess, who gave advice and support at any time and is the second referee for this thesis and.

One of the persons, who enabled me to perform all the practical work, at all, is Christian Bauer, who always had a solution to technical problems of any kind (and more) - thank you!

I am also most indebted to Matthias Junk and Jeannine Heller, two supporters and victims of a flood of questions, which were answered with highest patience and humor (...more humor).

Thank you very much!

Most important of all, I would like to thank my parents, my greatest supporters at all (who also saved me from starvation within the last days while writing this thesis).

It is hard to find the right words to thank so many people for their contribution to such a nice time, but I'm sure, that everyone, who reads this section, can be assured to be included in my acknowledgements.

Thank you so much!

Eidesstattliche Erklärung

Hiermit versichere ich an Eides statt, dass ich die vorliegende Arbeit selbstständig verfasst und keine anderen als die angegebenen Hilfsmittel verwendet habe.

Anderen Werken entnommene Textstellen, Daten und Abbildungen wurden unter Angabe der Quellen kenntlich gemacht.

Ferner versichere ich, dass ich diese Arbeit noch nicht in gleicher oder anderer Form an irgendeiner Stelle als Pruefungsleistung vorgelegt habe.

Ort, Datum

Unterschrift